THE UNIVERSITY *of* EDINBURGH

This thesis has been submitted in fulfilment of the requirements for a postgraduate degree (e.g. PhD, MPhil, DClinPsychol) at the University of Edinburgh. Please note the following terms and conditions of use:

- This work is protected by copyright and other intellectual property rights, which are retained by the thesis author, unless otherwise stated.
- A copy can be downloaded for personal non-commercial research or study, without prior permission or charge.
- This thesis cannot be reproduced or quoted extensively from without first obtaining permission in writing from the author.
- The content must not be changed in any way or sold commercially in any format or medium without the formal permission of the author.
- When referring to this work, full bibliographic details including the author, title, awarding institution and date of the thesis must be given.

Cryogenic Cold War: Closing the Thermal Conductivity Gap

Julia S. Kennedy

Institute for Astronomy

School of Physics and Astronomy

University of Edinburgh

Master of Philosophy

2013

Abstract

A critical analysis of published thermal conductivity data is presented which highlights failures in data extrapolation, unexplained sudden drops in previously observed material data sets and the clarity of equipment design.

Thermal conductivity measurements on a range of materials were performed using a Gifford-McMahon cryostat with the aim of consolidating current information on thermal properties as well as collecting data on new materials executed from 3 K to 30 K using the steady state method.

The ability of the cryostat to accurately cycle between desired temperatures was verified and used for thermal stability tests of materials for the Mid-Infrared Instrument to be launched on the James Webb Space Telescope. Tests undertaken on the electrical resistivity of aluminium foam were used to confirm the accuracy of the system. For steady state measurements of samples, the temperature across a known thickness of material was varied using a resistor heater of known power permitting the calculation of the thermal conductivity. The robustness of the system up to 20 K was shown using a Stainless Steel 316 sample, which agreed with expectations at the 2.1% level.

The thermal conductivity of boron-doped silicon was measured, specifically looking at the conductivity across a hydroxide-catalysis bond. Such bonded silicon and silicate bonds are integral to the ongoing research for the next generation of gravitational wave detectors. The thermal conductivity of p-type boron-doped silicon was shown to increase from 24.06 – 46.44W/mK over the 4 – 19 K temperature range.

The improvement in the design features of cryogenic systems outlined are being implemented in labs at the University of Glasgow. The experimental setup developed during the course of this PhD project will also be used for data collection for medical diagnostic equipment.

Declaration

I declare that this thesis is not substantially the same as any that I have submitted for a degree or diploma or other qualification at any other University. I further state that no part of my thesis has already been or is being concurrently submitted for any such degree, diploma or other qualification.

This thesis is the outcome of my own work except where specifically indicated in the text.

Julia S. Kennedy
Edinburgh
22nd May 2013

Acknowledgements

I would like to acknowledge all the staff at the University of Edinburgh and the Astronomy Technology Centre for the support they have given me during the course of my studies. I would also like to thank the Science and Technology Facilities Council, STFC, for the funding provided to conduct these studies.

Julia S Kennedy
Edinburgh
22nd May 2013

Table of Contents

List of Tables

List of Figures

Abbreviations

AO - Adaptive Optics
ALICE - A Large Ion Collider Experiment
ALMA - Atacama Large Millimeter/submillimeter Array
CCD - Charge Coupled Device
CERN - Conseil Européen pour la Recherche Nucléaire
CFRP - Carbon Fibre Reinforced Polymer
CMB - Cosmic Microwave Background
CMS - Common Muon Solenoid
CRIRES - Cryogenic Infrared Echelle Spectrograph
CSA - Canadian Space Agency
DIMM - Differential Image Motion Monitor
DR - Dilution Refrigerator
E-ELT - European Extremely Large Telescope
EM - Electromagnetic Spectrum
ESA - European Space Agency
FGS - Fine Guide Sensor
GE - General Electrical
GHP - Guarded Hot Plate
GM - Gifford-McMahon

GUI - Graphical User Interface

HARP - Heterodyne Array Receiver Programme

HEMT - High Electron Mobility Transistor

HST - Hubble Space Telescope

IR - Infrared

ISIM - Integrated Science Instruments Module

JCMT - James Clerk Maxwell Telescope

JT - Joule Thomson

JWST - James Webb Space Telescope

K - Kelvin

LHC - Large Hadron Collider

LHCb - Large Hardon Collider Beauty

LHCf - Large Hardon Collider forward

MIRI - Mid-infrared Instrument

mK - Millikelvin

MLI - Multilayer Insulation

NASA - National Aeronautics and Space Administration

NIRCam - Near-IR Camera

NIRSpec - Near-IR Spectrometer

PEEK - Polyetheretherketone

PID - Partial, Integral and Differential

PP - Polypropylene copolymer

PTC - Pulse tube cooler

PTR - Pulse Tube Refrigerator

RRR - Residual Resistivity Ratio

SCUBA - Sub-millimeter Common-User Bolometer Array

SHW - Short Hot Wire

SNR - Signal to noise ratio

SS316 - Stainless steel 316

S-Z - Sunyaev-Zel'dovich effect

THW - Transient Hot Wire

TFI - Tunable Filter Imager

TOTEM - TOTal Elastic and diffractive cross section Measurement

TPS - Transient Plane Source

UKATC - United Kingdom Astronomy Technology Centre

VLT - Very Large Telescope

WFL - Wiedemann-Franz-Lorenz Law

WMAP - Wilkinson Microwave Anisotropy Probe

Chapter 1

Introduction

Thermal and electrical properties of materials at cryogenic temperatures are important in the design and construction of instruments for astronomy. This thesis offers a thorough analysis of the thermal properties of construction materials used in instruments at very low temperatures. By studying thermal and electrical properties between 3 and 30 K we can provide recommended values to ensure the chosen materials meet the required specification. These proposed values can then be adopted by those who are selecting materials, with confidence that the materials will perform as desired.

Furthermore, the combination of theoretical values with experimental data is essential to develop a database of robust values, which is absent at this time. As part of this process and because experimental ability has flourished over the past few decades it has been revealed that some older data currently utilised may be incorrect.

An in depth critical analysis of data published between 1955 and the present has been developed and this investigation presents recommended values of data where possible. Some of these values are complemented by experimental values

calculated with modern equipment specially adapted for this purpose. A secondary objective of this thesis is to introduce an analysis of different methods for measuring the thermal conductivity of materials, with the method used herein being studied in depth.

This first chapter includes an introduction of instruments used at cryogenic temperatures (< 123 K) and their uses in astronomy. This contains details of the required information on the properties of materials before construction of an instrument is undertaken. Prior to this work there have been problems with instruments operating properly at cryogenic temperatures due to a lack of knowledge, or insufficient material testing in advance of instrument completion (section 1.4).

This thesis presents an overview of these issues and an explanatory example of how material properties are determined. Additionally, details of cooling techniques are discussed.

1.1 The necessity for instruments to assist astronomical discovery

Developments in technology are a necessary line of enquiry because without these advances, the rate of discovery and understanding in astronomy would decrease dramatically, even within theoretical investigations. To make these discoveries observing platforms, instruments and observing techniques are developed, as well computers for data output and analysis. In the early years of the 20^{th} century optical devices such as photographic plates were developed with photoelectric detectors following shortly afterwards [1]. By the 1940s, radars used in World War II accidentally detected radio waves from the sun, leading to the increased interest in radio astronomy. As diode and cryogenics technology was developed, sensitive radio instruments were produced [2]. In 1969 charge coupled devices (CCDs)

were developed using the advantages of both these earlier techniques [3]. In the 1960's development of infrared, X-ray, submillimeter and gamma-ray instruments increased [4].

1.1.1 Ground or space based observatory?

Many factors are considered when choosing whether to base a new observatory on the ground or in space, of primary concern is considering what part of the electromagnetic (EM) spectrum one wishes to view. As only visible, radio and sub-millimeter rays fully penetrate the Earth's atmosphere, all observatories on the ground must focus on this work. Figure 1.1 illustrates the regions of the EM spectrum which travel through the Earth's atmosphere. A ground based observatory can be as large as required as there is no need to consider how it will fit inside a launch vehicle to travel into space. Access is far easier if any problems occur or upgrades are required and instruments can have a long lifetime due to the accessibility when upgrading. However, there can be other complications and considerations due to monetary, political and aesthetic issues when choosing an appropriate site [5].

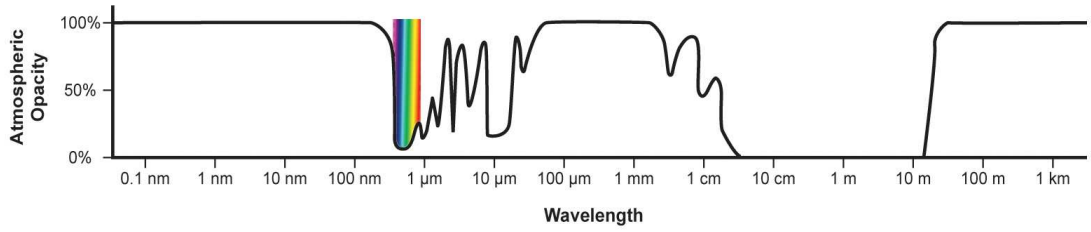

Figure 1.1: The Earth's atmosphere blocks most EM radiation from space: the atmospheric transmission of light can mainly be seen in the optical and radio bands [6].

In contrast, space based observatories have virtually no atmospheric loss, low background noise, close to 24-hour observing times and can image all wavelengths.

These observatories are more complex to design and build, are much harder to fix and upgrade once in orbit and are much more expensive to develop.

1.1.2 Signal detection

Every observation made can be broken down in to two distinct parts: the signal one is looking for and the background. The design of the telescope incorporates many factors to ensure as clean a signal as possible can be defined by reducing and eliminating noise. The signal-to-noise ratio (SNR) can be defined as:

$$\mathrm{SNR} \propto \mathrm{I}\,\Omega\,\mathrm{A}\,\epsilon\,\mathrm{D}^*\,\delta\,\lambda\,\sqrt{\mathrm{t}} \tag{1.1}$$

where IΩ is the flux density from the astronomical source, A is the area of the telescope, ϵ is the efficiency of the system as a whole (including any atmospheric impact), D^* is the sensitivity of the detector, $\delta\lambda$ is the observing bandwidth and the integration time, $\sqrt{t}$. The collecting area and the efficiency of the system as a whole are both directly related to the technology.

1.1.3 Where to detect?

Light pollution and atmospheric effects have an influence on positioning of telescopes. Telescopes were therefore gradually moved away from towns and cities and on to mountain tops to be further from areas of high light pollution. The increased altitude reduces the amount of atmosphere one must look through and the atmosphere is less disturbed than that seen at lower altitudes allowing more effective viewing due to better seeing (stable air with little turbulence). The air and atmosphere absorbs and scatters EM radiation, with redder light scattered less than bluer light. As water vapour absorbs much of the IR signal, placing these telescopes above as much of the atmosphere as possible reduces the loss in the infrared (IR) signal.

Gamma-rays and X-rays which are often targeted as a primary object of interest are absorbed by oxygen and nitrogen molecules, and UV-light is absorbed by oxygen and ozone molecules. This means that these rays are completely blocked by the atmosphere when attempts are made to view from the ground. The longest radio-waves do not penetrate electrons in the atmosphere so cannot be detected from the ground, but conversely shorter radio-waves do penetrate the atmosphere hence can be detected from the ground.

Adaptive optics (AO) have been developed to assist with reducing seeing effects due to optical effects introduced by the medium between the object and its image. Before focused light from the objective mirror reaches the detector, deformable mirrors are used and adjusted thousands of times each second to reconstruct images back to their original shape. A bright 'point source' (i.e. an object with a known shape such as a star) close to the desired object is used to analyse the atmospheric effects. If a bright object is not available, a laser guide star is created from which the system can be configured to compensate for atmospheric distortions. As conditions change over the period of an observation, AO compensations need to change in line with this. Actuators are used for this purpose; for example piezo-stacked actuators which expand or contract under voltage changes. Ideally, to ensure there is no over-compensation of signal, one must have at least the same number of measurements as number of actuators which control the mirror movement. The required AO correction is directly linked to the seeing conditions at the time of the observation: the worse the seeing conditions, the more AO correction that is required. [7]

The Very Large Telescope (VLT) in Chile examines the optical and IR regions and one of its instruments, the Cryogenic Infrared Echelle Spectrograph (CRIRES), uses AO. The instrument uses 60 actuators to optimise the signal to noise ratio (SNR) and spatial resolution. The AO system is housed on a tip-tilt stage and concentrates the light at the 0.2 arcsec wide spectrograph slit [8]. The

instrument has observed in all seeing conditions, from 0.5 - 1.5 arcsec. The Differential Image Motion Monitor (DIMM) is used to measure the quality of seeing using two images through parallel columns of atmosphere [3]. For the K-band, in 'good' seeing conditions (DIMM measurement below 0.78") the instrument produced an ensquared energy (concentration of energy in an optical image at a specified range) of 63% for magnitude R = 10 and 58% for R = 15, in In 'bad' seeing conditions (DIMM measurement above 0.78") they were 56% for R = 10 and 50% for R = 15 [9]. The measurements given are pessimistic for the instrument as the aberrations introduced by the IR camera were also taken into account, but the ensquared energy values are still within the requirements of the instrument.

1.1.4 Instrument efficiency

The overall efficiency of any given system constitutes many factors:

- Atmospheric transmission: Depending on the area of the electromagnetic (EM) spectrum an instrument is designed for observing, it may need to be sent to space as not all wavelengths will penetrate the atmosphere (see figure 1.1).

- Ground based instruments: An appropriate site must be chosen; for example, high sites with low water vapour for sub-millimeter studies or sea-level sites away from radio sources (cities, mobile phone networks etc.) for radio instruments.

- Background: The 'darkness' of the night sky is considered, especially when building optical and infrared (IR) instruments as a high photon background reduces the efficiency.

- Optical components: All optical components between the incoming ray of light and the detector must be optimised to reduce error in measurement.

This is a very challenging part of the design process as all optics must be configured to within $\lambda/20$ of the desired observation region. Once configured the optics must be aligned.

1.2 Instruments at cryogenic temperatures

The word cryogenics originates from the Greek words kryos meaning "frost" and genic meaning "to produce" and generally refers to temperatures below 123 K. To reach these temperatures, scientists require the use of liquid gases such as oxygen, nitrogen and helium. Further details of cryogenics and achieving cryogenic temperatures is given in section 1.6. The first refrigeration was in the 1840s, but from the point in 1908 when helium was liquified, a dramatic change in science and engineering occurred. The ability to use liquid helium for cooling allowed research to be carried out at near absolute zero, giving the opportunity to discover and understand more about the cold universe.

Many instruments used in astronomy use cryogenic technology in one form or another, for example; cryogenically cooled chambers for light collection; superconducting instruments; cooled mirrors; detectors and bolometers. These systems are differentiated by the region of the electromagnetic spectrum with which they are concerned. This section discusses the specific instruments and technology where cryogenic temperatures are required, primarily focusing on instruments for physics and astronomy throughout the EM spectrum, with some of the requirements for cold instruments illustrated in figure 1.2.

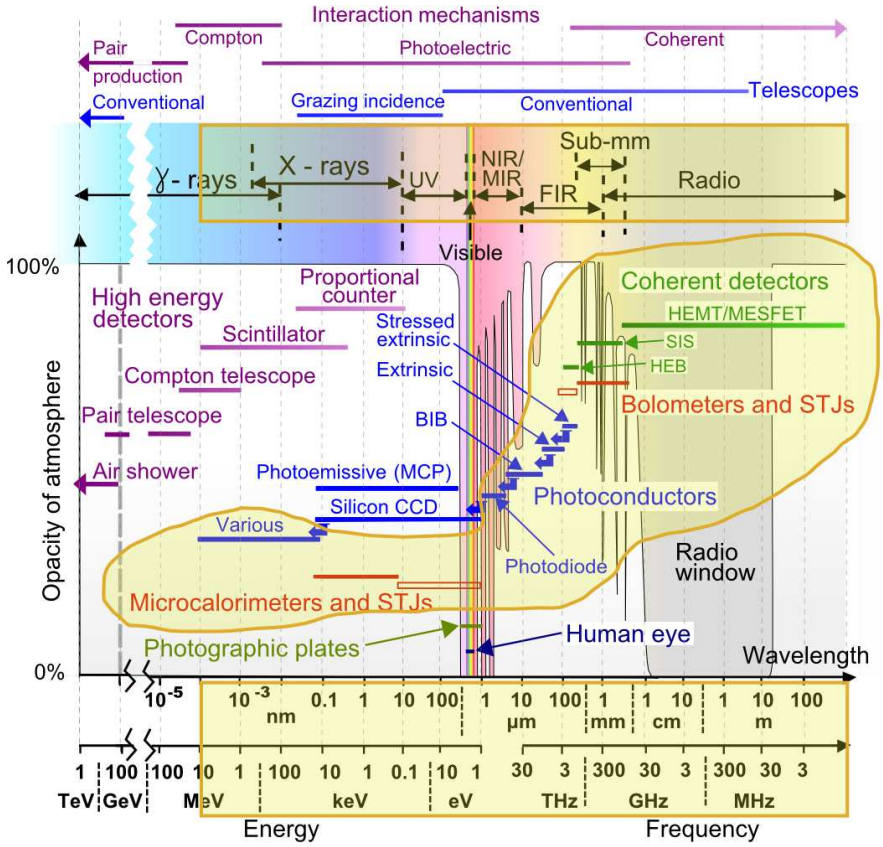

Figure 1.2: Some uses of Cryogenic technology through EM spectrum. Areas highlighted in yellow demonstrate some of the multiwavelength uses of cryogenics in astronomy [10].

1.2.1 Instruments through the EM spectrum

As we go through the EM spectrum from long wavelength radio-waves to short wavelength gamma-rays, cryogenic instrumentation is required in all areas. In detecting a signal in radio astronomy one of two methods is used: a low noise amplifier (for example a High Electron Mobility Transistor, HEMT), or a heterodyne mixer. In both of these instances, operation at cryogenic levels is preferable as it reduces noise interference. Additionally, some mixers used require superconductivity and therefore must operate at cryogenic temperatures [11].

For sub-mm wavelengths, the method used for detection varies depending on

the spectral resolution of measurements. Radio astronomy methods (HEMT and heterodyne mixers) are used for the high spectral resolution and bolometers are used for continuum and low spectral resolution measurements [11]. Many bolometers operate at 300 mK or lower, reducing the heat capacity and hence lowering time constants for the detector (to ensure it is practically useful) [12]. Optical filtering is required to ensure the bandwidth of incident radiation is reduced so the bolometer does not saturate [13]. Other methods can be employed including using superconducting tunnel junctions and kinetic inductance detectors which both rely on superconductivity thus operate cryogenically.

Cooling is required in infrared instruments to reduce dark noise (electrons promoted to the conduction band by thermal excitation). The bandgap varies in size with varying wavelengths - the longer the wavelength of photon to be detected, the lower the photon energy thus a smaller bandgap is required. The dark current (small current which flows in photosensitive devices when not in operation) depends on the bandgap size and the temperature, where smaller bandgaps require lower temperatures [14]. This technology requires temperatures of a few K at wavelengths of 200 μm, but can go up to operation as high as 100 K at a few μm.

The main devices used within optical astronomy are charge coupled device (CCD) cameras. CCDs have a much higher sensitivity and linearity than photographic film but require cooling to reduce dark noise (thermal excitation of electrons) [14]. The bandgap is larger than for IR detectors so less cooling is required thus they generally operate in the 150-200 K region. CCDs are also used to detect UV wavelengths, operating at similar temperatures.

Various different detectors are used in X-ray and gamma-ray astronomy including CCDs. Operating temperatures vary from room temperature (for scintillators) to below 100 mK (for microcalorimeters) [4]. Observations generally need to be carried out from space as the majority of rays are absorbed or reflected by

the atmosphere (figure 1.1).

1.2.2 The future of submillimeter detection: SCUBA-II

The Sub-millimeter Common-User Bolometer Array II, SCUBA-II, is a 10,000 pixel submillimeter camera on the James Clerk Maxwell Telescope (JCMT). SCUBA-II was built at the Royal Observatory Edinburgh, with the optics cooled for operation at 4 K. The camera was designed to replace SCUBA, the original bolometer camera for JCMT; SCUBA became operational in 1997. JCMT studies our Solar System (including our Sun), interstellar dust and gas and distant galaxies.

JCMT has a 15 m primary mirror, consisting of 276 aluminium skin panels bonded to an aluminium honeycomb structure. The alignment of the panels can be adjusted and the antenna altered to maintain the optimum overall mirror shape. The secondary mirror can be tilted in two axis for sky background calculations. JCMT is capable of rotation, including the observers carousel. JCMT offers the ability to hold multiple instruments simultaneously: the Cassegrain cabin and two Nasmyth platform hold heterodyne receivers, SCUBA-II and the Heterodyne Array Receiver Programme (HARP) respectively.

SCUBA-II replaced the original SCUBA, a 131 pixel camera and photometer consisting of two arrays of bolometeric detectors in hexagonal arrangements with additional photometry pixels at the edge of the long wave array. As SCUBA was such a success for research, with citations over a few years almost on a par with the Hubble Space Telescope, a second generation instrument was developed [15]. SCUBA-II offers continuum observing using eight detector arrays, four at each of 850 and 450 μm, and has a field of view of around 50 arcminutes. SCUBA-II successfully had first light in 2010 and since then has begun progression through the planned surveys.

Galactic astronomy SCUBA-II will examine the formation of stars and planetary systems in a wider field of view than has been studied previously. This will be focused on examining the origin and formation of dust. The SCUBA-II galactic plane survey will explore new areas of research: the star forming cloud population and the total mass of cloud dust in our Galaxy. With the capabilities of SCUBA-II this should only take around 50 hours to complete, as it is faster than previous instruments on JCMT. Further clouds above the Galactic plane will be searched for, revealing whether stars have been forming in this region. Finally, interstellar magnetic fields will be imaged in the wide-field, determining global magnetic fields between neighbouring galaxies [16].

Extragalactic astronomy SCUBA made an impact on extragalactic astronomy, especially our understanding of dust-obscured star formation. SCUBA-II aims to develop this further, using its wider field of view to fill in some of the gaps in our current knowledge. The history of star formation from the early stages is still unknown. Planned surveys will trace these early stages and with information from other regions of the EM spectrum this will reveal details of the early stages. Galaxy formation in the early universe and galaxy populations will be examined in a similar way, and the data collected, compared and contrasted alongside data from other regions of the EM spectrum to reveal the true beginnings. As submillimeter observations detect un-scattered photons, the survey will examine the Sunyaev-Zel'dovich (S-Z) effect [16].

With the increased pixel base and technological advancements of SCUBA-II as a submillimeter instrument, many cosmological questions can be investigated further and hopefully answered. SCUBA-II will also map dark areas to examine whether there are targets of interest, as preparatory work for future submillimeter surveys such as the Atacama Large Millimeter/submillimeter Array (ALMA).

Thermal design

SCUBA-II is the submillimeter equivalent of a CCD camera: it uses large arrays with 10,000 pixels in total to sample the sky, without having to 'sky chop' (take a background image from a section of sky outside the telescope's field of view). It has cryogenically cooled stages: 60 K, 4 K, 1 K and a few m K. Cooling of the lowest temperature detectors is by means of a cryogen-free dilution refrigerator (DR). The detectors operate at millikelvin temperatures. A 50 mK heat sink and the set of detectors are surrounded by the '1 K box', constructed from aluminium alloy 6082 T6. This '1 K' box is surrounded by radiation shielding, also held at 1 K. This completely surrounds the detectors to ensure that no radiation is allowed to enter from higher temperature areas of the instrument. The 1 K box is held in place with bolted joints meaning it can be removed from the instrument if required for alterations or upgrades. The detectors and 1 K box are connected with ribbon cable and further ribbon cable is used to run from copper plates on the 1 K box to the mK plate. To ensure sufficient thermal contact is made, joints are epoxy filled to increase contact area. The wiring for the mK box must be chosen very carefully as thermal isolation must be maintained between this and the 1 K box for successful operation.

In total, there are 256 SQUID series arrays (one for each column of detectors and 32 per sub-array), each of which dissipate around $1\mu W$ of power to the system. This excess heat must be removed from the system to maintain the required temperature [17]. The main cooling of SCUBA-II was to be provided using a dilution refrigerator (DR). The DR used consists of a two-stage pulse-tube cooler (PTC) for pre-cooling, before the helium enters a Joule-Thomson heat exchanger.

As both the TES and SQUID arrays are affected by magnetic fields, the

system was designed in such a way to eliminate these within the detector chamber. Superconducting shielding was fitted to the 1 K box to eliminate the majority of magnetic effects. Mu-metal (an alloy of iron and nickel) was added to the vacuum vessel and radiation shield to reduce the field strength within the superconducting shield. As the positioning of JCMT does not induce a large magnetic field, minimal shielding was required on the outside of the instrument.

SCUBA-II is a prime example of an instrument which required material testing to be carried out during manufacture. Furthermore, the implemented joints were constructed to perfect conditions, but if they need to be altered at any point this will potentially weaken them to an unknown specification. Ideally when joint specifications are tested, repeated construction and deconstruction should be carried out before retesting of the properties to ensure the structure can maintain the required specification after alterations have been made.

1.2.3 The future of astronomy: MIRI for JWST

The James Webb Space Telescope (JWST) is a 6.5 m aperture infrared telescope operating at 50 K and below, which is known as 'the Hubble Space Telescopes's (HST) successor'. The telescope is a joint program between National Aeronautics and Space Administration (NASA), the European Space Agency (ESA) and the Canadian Space Agency (CSA). JWST is currently planning for a 2018 launch on Ariane5 by ESA with the aim of orbiting at the Sun-Earth Lagrange point, 1.5×10^6 km from Earth. The telescope design incorporates four instruments on the integrated science instruments module (ISIM): a near-IR spectrometer (NIRSpec), a near-IR camera (NIRCam), tunable filter imager (TFI) and a mid-IR instrument (MIRI). These instruments share the telescope's field of view and can work simultaneously for parallel calibration and to assist thermal stability [18]. The Mid-Infrared Instrument is the only instrument on the JWST to operate in the mid-infrared range, specifically providing imagery, coronography and low

to medium spectroscopy over the $5 - 28.3\mu\ m$ band.

The science goals for JWST have been divided into four major science themes: first light and reionisation; assembly of galaxies; birth of first stars and planetary systems; and planetary systems and origin of life [18]. These science objectives cannot be met with any other existing or planned instrument either in space or on the ground.

The optical design of JWST incorporates a 6.5 m primary mirror, this design means the mirror is too large to fit in a conventional launcher. The telescope therefore features a segmented mirror comprising of 18 segments made from Beryllium, a lightweight material with good thermal stability at low temperatures [19]. The mirror segments will unfold after JWST has left our atmosphere and the full size mirror will be created. During a year, all regions of the sky can be observed. The instrument is designed to be operational for 70% of the time [18].

First light and reionisation JWST aims to identify the first luminous source(s) to assist with determining the ionisation history of the universe. Detection of low-redshift scattering of the Cosmic Microwave Background (CMB) by Wilkinson Microwave Anisotropy Probe (WMAP) [20] shows that the neutral universe became reionised at a redshift $z \simeq 10 - 15$. The hope is that JWST can both pin down this era more precisely and identify the source of the energy input that caused reionisation.

Broad band filters in JWST will create an ultra-deep survey, similar to that done by HST. Objects at increasing redshifts will be detected using the Lyman break technique, with JWST designed to have the sensitivity to reach AB=31 mag. This will be done using broad-band imaging in the near-IR with further data from mid-IR used to study very bright sources [19].

Assembly of galaxies Dark matter, stars and galaxies alongside the gas, metals, structures and active nuclei will be examined by JWST from the epoch of

reionisation to present. Groups of thousands of stars form galaxies, and these galaxies form the universe as we know it. Theory and observations have shown that galaxies are formed through merging of dark matter, first into small objects, then building up into larger hierarchical formation. The stars each individually move through their lifetimes (as depicted in the Hertzsprung-Russell diagram) at each step interacting with the surrounding gas, dust and dark matter. JWST will delve deeper into our understanding by investigating key questions about processes which determine galaxy properties and the role of starbursts and black holes.

Birth of stars and planetary systems JWST aims to determine more depth of understanding of the first stages of the birth of a star and the processes thereafter. Planetary systems will be examined in a similar way as although much is known, the early stages and detail of the later interactions is only now being uncovered. Many simulations have been created of the early stages of both stars and planets, but observations are lacking. With JWST, theory and observation can be combined to answer these questions on the early stages of formation and environmental impacts.

Planetary systems and the origin of life Physical and chemical properties of planetary systems will be researched by JWST to investigate the origin of life. The investigation will start with the formation of small objects, how they combine to make larger objects and how they enter orbits. We will then be able to determine more about how our solar system was formed. This will lead us towards a deeper understanding of how life could have been formed here and therefore in other solar systems. The filters for MIRI have been specially designed, and the four positions Exoplanet surveys have been performed by Kepler (2009 - present), specifically investigating the abundance of terrestrial and larger planets and the characteristics thereof. When the European Extremely Large Telescope (E-ELT)

is operational at the start of the next decade, exoplanet surveys in the optical and near-infrared region will be completed. JWST studies will complement the research done by Kepler and ELT, aiming to further our knowledge on other life forms. Finally, the cold objects and dust which can form in to debris disks around stars will be investigated further.

Thermal design and novel approach

This section focuses on MIRI and examines the thermal design, discussing the cryogenic requirements to achieve the goals set by the project.

The JWST will be launched warm and then passively cooled to around 50 K. The MIRI will be pre-cooled using a hybrid pulse-tube/JT cooler, separated from the optics module to reduce vibrations to the instrument [21]. Three instruments (NIRCam, NIRSpec and FGS) will operate at 35 K, with thermal switches in place to prevent overheating of the module during sunshield deployment and to prevent contamination heating from the rest of the structure [22]. The MIRI instrument is thermally isolated from the ISIM as the detectors must be actively cooled to near 7 K to ensure the stated sensitivity requirements are fulfilled. The modular design of the MIRI is an all-aluminium design to allow for isothermal stability, with a single stage thermal design [23] [24].

Thermal isolation of MIRI is important to ensure that the operating temperature of 7.1 K is not affected by the 35 K integrated science instruments module (ISIM). The struts holding MIRI in place are made of a high strength, high stiffness material but with low heat flow at cryogenic temperatures [25]. Carbon fibre reinforced polymer (CFRP) was chosen for these tubes as it has a low coefficient of thermal expansion, low density, high strength fibres and high strength:thermal conductivity ratio at cryogenic temperatures. A design meeting the performance requirements for launch and orbit, as well as the thermal prerequisites was required, with the symmetrical design allowing for stress to be equally distributed

in all directions [26].

A temperature of 15.5 K is required for reduction of the optical background noise from the mid-infrared thermal self-emission. The lower temperature, 7 K, which MIRI operates at is to account for reducing this thermal background to an optimum level for the one stage thermal design. The thermal architecture, illustrated in figure 1.3, consists of the 35 K ISIM structure; the 7 K Optics module of MIRI containing the three detectors; and the hydrogen dewar. The MIRI detectors are thermally isolated from the ISIM and are connected to the single stage dewar with a thermal strap, dedicated to take the heat load of the detector only. A second thermal strap is in place to take the remaining instrument thermal load as the precision of temperature control is less critical here.

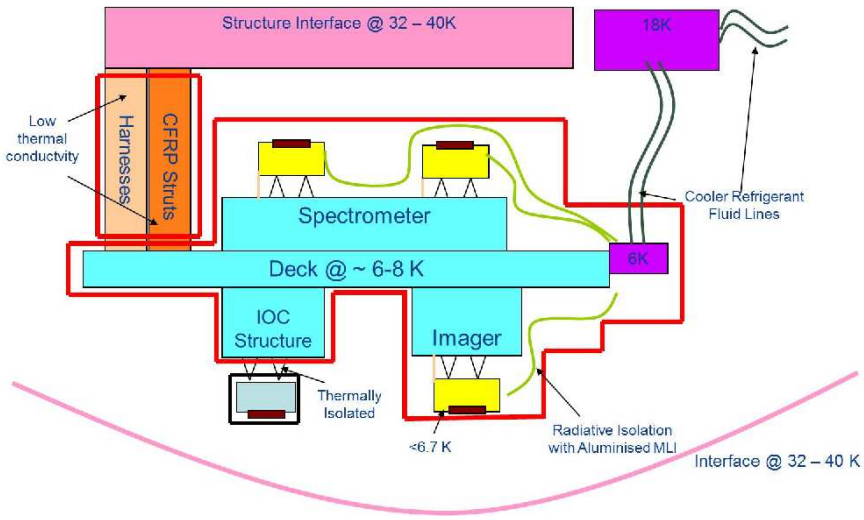

Figure 1.3: MIRI thermal design. (Image courtesy of Prof. G. Wright)

Thermal loss and contamination need to be considered: there will be radiative loss from the ISIM and structure as well as conduction through wiring and data harnesses.

As the JWST is an instrument designed to need no maintenance once operating, the optical and thermal/mechanical designs had to be designed to ensure the system was noise and vibration limited. A prototype was built to the ex-

act requirements of the final design, to be vibration tested in a simulator for liftoff. Mounting designs, optical alignment and components were tested prior and post launch. The optical design shown in figure 1.3 is enclosed in a 6061 (T6) aluminium alloy cover.

A full test model of MIRI was constructed and tested, successfully passing all stability and electronics tests after cooldown and launch simulations.

1.3 Cryogenic technologies in other areas of physics

Many instruments used in other areas of physics research also require cryogenic components such as superconducting elements. Two of the largest and most well known ground based projects currently utilising significant levels of cryogenic technology are the Large Hadron Collider (LHC) at CERN on the Swiss/French border and the Advanced LIGO Gravitational Wave detector in the USA.

1.3.1 Large Hadron Collider

One of the main applications of cryogenics in particle physics is for cooling the magnets in the Large Hadron Collider (LHC), the world's largest and most powerful particle accelerator located near Geneva, Switzerland. The LHC is a multi-billion pound project, involving 111 nations, and is now operating at full power after 70 years of developments in detectors for experimental particle physics [27].

The LHC is a 27km ring consisting of 9300 superconducting magnets, working alongside 4 detectors (A Large Ion Collider Experiment (ALICE), ATLAS, Common Muon Solenoid (CMS) and the Large Hadron Collider beauty (LHCb)), a further two experiments (TOTal Elastic and diffractive cross section Measurement (TOTEM) and the Large Hadron Collider forward (LHCf)) and a grid of processing and analysing computer power. Particles are fired round the LHC in

opposite directions close to the speed of light with very high energies. Once they reach optimum speed they are allowed to collide, creating new particles. It is at this point scientists track the created particles, examining their behaviour and identifying them. Accelerating structures have been built in to help boost the energy of the particles when required. These collisions will produce small patches of very high energy, which will help uncover the beginnings of our Universe.

Due to the nature of superconducting magnets, the network of magnets needs to be cooled to 1.8 K using liquid helium. The magnets are made from niobium-titanium wire wrapped in to coils. The helium supply must be constant, with heat sinks taking any excess heat out of the system. The collider is divided in to eight sections, with each having its own refrigerator. Liquid nitrogen is used to precool the system to 80 K, then helium is then injected in to the cold magnets to cool the system down to 4.5 K before finally cooling to 1.8 K.

The thermal contraction of the materials used to build the LHC ring have been calculated very carefully as this dramatic change in temperature makes the materials contract. This contraction is over 80 m in total for the full 27 km ring. Devices inserted between the magnets allow for this contraction to ensure smooth running.

Numerous problems arose during the construction and testing phases of the LHC with one of the most prominent problems occurring shortly after the LHC began operation. A transformer broke, then days later a helium leak occurred. These problems caused the system to be shut down for over 2 months, delaying the schedule and creating a huge financial loss.

The LHC is running at full power as of 2012, and on 4th July 2012 both ATLAS and CMS projects announced the observation of a particle consistent with the Higgs-boson [28].

1.3.2 Gravitational Wave detectors

Gravitational radiation is predicted by general relativity, in the form of "curvature of our space-time system that propagates outward at the speed of light, travelling outward from a moving object or system of objects" [29]. This curvature is produced by the mass-energy and momentum content of space-time. The more massive an object in space is, the greater the curvature it creates and the more intense the gravity. If objects orbit each other in a periodic way, the ripples in space-time will spread outwards similar to ripples on a pond: these are the gravitational waves.

These ripples in the curvature of space-time in turn cause a change in the separation between objects. Due to the nature of gravitational radiation these displacements are very small. Therefore, detectable (gravitational) signals are only produced by massive and compact astrophysical systems, such as neutron stars, supernovae and black holes. In fact, theoretical models currently predict the fractional relative displacement, or strain, from such astrophysical sources to be no greater than around 1 part in 10^{24} on Earth. This creates one of the greatest challenges for today's experimental scientists. In being able to detect these waves, scientists will be able to confirm the relativistic theory of gravity, impacting many areas of current research. A greater understanding of gravitational waves is important because these waves can propagate from and through regions that other (for example, electromagnetic) waves cannot. We may eventually be able to understand much more about black holes and the early phases of the Big Bang.

The most common method currently employed is laser interferometry, in which the interference pattern shown by the re-combination of light waves is used to detect the differential change in distances caused by the passage of a gravitational wave. Although it seems as if this may be easy to detect, the change occurring is minute, merely 10^{-18} m or less for arms length of 1 km [30]. One of the main factors in experimental design when trying to detect these gravitational

waves is to cut out all sources of noise from the surroundings so that the only remaining signals are from gravitational waves.

Thermal noise such as Brownian motion of the atoms with the mirror substrate material is a fundamental limitation in detecting gravitational waves. This can be reduced by fabricating the mirrors from low dissipation materials and by cooling the detector to low temperatures. One method envisaged for cooling the interferometers, used in the Cryogenic Laser Interferometry Observatory, CLIO, system [31], involves situating the mirrors in cryogenic chambers and reducing their temperature to approximately 20 K. The system is made of a pulse tube cooler (see section 1.6.2) with cold stages at 40 K and 4 K. The cooler is contained within a small vacuum tank and each cold head cools double radiation shields that are housed in the main mirror vacuum cryostat. Initial problems encountered with this system because of mirror contamination were overcome by introducing an 80 K pulse tube Gifford-McMahon refrigerator which assisted cooling of the radiation shield.

1.4 The effects of an incomplete material properties catalogue

Over the years there have been various technical problems due to cryogenic parts of instruments, with some attributed to a lack of knowledge on the construction materials.

Herschel Space Telescope

On Herschel's [32] first cooldown, the telescope did not focus. Tests were then carried out at cryogenic temperatures and the material characteristics were found to be different to predictions. This incomplete understanding caused a delay as adaptations were made.

James Webb Space Telescope

Much of the structure of JWST is made of Carbon fibre [33]. As this was a relatively new material, research was conducted to ensure the properties were sufficiently understood. Further research was conducted in to the materials for use in thermal straps and for joints. This was not damaging to the instrument as a whole, but incurred an extra time delay which could have been avoided if further material property data was available. [34]

ISOCAM

ISOCAM was well designed, but the incorrect wire was mistakenly used in the internal structure [35]. As the properties of the wire used were different to that which was planned to be used, heat leaked in to the instrument. This excess heat in the system meant it could not be cooled to the planned temperature, hence the planned scientific research would not have been able to be completed. Fortunately the mistake was noticed prior to launch, and the system was re-wired with the correct wire and the instrument cooled as expected. This highlights the necessity for correct materials being used which in turn relates to knowing enough about thermal and electrical properties of materials to implement them in complex systems.

Challenger Disaster

Possibly the most well known example of insufficient materials knowledge is the Challenger disaster in 1980, when failure of an o-ring caused the shuttle to explode 73 seconds after lift-off. The conclusion of the Report of the Presidential Commission on the Space Shuttle Challenger Accident was as follows:

"In view of the findings, the Commission concluded that the cause of the Challenger accident was the failure of the pressure seal in the aft field joint of the right Solid Rocket Motor. The failure was due to a faulty design unacceptably

sensitive to a number of factors. These factors were the effects of temperature, physical dimensions, the character of materials, the effects of re-usability, processing, and the reaction of the joint to dynamic loading" [36]. This statement alone shows that testing of all apparatus at the expected temperatures is of great importance.

1.5 Importance of knowledge on material properties

It can be seen from the examples discussed that the technology required both for current scientific research and future scientific goals is extremely complicated. As many of these goals are in the cryogenic region, it is of the highest importance that we have the knowledge and skills to design and build instruments as required. These requirements put a huge amount of pressure on researchers to choose the right materials for construction. This section has outlined some of the problems seen in the past with material data and how these can be resolved for future instrumentation.

To reach a conclusion on the suitability of a material one needs to look not simply at the numbers, but also to have a knowledge of the physical properties underlying thermal conductivity. The two sets of results collated in figures 1.4 and 1.5 demonstrate two of the key problems. Figure 1.4 illustrates a collection of measurements of the thermal conductivity of the polymer Torlon; one of Torlon 4301 [37] and four of Torlon 4303 [38] [39] [40]. The reference numbers 4301 and 4303 indicate different compositions of the same base material. The red line indicates Torlon 4301, so the inconsistency here can be attributed to this difference in composition from Torlon 4303. When looking at the rest of the data on the graph, huge inconsistencies can be seen in what is supposedly the same material. This is a demonstration that it is of utmost importance that one knows

the exact details of the composition of the material, including the details of the specific batch, before using it. The thermal conductivity of Torlon 4303 varies from 0.1 K through to 500 K, with a discontinuous and non-linear trend.

The polymer polyetheretherketone (PEEK) results, illustrated in figure 1.5, show four different compositions: Glass Filled, Carbon Fibre Filled, Ketron and finally pure PEEK [37] [38]. These results are some of the few readily available within published data in the last few decades and with apparent inconsistencies up to an order of magnitude can be shown. Looking in more detail at Runyan & Jones (2008) values for PEEK, it can be seen that the Glass Filled (GF30) and unfilled samples are significantly different over the temperature range shown: although the two samples are in agreement at 0.8 K, the thermal conductivity increases to 6.8 W/m.K at 3.9 K.

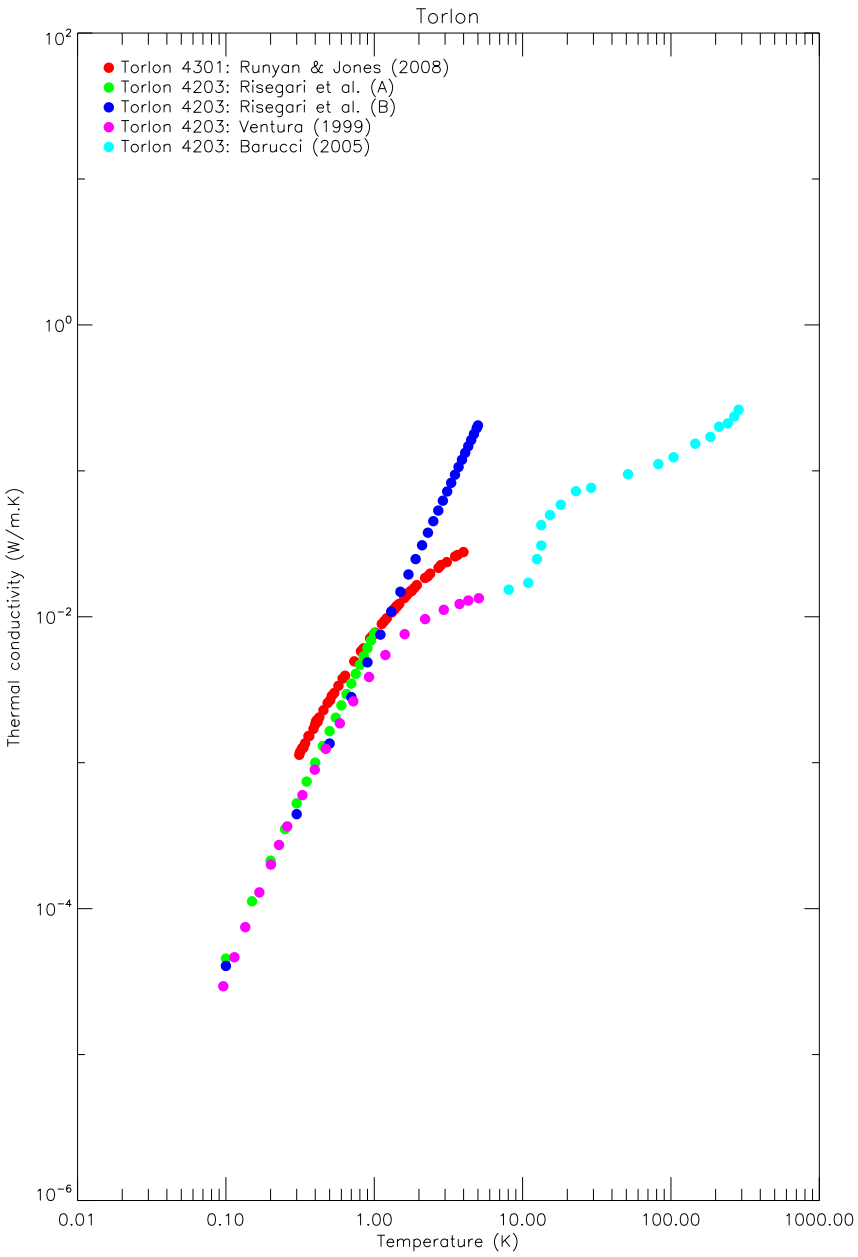

Figure 1.4: The thermal conductivity of Torlon as experimentally measured by other labs in previous years. For references see main text.

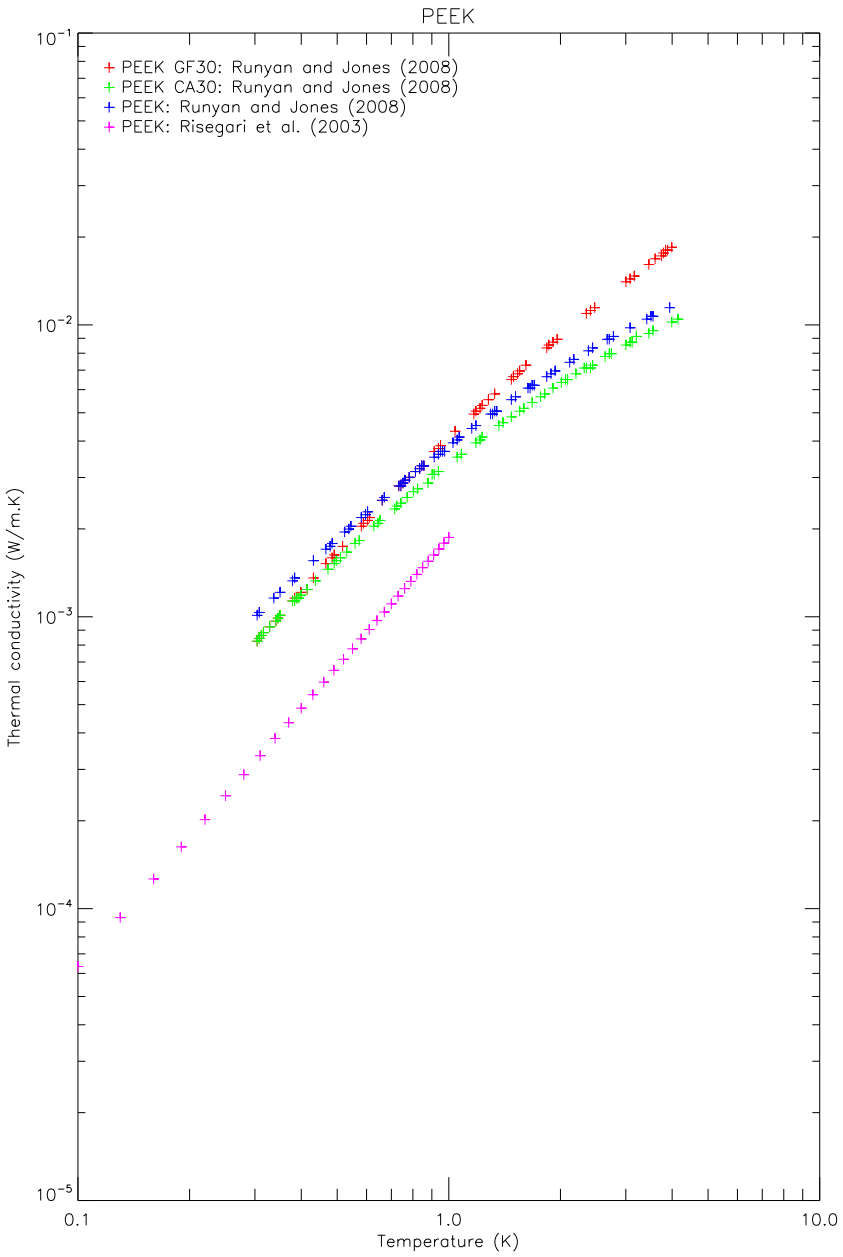

Figure 1.5: The thermal conductivity of Polyetheretherketone (PEEK) as experimentally measured by other labs in previous years. For references see main text.

When investigating whether to implement materials, the calculations for suitability will vary greatly depending on the source found. A more in depth critical

analysis of a variety of materials can be found in chapter 4.

1.5.1 How important is temperature?

As has been shown in the previous section, the choice of material to be used in different temperature ranges is of utmost importance as the properties can change so dramatically between materials, or with different compositions of the same material. During the construction of many instruments, each batch of a material to be used will be tested before implementation into an instrument. It is particularly important for space based instruments, such as JWST, as once the instrument has left land for its journey to space, it cannot be fixed.

1.5.2 Summary of how these properties vary with temperature

One of the other key factors surrounding material choice is how the properties vary with temperatures; the general behaviour of the key groups of materials is described below [41].

Metals

Depending on the quality of the material, the conductance varies dramatically. Good conductors (such as Cu, Ag, Al) conduct most of the heat in electrons. At high temperatures, large-angle scattering occurs by scattering electrons by vibrating ions predominates. At intermediate temperatures, the small-angle scattering is then of phonons. At low temperatures, electrons scattering off impurities will dominate.

Alloys

Electronic conductivity of disordered alloys is controlled at low temperatures by impurity scattering. Disorder of the electrons can reduce their electronic conductivity in these alloys which means the lattice thermal conductivity becomes more important. Electrons have a short mean free path, so $k \propto T$, smaller than that of pure metals.

Non-Metals

Lattice waves conduct heat, with velocity not changing much with temperature, but scattering processes change as the lattice spectrum becomes excited. High temperatures show dominant wavelengths of $\frac{\Theta}{T} \times$ lattice spacing (where $\Theta =$ lattice temperature). This scale is comparable to that of dislocations, stacking faults, point imperfections and point defects. At low temperatures, only long-wave phonons are excited and become scattered by large obstacles. At $T \leq \frac{\Theta}{5}$, anharmonic interactions between the lattice waves is dominant. Two processes within this occur: N- (normal) which redistributes energy or U- (Umklapp) which transfers momentum to the whole lattice, therefore limiting the conductivity. At times the absolute values of the scattering factors are difficult to define, for example at low temperatures due to the 'reflective' nature of the lattice.

Glasses and Amorphous Polymers

Localised low-energy excitations in glass scatter phonons, this increases the heat capacity at low temperatures. Heat capacity and heat conductivity of glasses and amorphous polymers varies slowly with temperature. When the temperature falls below 10 K, the heat capacity falls dramatically.

1.5.3 Difficulty of measurements

Another key issue is the difficulty in designing and constructing apparatus to conduct the measurements. For over a century research groups have been addressing this task, with varied outcome. Two key methods exist for determining the thermal conductivity of a material: steady-state and transient measurements. Within each of these there are numerous adaptations that have been made to the setup, but even the slightest change can have a large impact on the accuracy of results. Measurements are gradually becoming easier and more reproducible with advances in technology, including the software and computer power supporting experiments. Further details and an in depth analysis of some of these methods is given in chapter 3.

1.6 Achieving cryogenic temperatures

In the past, achieving cryogenic temperatures was not an easy task, but with the developments in technology this has become easier. Liquid refrigerants are commonly used when working at cryogenic temperatures, specifically nitrogen, oxygen and helium. At atmospheric pressure, nitrogen, ^{3}He and ^{4}He boil at temperatures of 77 K, 3.3 K and 4.2 K respectively. By controlling the pressure at the surface of the cryogen, temperatures as low as 1 K can be achieved.

Nitrogen is commonly used to pre-cool cryostats prior to the introduction of helium to the system, which results in less evaporation of helium. Thermal isolation must be maintained within a cryostat at all times, with most systems being kept in vacuum. Significant time delays can be caused if there are any problems or leaks, as these can only be fixed at room temperature. Occasionally an error will occur at low temperatures, but it appears to have corrected itself once warmed to room temperature. This creates more complex issues as it is harder to identify the problem.

The simplest method of cooling involves pumping liquid cryogen through a tube system from the storage dewar around the cryostat to the sample chamber, which gradually reduces the temperature of the sample chamber. As this process reduces the amount of helium in the storage dewar, the surface pressure will gradually change causing a slight change in overall temperature of helium. Systems have been developed to conserve the helium and surface pressure. [42]

Obtaining data at low temperatures

If measurements from cryogenic temperatures up to room temperature are required, the cryostat can be left to warm naturally for several days if the time constant for warming is long. If controlled temperatures above 4.2 K are required (but below liquid nitrogen temperatures) then a ^{4}He cryostat can be implemented. The base temperature of ^{4}He is 4.2 K and any temperatures above this can be achieved by integrating heaters to the system.

To obtain temperatures below 4.2 K using ^{4}He, the pressure above the surface must be lowered. The helium bath remains at 4.2 K and a small amount will be pumped to decrease the temperature around the experimental area. Adversely, this causes an increase in the rate of evaporation of ^{4}He making the process expensive.

The most common, and easiest, method of achieving temperatures below 1.3 K is to use ^{3}He as a cryogen. This allows one to easily reach 0.3 K and lower as the vapour pressure of the ^{3}He isotope is lower than that of ^{4}He, giving much greater cooling power. Using ^{3}He is an expensive method as the initial cost is greater and the heat of vapourisation is lower causing more ^{3}He to be lost in the process. In general, ^{3}He is only used in closed circuit cryostat systems to reduce loss as much as possible.

Nowadays, dilution refrigerators (DR) use a mixture of ^{4}He and ^{3}He. This mixture in a DR is capable of reaching temperatures of a few millikelvin and

closed-cycle cryostats can remain at that temperature for several months. There has been great progression in the field of cryogenics since this was achieved.

Maintaining low temperatures

When a cold system reaches constant temperatures, 4 factors must be controlled: conduction by the walls of the cryostat, radiation, convection of residual gas and thermoacoustic oscillations.

1. **Conduction by the walls of the cryostat**: Walls can be separated to reduce physical contact and hence reduce conduction.

2. **Radiation**: The emissivity of a material surface will effect the radiation in the system. The radiative heat flow can be controlled using radiation shields made of low emissivity materials, with the addition of further shields such as Multilayer Insulation (MLI).

3. **Convection of residual gas**: A vacuum can be created to reduce the number of air molecules available to transfer heat across layers.

4. **Thermoacoustic oscillations**: Thermally excited pressure oscillations can occur in tubes left with a closed end at high temperature and an open end at helium temperatures. This uses a great deal of helium and gradually increases the temperature of the system.

Types of cooling

There are multiple different cryostats on the market currently, which can be divided into 4 distinct groups:

1. **Closed-cycle**: Cryogenic vapour is pumped through a closed system by a mechanical refrigerator. As the vapour does not need to be replenished, this is ideal for projects requiring continuous cooling.

2. **Continuous flow**: Liquid helium is used and replenished when required. Large volumes of helium are used during operation.

3. **Multi-stage**: A coldplate is in place within a system with multiple stages, generally operating at different temperatures. These additional stages allow cooling to below helium temperatures.

4. **Bath**: These cryostats are a bath of helium into which the sample is lowered. Large volumes of helium boil off during operation.

The next section will detail some of these refrigerators and the cooling cycles in more detail.

1.6.1 Dilution refrigerators

The invention of dilution refrigerators (DR) in 1965 improved capabilities of cryogenics by using a mixture of ^{3}He and ^{4}He. This system allows temperatures of a few millikelvin to be achieved for periods of months on end. Using a DR rather than a single cryogen system requires less input power from support pumps and coolers to obtain the same cooling power in the instrument. The use of a DR is the only technique developed which is capable of achieving these millikelvin temperatures. In some systems a DR will be in place at the first stage, with other methods used at other points.

A ^{3}He:^{4}He mixture is used in most DRs today, offering efficient cooling power at low temperatures and keeping the cost of running the system low. The ^{3}He and ^{4}He will remain in the dilute phase through parts of the DR system, but as the pressure changes the two isotopes will form a mixture and cool to lower temperatures. The majority of modern systems use dilution refrigerators, using a mixture of ^{3}He and ^{4}He, with the potential of easily reaching temperatures of a few millikelvin (mK).

1.6.2 Mechanical refrigerators

Mechanical cryostats perform one of two operations: to liquefy a cryogenic gas, or to maintain low temperatures at a sample stage. Due to the complexity of these machines, large amounts of power are required to achieve consistent cooling.

Many modern cryocoolers use a gas compression-expansion cycle. During the expansion phase, the expansion of the liquid to a lower pressure achieves cooling. Various types of mechanical cryostats have been designed. A brief description is given here of some of the key types of mechanical refrigerators, focusing on the Gifford-McMahon system which was used for the experimental work contained in this thesis [13]

Joule-Thomson heat exchangers

A counterflow heat exchange is the main operation for the Joule-Thomson (JT) cooling system. Isenthalpic expansion of the cryogen produces liquid and a cold gas. Multiple expansion areas allow the gas to slowly expand creating lower temperatures, optimising the heat transfer.

Turbular heatflow must be maintained in the gas exchange pipes to give optimum performance of the heat exchangers. The heat transfer rate from the cryogen (gas) to the tube walls determines the effectiveness of the system. If the outgoing gas absorbs all the heat from the incoming gas then the system will be 100% efficient.

Linde type heat exchangers The Linde type heat exchanger is a multi-tube heat exchanger using a turbo-expander for cooling. In many examples of Linde cooling, the inner tube is smaller and carries the high-pressure stream of gas and the outer tube carries the low-pressure stream. Smaller versions of the Linde cooling system have been produced for medical technologies.

Klimenko coolers Klimenko coolers are very similar to the JT cycle, but use a gas *mixture* rather than a single gas. The compressed gas mixture travels through a counterflow gas exchanger, it then expands through a throttle and the cooled gas returns to the exchanger with a continuous process maintained. The mixture of gases is used to obtain the greatest efficiency possible by matching the heat capacities of the two counterflow streams. [13]

Philips Stirling cycle

The Stirling engine principle was used in 1954 to develop a small air liquifier, for incorporation into a cryocooler system, later to be known as the Philips-Stirling cycle. Regenerative heat exchangers have the benefit of being able to take the energy from one gas flow and exchange it to a secondary gas flow. The Stirling cryocooler, as shown in figure 1.6, contains two pistons and the cycle works as follows:

1. First the cryogen gas is compressed by the compression piston. The heat of compression is removed by water or air cooling.

2. The displacer transfers gas through the regenerator. The gas cools when in contact with the cold regenerator.

3. The two pistons move simultaneously, with further expansion and cooling.

4. The expansion piston moves away from the regenerator, allowing the gas to expand.

5. The cold gas transfers back to the original area as the two pistons are moved back to their original places and the cooling cycle repeats.

This procedure can also be carried out in a split-cycle cooler where the compressor and cold head are in separate areas. Compression is contained in one cylinder

and then the compressed gas is moved to the experimental area. This separation reduces vibrations at the cold head area where a sample or mechanisms would be stationed.

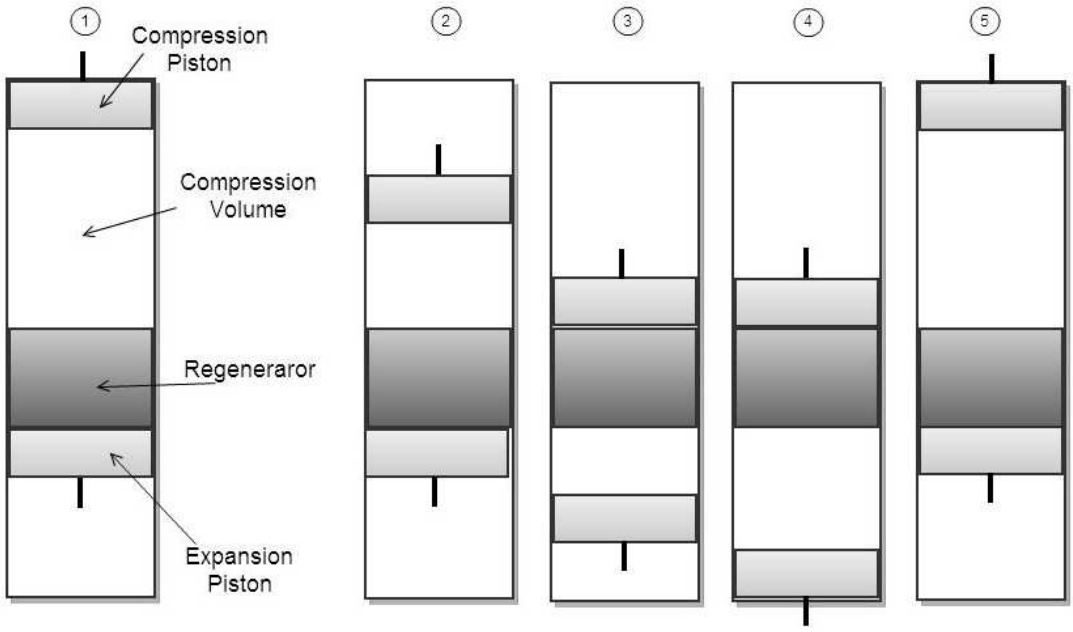

Figure 1.6: Mechanism for the Stirling cooling cycle.

Gifford-McMahon cooler

The Gifford-McMahon (GM) cooling system is similar to the Philips-Stirling cooler in that it has a displacement/refrigerator area, but here the compressor is controlled by inlet and outlet valves as follows:

1. The displacer begins at the cold end. The inlet valve is opened and compressed gas flows in to the warm end of the cylinder.

2. The inlet valve stays open as the displacer moves upwards towards the warm end of the cylinder. The gas passes through the regenerator to the cold end of the cylinder.

3. The inlet valve is closed, the exhaust (outlet) valve is slowly opened and cooling begins.

4. The displacer moves downwards again to the cold end of the cylinder, pushing out remaining cold gas. The exhaust valve shuts and the cycle repeats.

The GM cycle is available in single stage systems as well as multi-stage systems. The multistage systems have stages at various temperatures, for example, 60 K and 4 K and are commonly used for precooling large cryostat systems.

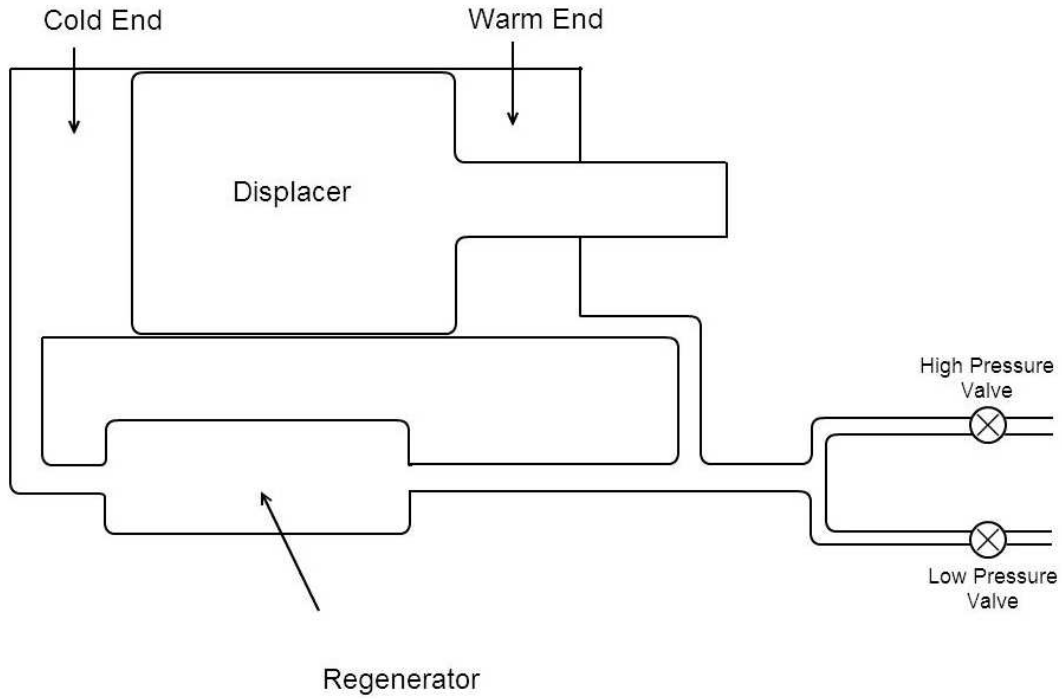

Figure 1.7: Mechanism for the Gifford McMahon cooling cycle.

Pulse tube refrigerators

Pulse tube refrigerators (PTR) have no moving parts at low temperatures, hence the lifetime of the system is lengthened and the vibrations dramatically reduced with respect to other cryogenic cooling systems. The mechanical operation can be based on the Stirling or GM mechanism, with an extra oriface and buffer at the

warm end of the system. In turn, the Stirling/GM mechanism creates pressure oscillations in the pulse tube, gradually cooling the required area by expansion of the cryogen gas [43].

1.7 Outline of thesis

We have now introduced the importance of knowledge of material properties at low temperatures before design and construction of instruments. We have seen the differing methods of achieving these low temperatures, and how these properties can vary with temperature. Previously published data have been introduced and the necessity to consolidate these data due to errors and unexplained differences between different research group's work has been explained. With this background, the thesis will consist of the following chapters:

- In **Chapter 2** the theory of properties of materials is outlined in some detail, specifically considering properties at low temperatures. This chapter introduces key equations which will be used in the experiments detailed later in the thesis.

- **Chapter 3** looks at the theory of low temperature thermal conductivity measurements as carried out in other laboratories. An analysis of both steady-state and frequency-time domain measurements is provided. This chapter also provides a conclusive overview of the method which will be used in the experimental work contained within this thesis.

- **Chapter 4** explains the method used to critically analyse previously published data from throughout the last century with a focus on materials used for experimental work of this thesis. Further detail is also given on polymers, which are becoming more widely used in low temperature experiments.

- In **Chapters 5 and 6** the experimental hardware and software are detailed. The experimental method is looked at in more detail including the analysis method and detailed errors of the system.

- In **Chapter 7** experimental results for the thermal conductivity of silicate bonded boron doped silicon are presented. Electrical resistivity of Aluminium Foam is presented with results of electrical resistivity of various wires used in instruments low temperatures available in appendix C.

- Finally, **Chapter 8** contains a summary of the work contained in this thesis and makes suggestions towards future work to lead on from the results presented here.

Chapter 2

Theory of material transport properties

Precise knowledge of the physical properties of construction materials at low temperatures is of utmost importance when designing scientific instruments. It is necessary to gain a full understanding of thermal and electrical factors, as these can influence both the design and function. Transport properties such as thermal and electrical conductivity are highly important when designing instruments. These need to be known as a function of temperature for successful integration into systems to provide optimum results for the designated purpose. Long time scales and specialist equipment are required to gather this information which means that many current designs are based on measurements made in the past on varying systems or for specific purposes. As seen in section 1.5, these varying conditions for collecting data need to be extremely well understood and methods implemented correctly to ensure errors do not occur. This chapter will take a closer look at

the structure of materials and the transport processes that occur within.

2.1 Material Structure

At the microscopic level, each material is one of 14 Bravais lattice structures stemming from its crystal structure: a unique arrangement of atoms or molecules, repeating in three dimensions. Although the general structure is limited to one of these 14, the general properties can vary depending on if the material is a pure or alloyed metal. Solids have a structure defined as either crystalline, for those solids with a regular repeating unit, or amorphous (non-crystalline) for those solids with no order within.

2.1.1 Crystal defects

Although a material may appear to have a smooth finish, at an atomic level this is not the case. Inconsistencies or defects in the structure can be present. Defects occur when the thermal energy within an atom of a crystal is higher then the energy required to remove an atom from the lattice site. 'Point defects' are localised defects within a crystal, 'line' and 'planar' defects occur in the larger structure. The most common defects are:

- Frenkel Defect: An atom migrates a short distance from the 'vacancy' it creates and situates itself in a gap in the crystal structure.
- Schottky Defect: An atom migrates to the surface of the crystal leaving an isolated vacancy.
- Isolated Interstitial: An atom diffuses from the surface of a crystal to the main structure causing an internal isolated interstitial defect.

The number and likelihood of defects change between materials, and even within a batch of a material it can differ. A substance with a tightly packed structure is less likely to have defects, as the atoms would require higher energy to be displaced, whereas in more open structures this required level of energy is lower. Line and planar defects can also have an influence on the transport properties of the material:

- Stacking Faults: A misalignment of stacked layers can cause a 'break' which creates an 'internal boundary'
- Dislocations: Both edge and in-plane (planar) defects can occur when the crystal is under stress or strain
- Antiphase Boundaries: Atoms within a crystal structure are configured in the opposite order to the 'ideal' system.

2.1.2 Purity

Further to defects, the purity of a material can have an additional effect on its properties. As properties of materials vary so much from near absolute zero to room temperature, the level of doping can have different effects at different temperatures. At high temperatures the doping may have no additional effect on the overall thermal conductivity, whereas when reaching low temperatures scattering might induce a drastic change in conductivity compared to the pure material [44].

2.1.3 Annealing

If materials are treated their properties can alter, as the crystal structure can be changed. This can again have either a positive or negative effect depending on the proposed use of the material. Annealing of a metal is a

process in which a metal is heated to a specific temperature and is then cooled slowly. This process softens the material, but can also change the internal and surface structure of the material due to a reduction in lattice defects [45]. The annealling process can be used to 'smooth out' any inconsistencies in the material structure.

2.2 Thermal expansion

As a material's temperature is raised, the particles within are given more energy, occupying excited states and leading to an increase in the mean interatomic distance. This results in the material expanding with increasing temperature, with the exception of Kevlar which has the opposite effect. This expansion with increase in temperature needs to be considered carefully to ensure no further problems are encountered. If an optical instrument is aligned and calibrated at room temperature, the optics will not necessarily be aligned at low temperature unless sufficient research and calculations have been done to allow for any expansion or contraction of structural materials.

The thermal expansion (α) of a material can be characterised by calculating the relative length (L) increase in a material with respect to temperature (T):

$$\alpha = \frac{1}{L}\frac{dL}{dT}. \tag{2.1}$$

A dramatic illustration of this problem was encountered during the research carried out for this thesis. When a silicon sample was placed in clamps during an experiment, it broke when heat was applied to the cryostat cold head when returning the system to room temperature. It is thought that

the copper clamps expanded with the sudden increase in temperature and crushed the sample, as shown in figure 2.1. Silicon has a near-zero thermal expansion at 4 K (0.022%), whereas copper has a thermal expansion of 0.324% at the same temperature [46]. Sufficient space had not been allowed between the sample and the copper clamps.

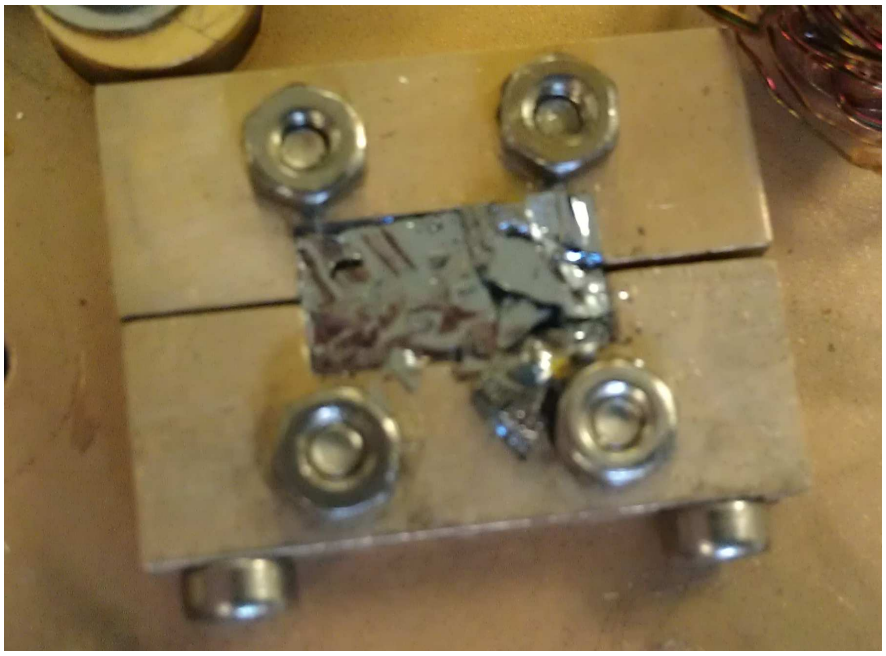

Figure 2.1: Illustration of broken samples. This occurred as the cryostat warmed up to room temperature. It is thought that the increase in temperature of the cryostat cold head led to the copper expanding at a faster rate than silicon, and thus crushed the silicon.

Many materials with a low thermal expansion coefficient have been researched, identified or developed. The resulting data are mainly available for room temperature, but low temperature data are available in publications such as 'Low Thermal Expansion Glass Ceramics' [47] and 'Heat Capacity and Thermal Expansion at Low Temperatures' [48]

2.3 Electrical resistivity

Electric charge within a material is carried by the negatively charged electrons. This charge conduction depends strongly on temperature, and varies greatly between pure materials at low temperatures. Knowledge of the electrical conduction can be used to estimate the thermal conduction at low temperatures hence gaining an understanding of the electron contribution to thermal properties.

Electrical resistivity, ρ is defined using 'free electrons':

$$\rho = \frac{m\overline{v}}{Ne^2\ell} \tag{2.2}$$

with electron mass, m, electron velocity, $\overline{v}$, number of electrons, N, the charge of an electron, e and the mean free path, ℓ.

The electrical resistivity (ρ) is temperature dependant and related to the electrical conductivity (σ_e) by:

$$\sigma_e = \frac{1}{\rho}. \tag{2.3}$$

High temperature

At high temperatures, thermal vibrations (phonons) of the crystal lattice dominate electron scattering which defines ℓ so this process is heavily temperature dependant.

Low temperature

At low temperatures, phonons do not have enough energy to cause electron scattering, so ℓ is dominated by electron scattering from defects and impurities (section 2.1.1) which is known as Residual Resistivity, ρ_{res}. At these

temperatures ℓ is temperature independent. It can be concluded that the higher purity a material is, the lower the residual resistivity it will have and hence the resistivity will become constant at a lower temperature.

One large difference in the residual resistivity, ρ_{res}, and the temperature dependant intrinsic resistivity, $\rho_i(T)$, is that the former is strongly affected by line and planar crystal defects which can form during preparation of the material. At higher temperatures where $\rho_i(T)$ is more dominant, the defects concerned are point defects which are independent to the material.

The scattering phonons and defect contributions need to be combined to output a value of resistivity we can use and trust. To get the total resistivity we can simply add the residual resistivity from defect scattering, $\rho_{res}, and the thermal vibrations, \rho_i(T)$:

$$\rho_{total}(T) \cong \rho_{res} + \rho_i(T). \tag{2.4}$$

2.3.1 Residual Resistance Ratio

The 'Residual Resistance Ratio' (RRR) is a way to easily express a resistivity without looking at sample dimensions. It can be used to gain an initial estimate of how a material will behave:

$$\mathrm{RRR} = \frac{\mathrm{R_{RT}}}{\mathrm{R_{4K}}} = \frac{\rho_{\mathrm{RT}}}{\rho_{\mathrm{4K}}}. \tag{2.5}$$

Using the room temperature resistance and resistivity, R_{RT} and ρ_{RT} respectively, and the resistance and resistivity at $4K$, R_{4K} and ρ_{4K} respectively the RRR of a material can be calculated. At low temperatures ρ_{res} dominates, so it can be assumed that $\rho_{\mathrm{res}} \cong \rho_{4\ K}$, and so, from equation 2.5:

$$\rho_{\text{res}} = \frac{\rho_{i\text{RT}}}{\text{RRR} - 1}, \quad \text{as} \quad \text{RRR} = \frac{\rho_{\text{iRT}} + \rho_{\text{res}}}{\rho_{\text{res}}}. \tag{2.6}$$

Furthermore, Umklapp scattering, or the U-process as it is sometimes known, occurs when an electron can be scattered both by a phonon and the complete crystal lattice. This can have a large effect on the direction and velocity of an electron hence greater electron resistance is created. This process depends solely on the particular material properties such as structure and phonon presence and can reduce the thermal conductivity of a material.

2.4 Thermal conductivity

The thermal conductivity of a material is the rate of flow of heat through a material per unit area, created by a temperature difference between two points. The total conductivity of a material is given by the summation of the different modes of conduction. Most materials will be dominated by one mode; pure metals (and dilute alloys) demonstrate conduction by free electrons. As a material becomes more alloyed there are fewer free electrons so conduction occurs by lattice vibrations (phonons). Semi-conductors demonstrate electron-hole pair conduction as well as free electron and phonon conduction. For both electron and lattice conduction, resistive elements play a part: imperfections, crystal boundaries and electron mean free path.

Thermal conductivity, λ, is the rate of heat flow per unit area with respect to a temperature gradient along length (L) within a material of cross section A, with respect to the power, P at temperature, ΔT :

$$\lambda = \frac{PL}{\Delta T A}. \tag{2.7}$$

Considering specific heat, thermal conductivity (λ) can also be defined as:

$$\lambda = \frac{1}{3}\frac{\mathrm{C}}{V_m}\nu\ell, \tag{2.8}$$

where C is the specific heat, V_m is molar volume, ν is the velocity of the carriers and ℓ the mean free path of the particles. For phonons, ν is the speed of sound, whereas for electrons it is $10^7 - 10^8 \mathrm{cm\,s^{-1}}$, both of which are independent of temperature at low temperatures.

2.4.1 Thermal conductance

Thermal conductance (G) is the quantity of power (P) passing through a substance of a constant cross sectional area when the two faces differ in temperature by ΔT:

$$G = \frac{\Delta T}{P}. \tag{2.9}$$

This value can be used to gain an understanding of a material, or to compare two materials of the same cross sectional area.

2.4.2 Electronic thermal conductivity

In metals, electronic thermal conductivity dominates because the thermal energy of the conduction electrons is much greater than that of the lattice phonons. The conduction electrons all have Fermi energy.

Semiconductors

The resistance properties of semiconductors are attributed to the presence of a band gap between valence and conduction bands. At very low temperatures, the valence band will be full and the conduction band empty therefore the material

will behave as an insulator. As one increases the temperature of the material, adding thermal energy, some electrons are given enough energy to 'jump' to the conduction band. The overall conduction of the material will now be attributed to the electron holes in the valence band and electrons in the conduction band. This temperature-dependant resistance is commonly used in technology for engineering temperature controlled systems in which the conductivity can also be controlled. Adding impurities to the semiconductor introduces more energy levels for the electrons to fill.

2.4.3 Thermal resistance

The total resistance of a substance can be described by incorporating the resistive effects for all phonon and electron interactions; phonon-phonon (pp), phonon-defect (pd), electron-phonon (ep), electron-impurity (ei), point/boundary defects (pb). When thermal resistances occur in series, the total resistance, R_{total} can be taken as the addition of the components:

$$R_{\text{total}} = R_{pp} + R_{pd} + R_{ep} + R_{ei} + R_{pb}. \tag{2.10}$$

These interactions are not necessarily all present in every material so the next section focuses on the main contributors:

$$R = R_{pp} + R_{ep}. \tag{2.11}$$

2.4.4 Lattice conductivity: phonons

Heat transfer differs with material. The purity of the material can have an effect on this transfer hence it is important to know the details of the materials' composition. Phonons are the main carrier in amorphous insulating solids and dielectric

crystals. Furthermore, lattice conduction is responsible for the majority of heat transfer in impure metals, alloys and semiconductors. The Debye temperature (θ_D) needs to be taken into consideration when discussing thermal conductivity of phonons (see section 2.5.1).

Low temperatures: $T \ll \theta_D$

The number of thermally excited phonons is relatively small. The phonons no longer cause a significant amount of scattering within themselves, but they can be scattered by crystal defects and boundaries. Since at low temperatures the dominant phonon wavelength is larger than the lattice point imperfections, the crystal boundaries are the only relevant factor. This means that the phonon thermal conductivity, λ_{ph}, tends to be temperature independent. This leads to the conclusion that the temperature dependence of thermal conductivity at low temperatures is that of the phonon specific heat, C (see section 2.5):

$$\lambda_{ph} \propto C_{ph} \propto T^3. \tag{2.12}$$

High temperatures: $T > 50\ K$

In this temperature range scattering is dominated by phonon-phonon interactions. With increasing temperature the number of phonons increases, and hence λ_{ph} decreases. Overall in this temperature range the thermal conductivity is inversely related to temperature..

Due to differences in defects, low temperature thermal conductivity of comparable samples can vary greatly. As stated previously, phonons are the main carriers in dielectric crystals. If very few defects and impurities exist, the thermal conductivity can be extremely high and similar to metals such as copper and aluminium. Conversely, the thermal conductivity of a strongly disordered

insulator can be very small owing to large numbers of phonon scattering from defects.

Another example is glass in which additional scattering exists because of tunnelling states [49]. This puts a limit on phonon thermal conductivity. This also means that due to temperature dependence, the thermal conductivity is almost always proportional to T^2 below 1 K and forms a plateau around 2-20 K.

2.5 Specific heat

Specific heat describes the temperature change of a system due to the required heat per unit mass to raise or lower the temperature. More precisely it is the amount of energy one mole of a substance requires to increase its temperature by one degree, or conversely the amount of energy required to be extracted for it to decrease by one degree. Heat capacity is similar, but is relative to the heating and cooling of the material *as a whole* hence is an extensive variable. As the specific heat of a material has such a strong dependence on temperature, it needs to be known precisely. This is eminently important in astronomical instruments as a small miscalculation in heat transfer can have disastrous effects. When considering the specific heat of a material, the atomic excitations within must be examined. These will differ between different types of material: insulators, metals, crystalline and non-crystalline substances.

At high temperatures all vibrational states of an atom are excited. From this, one can take each atom as an independent classical oscillator, relating to the Dulong-Petit value. The Dulong-Petit value of the high temperature specific heat of a material with N_0 atoms per mole, of which each has 3 degrees of freedom (for potential and kinetic energy). Each degree of freedom contributes $k_B/2$ to the specific heat at a constant volume (C_v):

$$C_v = \frac{6}{2} N_0 k_B = 3R = 24.94 \frac{\text{J}}{\text{mol K}}. \tag{2.13}$$

This holds until the thermal energy, $k_B T$, becomes high enough to be of the order of that necessary for excitation of lattice vibrations.

Definition

Heat capacity (C) is the ratio of the change in heat (dQ) added (or removed) to the change in temperature (dT), with the quantity x representing a constraint which can be imposed on the system:

$$C_x = \left[\frac{dQ}{dT} \right]_x . \tag{2.14}$$

Heat capacity can be written as a function of pressure, volume or mass. For solids, both linear dimensions and the shape can be altered by a change in temperature. This means that specific heat should be measured at constant pressure. The relationship for specific heat at constant pressure (C_p) and constant volume (C_v) can be shown by:

$$C_p - C_v = \frac{\beta^2 \nu T}{\kappa_T} \tag{2.15}$$

with specific volume, ν, coefficient of volume expansion, β, temperature, T and isothermal compressibility, κ_T. This equation applies generally to crystalline solids [50].

Equation 2.15 cannot in practice be applied to most materials due to the lack of low temperature data, but an approximation can be used:

$$C_p - C_v = A C_p^2 T. \tag{2.16}$$

where A is the cross sectional area of the material.

2.5.1 Debye specific heat

Debye specific heat assumes that the crystal lattice is continuous and only specific wavelengths can be maintained. These wavelengths are the only ones that set up standing waves. Peter Debye also established an upper limit to the frequencies that could exist. The propagation velocities in longitudinal and transverse directions are considered as well as the volume. From this one can derive the Debye characteristic temperature, θ_D:

$$\theta_{\mathrm{D}} = \frac{h\nu_{\max}}{k} \tag{2.17}$$

with Planck's constant, h, the maximum velocity $\nu_{\max}$. The Debye specific heat, C_v, can be written as:

$$C_v = 9rR\left[\frac{T}{\theta_D}\right]^3 \int x_m ax6e^x x^4 \frac{dx}{(e^x-1)^2}. \tag{2.18}$$

At high temperatures (low values of x), C_v approaches the 3R Dulong-Petit value and at low temperatures the upper integration value becomes large. For $T \leq \frac{\theta_D}{10}$ it approaches ∞ and the integral becomes $\frac{12\pi^4}{45}$ so:

$$C_v \simeq 1944r\left[\frac{T}{\theta_D}\right]^3 J\mathrm{mol}^{-1}K^{-1} = \beta T^3. \tag{2.19}$$

This equation can be used to calculate θ_D or β. One needs to remember that the Debye theory is only valid at low temperatures and the value 'r' is often removed (no. of atoms per molecule) as often monotomic solids are used ($r = 1$). If there is more than one molecule $\frac{C_v}{3R}$ represents specific heat for $\frac{1}{r}$ of a mole.

2.5.2 Lattice specific heat

The frequency of vibration of atoms and molecules within a solid dominates the internal energy (i.e. specific heat). The free electrons can also contribute for metals, but only at very low temperatures (approximately 3 K).

This discussion begins by looking at the equipartition of energy as shown by Boltzmann. A particle will have $\frac{1}{2}kT$ of energy for every degree of freedom (R) while in equilibrium. A crystal lattice (in the classical form) contains 6 degrees of freedom in the 3D view with energy depending both on velocity and mean free path (position). This means that each part contains $3kT$ of energy hence one mole has:

$$E = 3N_A kT = 3RT. \tag{2.20}$$

This leads on to give specific heat with respect to volume of:

$$C_v = \frac{dE}{dT} = 3R. \tag{2.21}$$

2.5.3 Electronic specific heat

Since the lattice term is proportional to T^3 (see equation 2.19), the electronic specific heat is relatively small *except* at low temperatures. The derivation of electronic specific heat begins by looking at the Fermi-Dirac distribution. This defines the probability of an energy state (E) being occupied by an electron (in an ideal electron gas in thermal equilibrium):

$$f(E) = \frac{1}{\exp\left[\frac{E-E_F}{k_T}\right] + 1}. \tag{2.22}$$

where E_F is the Fermi energy.

1. At absolute zero, all energy states are full so $f(E) = 1$ for energies less than E_F and empty for $f(E) = 0$ for $E > E_F$
2. As the temperature increases, the probability of finding a state occupied at energies above E_F increases.
3. Any electron which jumps to a higher state contributes to specific heat.

The number of electrons capable of jumping energy levels can be estimated. The thermal energy of an electron of Fermi Energy is $E_F = kT_F$. For most metals $E_F = 8.8 \times 10^{-19} J$, so it follows that $T_F \simeq 6 \times 10^4 K$. This shows that the fraction of electrons that lie within kT of the Fermi energy is $\sim \frac{T}{T_F}$ so at room temperature this equates to around 0.5% of the electrons having the capability to jump up an energy level and hence contribute to specific heat .

To now look at a mole of a monovalent metal: N conduction electrons exist hence $\frac{NT}{T_F}$ electrons contribute to specific heat. Each one of these electrons will have an energy kT hence the total energy, E_{el}, is:

$$E_{el} \simeq N \left[\frac{T}{T_F}\right] kT. \tag{2.23}$$

So at 300K the electronic specific heat, C_{el}, is:

$$C_{el} = 2\frac{NkT}{T_F}, \tag{2.24}$$

Introducing the energy of electrons in the Fermi-Dirac distribution function allows the previous equation to be differentiated this with respect to T to yield the electronic specific heat:

$$C_{el} = \frac{1}{3}\pi^2 D(E_F) k^2 T = \gamma T, \tag{2.25}$$

where $\gamma = \frac{1}{3}\pi^2 D(E_F)k^2$. This gives a linear temperature dependence of electronic specific heat until $T/T_F \simeq 0.2$. At very high temperatures it approaches $\frac{3}{2}R$, the classical value for the electronic contribution per mole.

2.5.4 Total specific heat

To calculate the total specific heat, both the lattice and electronic parts (sections 2.5.2 and 2.5.3 respectively) must be taken into consideration:

$$C_{total} = \beta T^3 + \gamma T. \tag{2.26}$$

As electronic specific heat only occurs in metals, $\gamma = 0$ for all non-metals. This means that a check can be done by plotting $\frac{C}{T}$ against T^2 which should produce a straight line. When the material in question is a metal, $\gamma \neq 0$ and from this graph the values of β and γ can be obtained.

When one approaches higher temperatures, the produced graph is no longer a straight line, so the T^3 law is no longer valid [50]. Materials with electronic and lattice contributions are dominated by the T^3 term except at very low temperatures. When $T \leq 4K$, the linear (T) electronic term and the cubic term are of the same order. Low temperature data are required to allow separation.

2.6 Predicting thermal conductivity

Tools have been developed to predict the thermal conductivity of a material using other available data. At times, electrical conductivity data will be available for a temperature range but not the thermal conductivity data. Information might also be available on impurities, defects, magnetic fields and more; applying this can assist with defining further information.

2.6.1 Weidemann-Franz-Lorenz Law

Thermal and electrical conductivity can be related using the Wiedemann-Franz-Lorenz (WFL) Law. This is beneficial as electrical conductivity tends to be easier to measure than thermal conductivity, especially at lower temperatures [51]. For metals, both conductivities are heavily based on the flow of electrons.

$$L_0 = \frac{\lambda(T)}{\sigma(T) \cdot T}. \tag{2.27}$$

Sommerfield derived the Lorentz number (L_0) to be:

$$L_0 = \frac{\pi^2 K_{\mathrm{B}}^2}{3e^2} = 2.45 \times 10^{-8} \mathrm{WK}^{-2}. \tag{2.28}$$

Experimentally, this law applies within a few percent at room temperature where electron scattering from high energy phonons dominates, and also at low temperatures where electron scattering from impurities dominates. At intermediate temperatures, energy loss from electron-phonon collisions limits flow of heat rather than flow of charge so the behaviour deviates from the law.

2.7 Summary

This chapter has looked at details of the thermal properties of materials and why they change with temperature. The following chapter will examine some thermal conductivity measurement systems used in the past half century, and the designs used presently.

Chapter 3

Experimental methods and measurement techniques

We have seen from the previous chapter how important the compilation of knowledge on material properties is prior to the design and construction of cryogenic instruments. Inconsistencies in published values exist due to differing equipment and experimental setups used to conduct measurements. Accurate measurements of the thermal conductivity of a material are difficult to achieve. One of the main problems is the characterisation of the heat flux through the test material as opposed to heat lost to the surroundings and equipment. Steady state and frequency domain methods are two common methods for measuring thermal conductivity. Many variants on these methods have been developed; but regardless of which is used, extreme care must be taken with the design and manufacture of the experimental setup to reduce errors. The smallest of errors in apparatus and experimental methods at this stage can lead to disastrous effects if implemented in a working instrument. This chapter will give an overview of the most com-

mon techniques used to determine the most appropriate way to conduct these experiments.

3.1 Steady-state methods

The first steady state thermal conductivity measurements were conducted at room temperature and investigated the transfer of heat along an arrangement of bars using water and steam jackets as heaters, as illustrated in figure 3.1 [52], [53]. In this apparatus the use of water and steam jackets as heaters limited the control of temperature. In subsequent years, the accuracy of these measurements was improved with the developments in assistive technology. This progression resulted in the development of apparatus that allowed these measurements to be conducted at cryogenic temperatures. Due to increased standardisation and improvements in instrumentation, experimental setups are now used at multiple laboratories This has resulted in a progressive improvement in the ability to obtain accurate results, especially at low temperatures (for example [54], [55], [56], [57] and [58]).

The absolute linear method tends to be the basis of any steady state measurements. No large variation in the apparatus or setup used by each individual research group was noted.

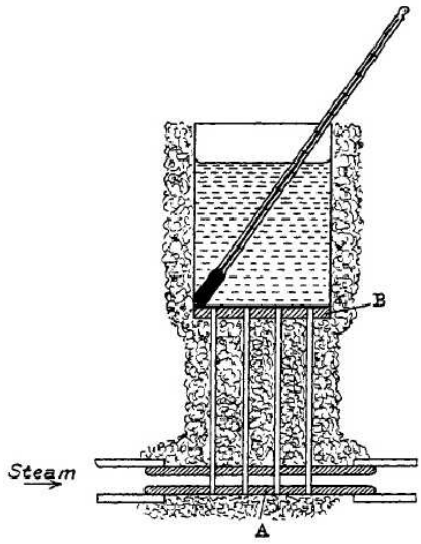

Figure 3.1: Early thermal conductivity as carried out with a steam jacket [53].

The steady state technique involves heating one end of a sample while holding the other end at a set cold temperature. A direct measurement of heat flux and the change in temperature along a specimen of known dimensions is then taken. The concept for this operation is illustrated in figure 3.2 where the basic setup consists of a bar sample fixed in place with one end attached to the cold head where the temperature can be stabilised. A heater is connected to the other end and is used to deliver heat to the system, creating a temperature gradient. The power to the heater must be held static for measurements of the temperature at different points to be monitored by thermocouples attached to the sample. This whole sample is contained within radiation shield(s) and the system is held within a high vacuum to minimise heat loss by convection. Temperature sensors are placed in various places on the sample and shields to monitor heat transfers and losses. Using the data from all temperature sensors, measurements can be computed and used to create a 1D heat flow model.

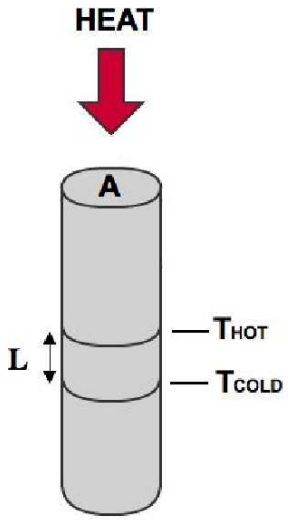

Figure 3.2: Experimental setup for steady-state measurements through sample of known cross sectional area, A, and length, L. Sensors are placed at T_{HOT} and T_{COLD} and power is applied using a heater at one end while the other end is held at a constant temperature.

For the standard setup with a bar sample with two temperature sensors, the thermal conductivity, λ, through length L and cross sectional area A, when power P is generated from an heater can be defined as:

$$\lambda = \frac{L \cdot P}{A \cdot (T_{\mathrm{HOT}} - T_{\mathrm{COLD}})}. \tag{3.1}$$

The base must be maintained at a constant temperature, and sensors measure the temperature at points T_{HOT} and $\mathrm{T_{COLD}}$ across which a temperature gradient has been created. The heat flow must be isothermal before reaching T_{HOT} and the cross sectional area must be constant over length ΔL. Different configurations have been employed by laboratories, and therefore the related analysis varies slightly. The general case, as depicted in figure 3.2, consists of a solid block with sensors fixed on the outside of the sample. With this arrangement the precise location of the sensors must be calculated to ensure the heat flux monitored is

representative of the section measured. This arrangement also allows multiple measurements to be made on a material from the same batch during one cool down cycle.

3.1.1 Divided samples method

The 'divided bar' method can be employed whereby a sensor is positioned between two sections of the same material of different lengths and the conductivity of each section is calculated separately [54]. A further variation on the divided bar setup is to have a set of samples of various thicknesses, divided by thin blocks of a high thermal conductivity materials each with their own temperature sensor [58]. Using a material such as copper or aluminium gives a negligible thermal conductivity compared to a relatively low thermal conductivity sample. The insertion of a reference specimen between the sample and cold head can allow the validity of each individual measurement to be checked instantaneously [55]. This arrangement holds many advantages over previous methods employed: it allows systematic errors to be checked during each measurement allowing inconsistencies to be identified immediately. In systems where this is not carried out, some data can be lost if an inconsistency is identified after collection. This results in the loss of time as protracted periods are required for experiments at low temperatures.

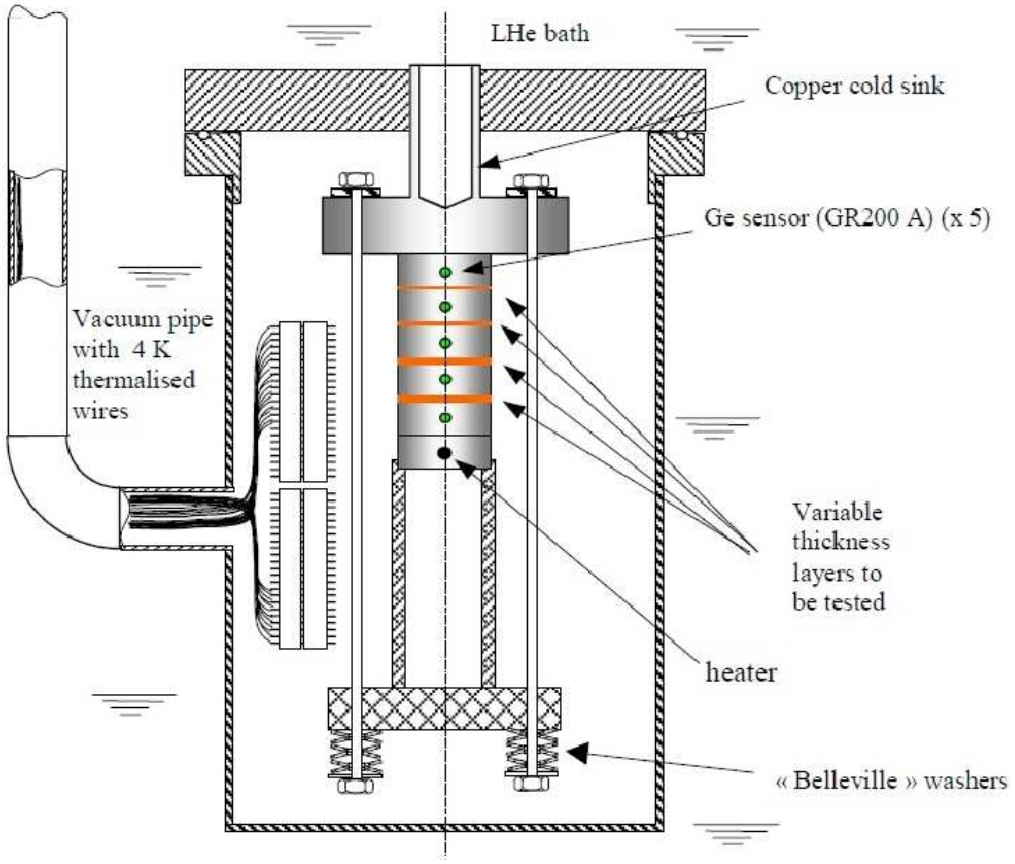

Figure 3.3: Divided bar setup as used for thermal conductivity measurements [58].

Figure 3.3 shows that this setup has been adapted for differing purposes and materials. Longitudinal heat flow measurements at low temperatures are extremely time consuming due to temperature stabilisation times, cooling time, heating times and creating a vacuum in the apparatus. Researchers at Clemson University created a setup whereby the sample area could be easily mounted on a removable puck, allowing rapid changeover of samples (as sensors were already fixed on the sample before mounting on the cold head) [57]. This specific setup is large enough for two samples to be measured simultaneously in the puck and cold head areas. This is an excellent way to reduce the changeover time between

sample measurements and is a technique that was employed in the measurements carried out during these studies.

More recently Ventura et. al have carried out a series of measurements below 5K. The experimental assembly is a simplified longitudinal heat flow design where the end of the sample screws into a copper cold head and the 'hot end' screws into a holder complete with temperature sensors and heaters. The cold end is kept at a constant temperature and the heaters on the 'hot end' introduce stepped heating. This system has been designed and calibrated over many years and series of measurements. It is a good example of a suitable system for these measurements. As the Firenze University group have successfully measured multiple materials using this configuration [56] [59] [60] [61] [62], a visit was made to the group to study their system further. Their cryogenic laboratory is fully automated, tailored for thermal conductivity and specific heat capacity measurements of small materials. These are all factors which assist rapid data collection and analysis.

3.1.2 Reducing heat loss and radiative effects

One of the biggest problems with steady state measurements is the control of heat introduced to the 'hot end' of the sample. Some of this heat will be lost to the surrounding chamber due to convection and radiation so the exact quantity that passes through the sample must be determined by calculation. Convective loss is reduced dramatically by implementing a high vacuum as the majority of air particles are removed from the system, reducing the chance of particle collisions.

Radiative losses pose a larger problem as they are caused by any EM radiation in the system, including that from surfaces within the cryostat. Materials with low emmissivity surfaces are generally chosen for construction of cryostats to reduce radiative effects.

Radiative effects can be reduced even further with careful selection of mate-

rials and coatings for the cold head, heat sink and radiation shields. The system needs to be optimised, especially for materials of high emissivity. Research conducted using black stencil ink on the heat sink to achieve an emissivity of $\varepsilon = 1$ was conducted: this has an adverse effect on boundary effects of radiation. This research shows results from $233\ K - 413\ K$ [63]. At lower temperatures the temperature control of the radiation shields would need to be improved to ensure consistency of the experiment. In general the setup is very adaptable in different temperature ranges.

The steady state method has also been used to investigate the effects of multilayer insulation (MLI) [64]. A central heater, surrounded by 40 layers of MLI is placed in a liquid nitrogen bath. The MLI was investigated both in the 'ideal' setup with the reflective layers being arranged the same way round, and the 'non-ideal' arrangement where the direction of the reflective layer was mixed. Once the thermal equilibrium was reached, the evaporation rate of liquid nitrogen became constant over a period of a few days. This evaporation rate was used alongside heater data to deduce information on the MLI. This experiment gives an estimated uncertainty of 5%, remarkably low for the apparent lack of ability to control the evaporation rate due to surrounding room conditions. Application of MLI to the radiation shields is used for passive cooling in space missions such as the Cassini spacecraft [65]. For measurements carried out above 300 K, radiation losses pose a huge problem and this requires changes in the experimental setup [66].

For many measurements, heat loss from the sample surfaces has been reduced. In 1911, Poensgen introduced low conductivity 'packing' and an annular copper guard so that all heat from the hot plate travels through the sample (figure 3.5). This technique has been further developed, and is currently referred to as 'Guarded Hot Plate' (GHP). A guard ring is incorporated to prevent lateral heat loss from the test area, and the contained heat flows normal to the sample faces,

as illustrated in figure 3.4. Other insulation such as wool or block insulation can also be incorporated to ensure the sample is isolated, thus addressing these heat loss problems [67].

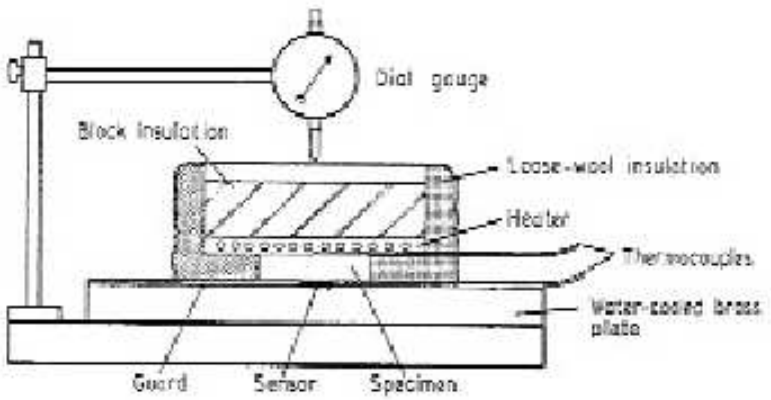

Figure 3.4: Guarded hot plate design for thermal conductivity measurements [67].

Accurate control of the guard ring temperature is required to ensure the specimen reaches steady-state; depending on the sample this may take days. Thermocouples attached at both ends of the sample monitor heat flow. The GHP has two configurations; either the sample is contained within the heat sink [68] so a guard ring may not be required; or a heater can be implemented in this experimental design [69]. The introduction of the guard to the system allows more accurate measurements to be made on thicker samples as one of the main problems with a larger sample is a larger surface area from which heat can be lost, especially for materials with a high emissivity. The width of the guard should be 'at least $0.25\times$ the width of the measuring area and no less than the specimen for effective shielding' [69].

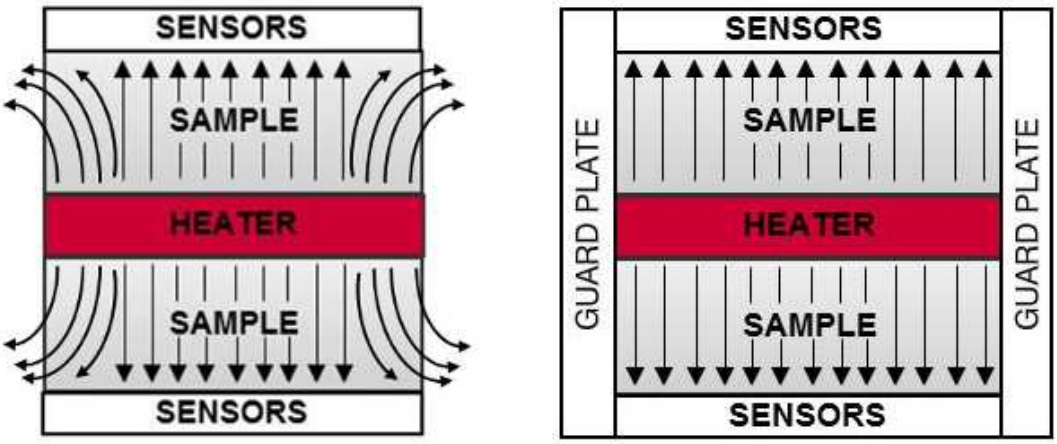

Figure 3.5: Guarded hot plate design: (a) unguarded setup and (b) guarded setup.

The overall design has not changed significantly since the 1950's [70]. Improvements in technique between the work shown by Dickson (1973) [67] and Salmon (2001) [69] relate mainly to advancements in technology over the 28 years between publication of the respective papers and specifically to improvements in the design aspects for maintaining controlled temperatures by minimising heat lost to the surroundings. Advancements due to more accurate instrumentation and accessories, the incorporation of computer systems for data collection and analysis, improved temperature control systems and the adaption of experimental setup (i.e. thicker insulation is present) have led to an improvement in heat control.

Further investigation of guarding techniques has been conducted using powders as a guard, as illustrated in figure 3.6 [54]. This powder is intended to absorb radiation; it also gives an indication of how radiative effects increase at higher temperatures. A more modern example of powder filler is fibre frax (a ceramic filler) which alongside more careful control of the thermal shields reduces the radiative effects.

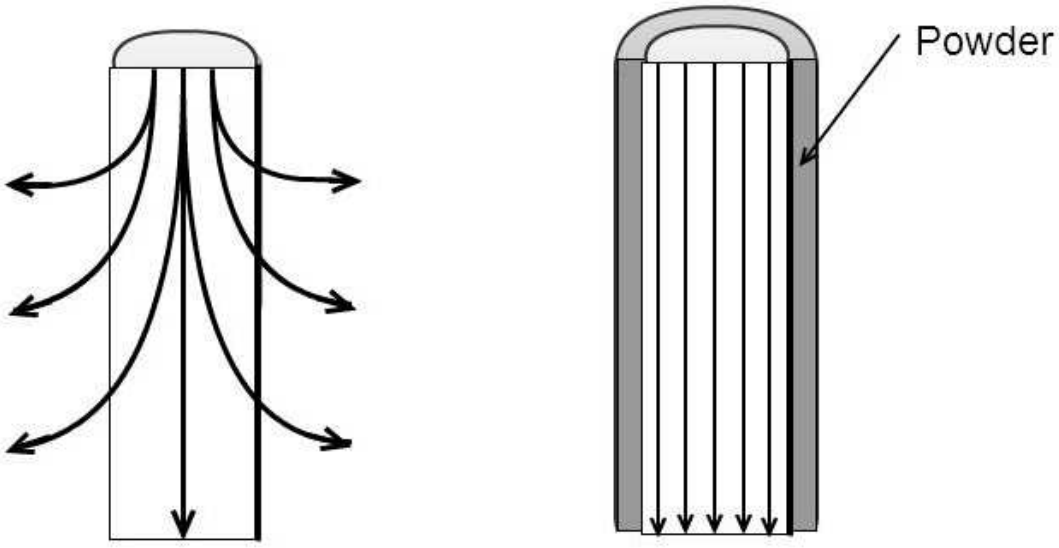

Figure 3.6: Unguarded and guarded samples using powder filling to reduce radiative loss.

3.2 Transient methods

Transient methods of thermal conductivity measurements involve small temperature fluctuations being implemented over very short timescales and the resultant change in wave properties being analysed. Short timescales are mandatory. Developments in computing power have resulted in increased use of transient methods for measuring thermal conductivity. High volumes of data are collected for each experiment, with measurements being taken multiple times per second.

The general experimental configuration consists of two elements which act as a heater and a temperature sensor. For solid materials, the elements are either embedded in to the material or are transposed on to the surface. If a liquid or powder sample is being tested, it is suspended in the sample. Some experiments use two separate wires for the heater and temperature sensor where others use one wire acting for both purposes. Stepped electrical current is introduced to

the heater wire at millisecond intervals. The corresponding time-dependant temperature rise is recorded. It is due to these short measurement time-scales that sophisticated computing facilities are required. The heat source outputs heat from its full length which conducts radially outwards. The temperature rise at radius, r, from the heat source can be given as:

$$\Delta T_(r,t) = \frac{P}{4\pi\lambda} \ln\left(\frac{4at}{r^2 C}\right), \tag{3.2}$$

where P is the power, λ the thermal conductivity, a the thermal diffusivity, t the time constant and C is Eular's constant.

Long wires increase the test area which increases the accuracy of the measurements. This method gives a 2D heat-conduction solution where the average temperature rise is associated with the thermophysical properties as well as size of wire, coating and sample.

If an electrically conducting or corrosive substance is tested, the wires must be coated in an electrically insulating coating or anti-corrosive coating respectively. Many experiments avoid testing such substances due to these factors, so materials could be less useful in large instruments as all surrounding materials would need to meet the electrical and anti-corrosive properties. Transient methods eliminate error due to convection as measurements are obtained in a thermally closed system. Sensor calibration data are used to calculate the temperature changes within the system. The following sections give further detail of some of the transient methods developed for thermal conductivity measurements at cryogenic temperatures.

3.2.1 Transient hot wire

The Transient Hot Wire (THW) technique was developed to meet the requirements of the thermal engineering field. A cell containing two thin wires, used as a heater and temperature sensor, can be set up easily with data acquisition software to supply heat to the system quickly and accurately and to record temperature changes in the system. The linear relation between the temperature rise and the logarithmic time can be used to calculate the thermal conductivity [71].

3.2.2 Short hot wire

The Short Hot Wire (SHW) technique is a variant of the THW experiments: the experimental setup consists of a single metal wire (as opposed to the two wires used in THW experiments) running through the test specimen. This wire acts both as a heater and a resistance thermometer [72]. This is a method of determining thermal conductivity and thermal diffusivity simultaneously in liquids, solids and powders. One big advantage it has for fluids is the elimination of convective error which would be present if using the steady state method [71].

3.2.3 Transient plane source

The same method has been used to measure larger surface sections using the Transient Plane Source (TPS) method. Here a heater/thermometer resistive element is produced and 'sandwiched' between two pieces of a sample. When heat is applied, a transient thermal wave travels to the surface of the material, monitored by recording voltage variations [73]. The thermal conductivity of thin film insulating materials has been measured using the same process [74].

3.2.4 Angstrom Method

This method, determined by Angstrom in 1863, involves heating a bar sample at one end using a low-frequency sine-wave generator to propagate a thermal wave through the sample. To measure the thermal diffusivity, the amplitude and phase of this wave at any point is measured and the properties of the sample are used alongside the wave properties to calculate the thermal diffusivity [75]. To avoid heat loss by convection, the heater used should be approximately the same diameter as the sample. Temperature variations of up to 2 K can be seen at 300 K. The signal generator can detect a measurable sinusoidal wave which can be used as the reference wave before heat is applied. Low-noise amplifiers and bandpass filters can be used to improve the signal-to-noise ratio if required. If a higher frequency of wave is used, radiation effects can be reduced therefore shorter samples can be measured. [76]

3.2.5 3ω Method

The 3ω technique developed by Cahill and Pohl in 1986 [77] is an AC technique very similar to the SHW method. A metal strip in perfect thermal contact with the sample, achieved by photolithography or evaporation of the metal, is used as a heater and a temperature sensor simultaneously (figure 3.7). The SHW and THW techniques both consist of measurements made in the time-domain, whereas the 3ω method uses lock-in amplifiers to conduct measurements in the frequency-domain. As power is applied to the metal strip, the amplitude and phase of the resistance changes are measured as a function of excitation frequency. The 3ω method creates a time-harmonic temperature variation within a solid material which when measured can be used to create a 1D heat conduction model and hence the thermal conductivity can be calculated. Again, the setup has to incorporate the ability to measure at millisecond intervals.

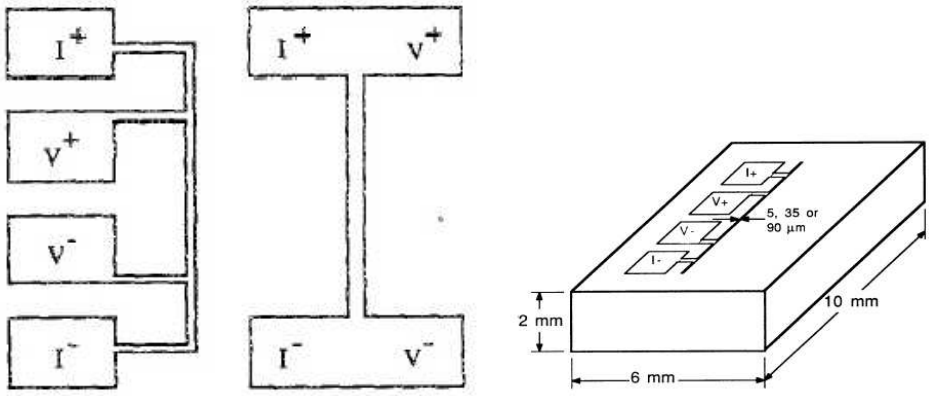

(a) (b)

Figure 3.7: 3ω setup (a) Two options of track design of heater/thermometer module [78] (b) heater/thermometer module on sample surface [77].

3.2.6 Other techniques

Many variants of the steady state and transient methods described previously have been used to determine the thermal conductivity of materials. We will now briefly list some of the less common methods.

Series comparative

Thermistors arranged in matched pairs (using the Godson technique) have been used in a Wheatstone Bridge [79]. A comparison can be calculated between the balanced system with zero heat flow and the unbalanced system when heat flows. As the resistance of the thermistors is known, the temperature can be calculated for a given resistance and hence ΔT can be determined, yielding an estimate of the thermal conductivity, λ [79]. The cited work was carried out above room temperature and the error in λ is remarkably high at 16%. As this work was conducted almost 50 years ago, the system could potentially be improved due to developments in technology, computing power and data acquisition. Furthermore,

if the method was adapted for low temperatures this would reduce any radiative effects and convection (as a vacuum would be used), thus potentially reducing the total error in experimental data.

Inter-facial contact

The thermal conductivity of small samples can be measured by bringing them in contact with a hot copper bar and recording the temperature at the inter-facial contact. A few slightly differing methods have been used, including; decay of temperature between two hot balls [80]; and using a heater consisting of a U-shaped capillary filled with liquid, low-melting point alloy as a heater [81]. Varying sizes of conductors will have different stabilisation times, but above room temperature this time constant can be as low as 30s. Although an accuracy of 5% has been achieved by Zie (1963), there are many inconsistencies in the experiment such as: pressure of inter-facial contact; material structure; heat transfer from human hand to rock interface; and definition of stable temperature.

One complication is the difficulty of achieving an ideal thermal contact. The surfaces need to be smooth at a microscopic level, or a conducting gel could be used between the heater and sample. Furthermore, to adapt this method for use at cryogenic temperatures, one would need to develop a mechanical arm to bring the sample into contact with the heater. This would be one way of normalising the pressure of contact and removes the issue of heat transfer from human to sample. The heater could be mechanised electronically instead of containing liquid alloy and both time constants and temperatures can be recorded by a specialist computer and data acquisition system. This would give more accurate results as temperature conversions would be done to a higher degree of accuracy using suitable computer algorithms.

Two probe

Thermal conductivity (at cryogenic temperatures) of two tin wires has been measured using a thin film resistor connected to a resistance bridge, as both a heater and temperature control [56]. Two wires are attached across a temperature controlled ring (see figure 3.8) with a temperature sensor at the central point and a second sensor monitoring the temperature of the ring. The wires are connected in a 4-wire arrangement and are electrically isolated from the ring, but with a good thermal contact. The setup as shown in Ventura et. al allows for changing the geometrical factor, and testing electrically conducting materials and in general has an appealing flexibility. The experimental arrangement has already been proven to be accurate at cryogenic temperatures. Unfortunately, this method is not easily adapted for bar samples: the heat distribution would not be uniform at short time constants, and more power would be required than the resistance bridge can provide in order to ensure accurate results over a large temperature distribution.

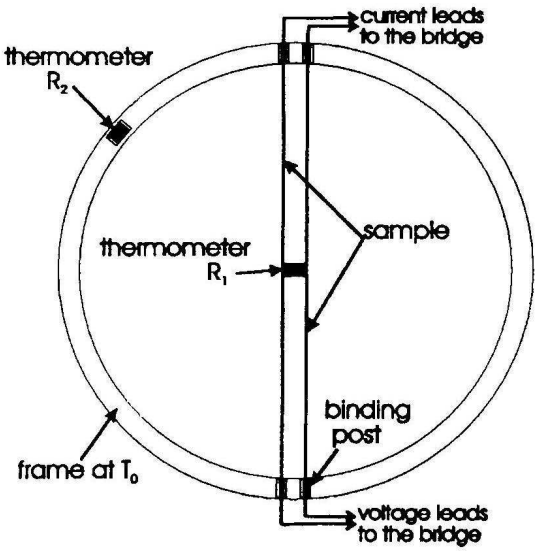

Figure 3.8: The experimental setup as used by Ventura et. al for making thermal conductivity measurements using the two-probe method.

3.3 Conclusions and method to proceed with for thermal conductivity measurements

Various methods have been developed to improve the accuracy and breadth of the knowledge base available to scientists and engineers for designing and developing new projects. In particular Laubitz gave a detailed review of eight systems measuring a range of materials at high temperatures (100-1200 K) which provided a great insight to the capabilities of the available technology as well as highlighting some of the associated problems [82]. Applying this at cryogenic temperatures creates additional problems and introduces new challenges which have been addressed by various researchers. Methods have been developed for testing solids, liquids and gases. Although each measurement is an achievement in itself, many of these were unsuitable for the task in hand with the project contained in this thesis. The samples to be tested for this project were all solid in form and small (although not on the nano-scale). The steady state longitudinal method was identified as the most suitable setup for bulk measurements and the 3ω method for surface property measurements. These two methods have not previously been used simultaneously, or when set up in the same configuration, but if this was achieved it would offer a more in depth analysis of a single sample.

The following chapter examines in more detail some of the variations within published data and the reasons therin. This will help assist the experimental procedures detailed in later chapters.

Chapter 4

Review of thermal conductivity data from the literature

This chapter discusses the necessity, availability and quality of low temperature material properties. Information in existing literature studies are collated, analysed and reviewed, resulting in a cohesive source for future instrumentation development.

4.1 Overview and aims

Knowledge of the physical properties of construction materials at low temperatures is of utmost importance when designing instruments. It is necessary to gain a full understanding of thermal conductivity, electrical resistivity, specific heat and magnetism as well as other factors that can influence both the design and function. These properties need to be known as a function of temperature for successful integration into systems that can provide optimum results for the

designated purpose. Due to long time scales for gathering these results and the specialist equipment needed to carry out the experiment, many current designs are based on measurements made in the past on different systems or for specific purposes. The CUORE cryostat for double beta decay experiments [83] has been investigating thermal properties of materials during the construction of the first CUORE tower, CUORICINO [84]. CUORICINO has been produced to confirm the science goals set out for CUORE and has thus far been successful. Parts of the experiment are supported with rods, so two materials were tested for suitability: Ti_6Al_4V alloy and Stainless Steel 316LN [85]. Furthermore, supports for the crystal absorbers needed to be developed for operation at 10 mK. Polypropylene copolymer (PP) was tested [61] as it was expected to have similar properties to materials such as Vespel, Torlon and Kevlar which had been used in previous experiments. These tests were all carried out in the construction period of the CUORE instrument.

This lack of empirical study can have an adverse effect on the quality and reliability of overall results, as the material may not have been tested in an appropriate manner for the planned project. In order for these designs and projects to be successful, the physical properties of materials must be known. It is of paramount importance that there is correct information in the literature to which engineering teams can refer. Data printed in the literature also act as a guideline for further characterisation of materials. This chapter aims to provide a review of commonly used data in literature discussing variation between samples, justification of data extrapolation and the equipment used to gather the information. Thermal conductivity is eminently important, as even the slightest change in temperature can have a huge effect on the behaviour of its surroundings. Both materials of high and low thermal conductivity are required. Thermal conductivity will thus be the main focus of this chapter of research. This review is the beginning of a cohesive source of information on the thermal conductivity of

nylon, kapton, boron-doped silicon and stainless steel 316 in the 0.1 K to 100 K temperature range.

4.1.1 Currently available information

Information is available from many sources in printed texts, on the internet and directly from industrial sources. The collection of these results has been performed by a vast number of people using different equipment and utilising varying methodologies. One problem we face is that it is, at times, very hard to trace back the citations to discover the exact composition of the material or the laboratory where the work was carried out. If the systematic errors are not fully investigated and discussed, it reduces the confidence that the laboratory in question can have fully investigated and reduced these issues. These details are very important in gaining the overall picture of the analysis. All information published should have comprehensive and correct details of the materials studied, including the chosen samples' composition. Information currently released by some industrial companies is known to be missing some key facts regarding the material and/or the method of measurement.

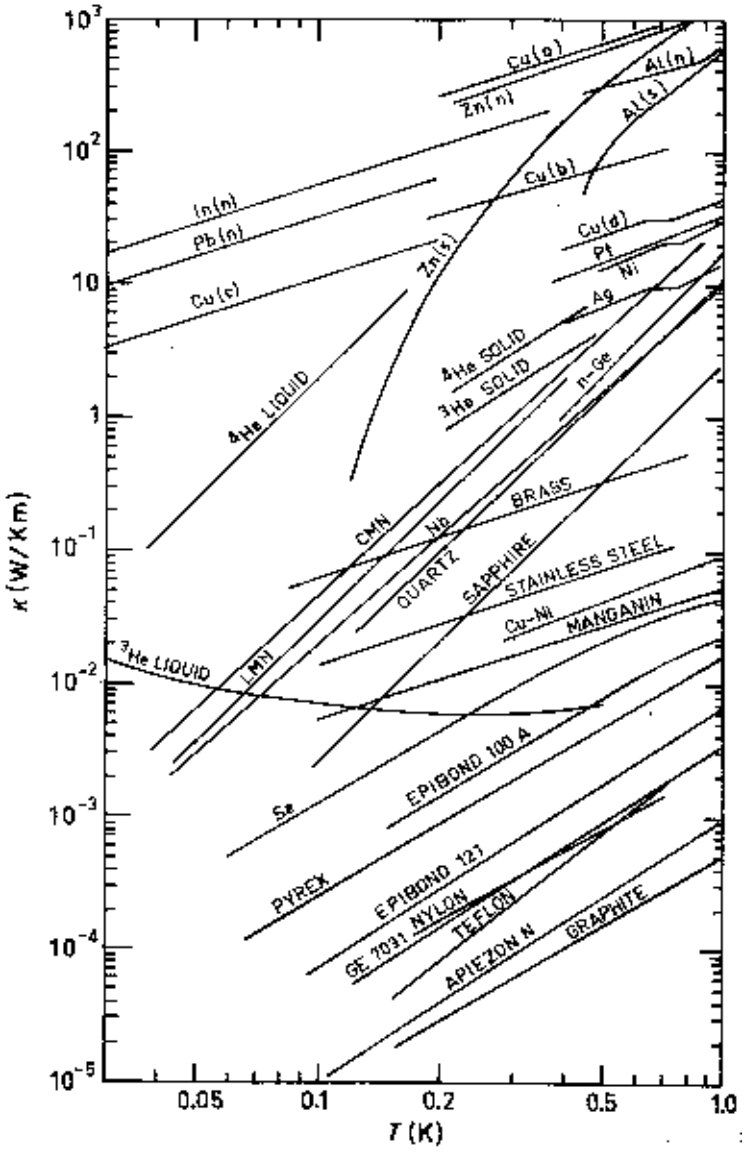

Figure 4.1: The thermal conductivity as fit of temperature of several materials below 1 K as published in Louanasmaa (1973) [86]. Data have been compiled from research papers dating back to 1952 and the graph is now used in various printed texts. Some of the data included in the graph may not give a true view of the material behaviour, such as the lines for Cu(d), Ni and Ag which all show an unexplained 'drop' at approximately 0.7 K.

There are extensive sources throughout the literature, but this analysis will focus on two areas: data below 1 K and the 3-30 K range. In 1973 Louanasmaa showed a detailed study of several materials at millikelvin temperatures [86]. The graph, as depicted in figure 4.1, has since been used in various other publications e.g. [13], [51] and partial data have been used in [87] and [88]. Selected data from this work have been used extensively, but little effort has been made to critically examine these results prior to publication. Papers used to compile this graph date back as far as 1952 and hence are now very difficult to acquire unless access to the original sources can be granted. Since this work was completed there has been an evolution of both instrumentation and the scientific/academic understanding of material science. Methods for gathering data have become more efficient owing to these improvements, resulting in questions regarding the accuracy of Louanasmaa's graph (amongst others). There is a prominent lack of complete data as most data is available either near to room temperature or at specific points such as 4 K and 77 K.

Compilations of data

Many compilations of thermal conductivity data have been made over the last few decades. Compendiums such as that of Louanasmaa, Rosenberg [89] and Rose-Innes [90] offer a collection of data on a variety of materials; metals, polymers, technical alloys and glass. Other compilations have been carried out which are slightly more focused, such as White's treasury of amorphous solids and powder insulators [87] or Pobells's compilation of dielectric materials [51].

Information is often lost in translation between sources: when secondary references are used it is, at times, difficult to source the original publication. Data will be extracted from textbooks without the original work necessarily being retrieved. Much original data have been hidden over the years within later

research. Some would argue that this full information will also become lost over the next few decades, but this too is a problem we need to solve. If we can provide structured, correct data and make the literature available to all, then we can potentially decrease these problems.

Aside from textbooks, material property data are published on the World Wide Web and in research papers worldwide. Some industrial companies release data on certain products, though this is generally very basic or limited data [91]. There is a prominent lack of complete information, especially when nearing 300 K as it is more complicated to ascertain.

On initial examination of Louanasmaa's graph, a few potential issues arise; particularly with the requirement on the reader to search back to the original papers to find the particulars of the material or experimental method. Firstly, Brass is shown without a precise description of the composition; the implication of different compositions can be drastic for low temperature thermal conductivity [92]. Likewise Manganin, as indicated on the graph, is a thermal conductivity derived from electrical resistivity using the Weidermann-Franz Law (section 2.6.1): this only takes conductivity due to electrons into consideration, while phonon conduction is also relevant at these low temperatures [93]. Four different copper samples are shown, with the higher purity copper having the lower conductivity. Silver, Nickel and Copper (d) [94], [95] all show an unexplained 'drop' at approximately 0.7 K which on first investigation seems strange for two reasons: the other copper samples show no anomaly at this temperature; and silver, nickel and copper belong to different families of materials so they would not be expected to show a fluctuation at the same point.

4.1.2 Reliability of information?

Many people will search for data on a specific material, take a value from a 'trusted' source and proceed with their work. The engineer may think they have a reliable source, but depending on the difference in requirements between the original work and their experiment this could be a fatal error of judgement. Scientific theory suggests that we can only fully trust information that has been obtained through the use of a specialist system, with details of the full material specifications and allowing the experiment to be repeated if necessary. Obviously many complex instruments are made every year and much information currently available can be used, as demonstrated in projects such as Hubble Space Telescope. More recently, SCUBA-2 has been developed requiring mechanical supports between different stage temperatures and thermal links to the main mechanical systems [96]. Research was carried out on potential changes to some of the thermal links in the system, as there were issues surrounding the ability to connect the ends to the main body of the instrument.

4.1.3 Resolving issues arising from inaccuracies

Further to the explanation above, there are ways to resolve the problems surrounding inaccurate data being used during the design and manufacture processes of instruments. Many of the published compilations offer no analysis as to *why* the values vary. At times the compilations are there only to show general trends of materials and not the specific properties. The suggestion of the present work is that for each chosen material the known measurements can be used alongside a chemical knowledge of the material at low temperatures to produce recommended data regarding the material. This information can then be used to assist with planning material characterisation tests on specialist equipment to solidify this knowledge experimentally. As data would be collected from as many sources as

possible there would be a wide range of experimental procedures covered – so the systems involved would be also analysed. Potentially erroneous results should be analysed further to avoid including data taken, for example, by unjustly extrapolated results. This offers a more robust fit of recommended results, and in conclusion there would be less error in future experimental work.

4.2 Method of analysis

As many of the results that require analysing are only available in paper format, the published papers were scanned and digitised using WinDig™ [97] and Engauge Digitiser [98]. These programs offer a simple way to recreate data originally produced by people and groups who may no longer be in the field. The data collected by digitisation can be collated with data received from companies/research groups and other sources. This can then be analysed using knowledge of the material and the predicted properties in the given range. The accuracy of the digitising method shows that results from a paper can be recreated to an accuracy of 1%; this is typical of the results used here. The papers collated for each material are referenced in the individual sections.

4.2.1 Focus of analysis

As the Louanasmaa graph has been used extensively over the last few decades, the discussion here focuses on materials contained therein. Due to time constraints, not all materials contained in the graph were examined, and access to data sources was at times limited. The materials focused on were: Stainless Steel 316, Boron doped Silicon, Nylon and Kapton. Stainless steel 316 was examined as it is the experimental standard used in the work contained in this thesis. Boron doped silicon is of interest for Gravitational wave detectors and both Nylon and Kapton

are increasingly used in cryogenic instrumentation.

4.2.2 Stainless steel 316

Stainless steel is an austenitic stainless steel (maximum 15% carbon, minimum 16% chromium) and is a widely used material in construction of cryogenic instruments. Various compositions exist, described by the numbers included in the name. Here I will look at stainless steel 316, a readily available stainless steel used as a standard in the experimental work carried out for this thesis.

As the different grades of stainless steel have different compositions, mainly with a difference in the contained quantity of nickel and chromium. This accounts for the range of thermal conductivity values [99]. As stainless steels are in mass production and are sold in the different grades, there is a lot of continuity between different batches. One of the more recent research projects focuses on which material to use for the CUORE suspensions and whether stainless steel is more suited than a polymer such as kevlar [100] [101]. This also highlights the forthcoming uses of polymers in large projects, whereas in the past less polymers were implemented.

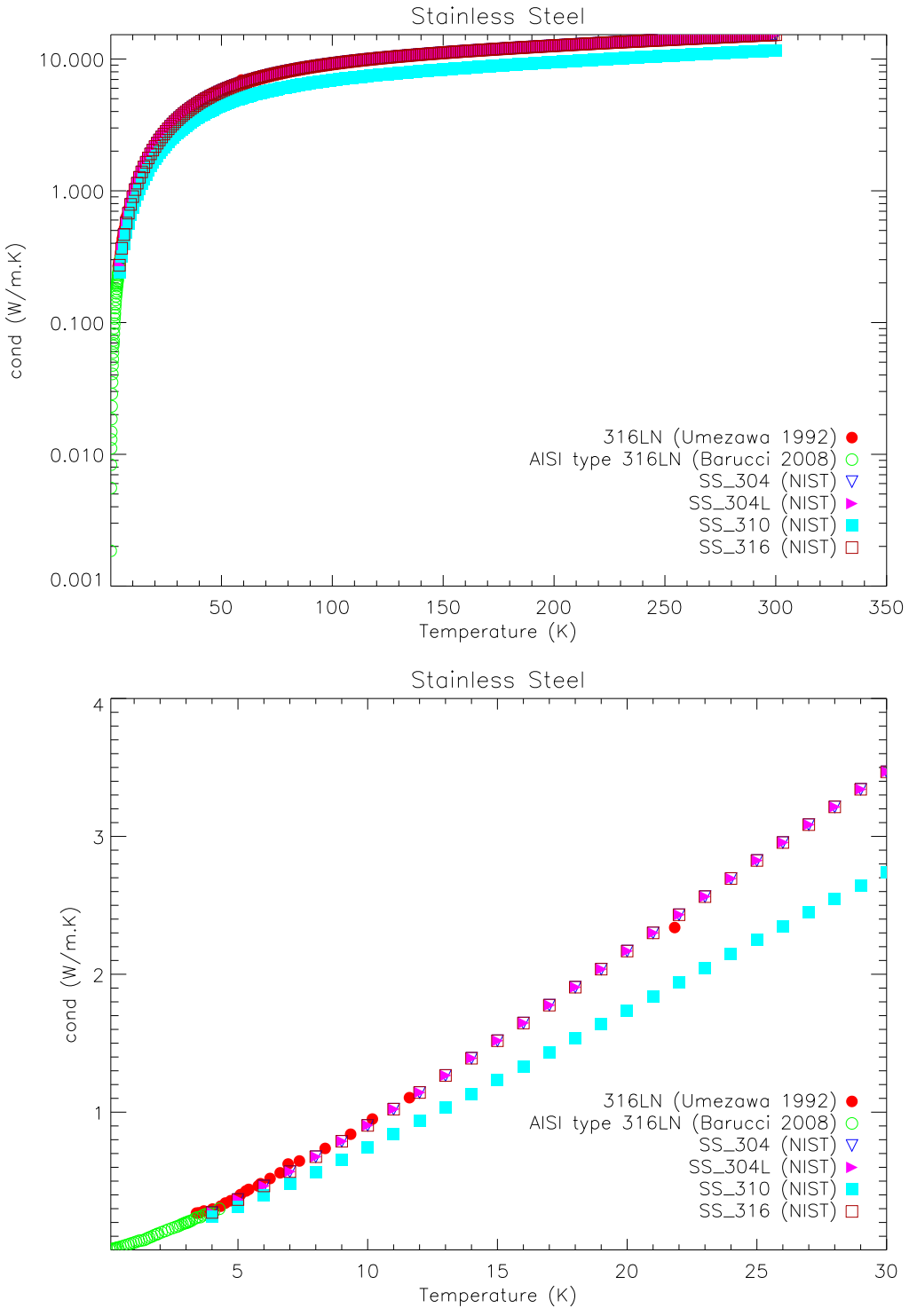

Figure 4.2: Thermal conductivity of Stainless Steel 316 (a) up to 300 K and (b) up to 30 K. Original experimental data from [85] [91] [102].

Austenitic stainless steel is the most widely used type of stainless steel making up over 70% of the total. It is manufactured to the following specification: maximum 0.15% carbon, minimum 16% chromium and finally if they contain enough nickel/manganese to retain austenitic structure. Of the austenitic grades, stainless steel's 304 and 316 are the most common. Grade 316 has an addition of molybdenum to prevent types of corrosion and is also more resistant to chlorine corrosion than some other grades. If the grade contains the letter 'L', it is the low carbon version of the grade and and 'N' denotes a nitrogen-strengthened stainless steel.

It can be seen from figure 4.2 that data for stainless steel has a consistent trend. The main variation below 30 K is the lower thermal conductivity of stainless steel 310. As the number in the stainless steel code defines its composition, this slight difference is not surprising; grade 316 has molybdenum content which grade 304 does not. It can also be seen that the experimental data collected by Umezawa and Ishikawa (1992) and Barruci et. al (2002) is in good agreement with the NIST data

Further data exists for stainless steel, but due to the high constraints on manufacturing for use in industry and the widespread uses, there is much more data available on thermal conductivity. The general processes for preparation for different grades and properties of grades are depicted in [103].

4.2.3 Boron-doped silicon

Boron-doped silicon is of interest as it is one of the substances to be tested for the work contained in this thesis. As discussed in section 2.1.2, the level of doping can have a significant effect on thermal properties of a material. Boron-doped silicon is proposed for use in Gravitational wave detectors, and the materials are purchased with specified doping levels. Each batch of silicon produced will

meet these requirements, to the stated doping standard, and each batch will be tested for continuity between batches before implementation in to systems. The boron for Gravitational wave detectors has the surface oxidised to aid the bonding technique used.

The samples shown in figure 4.3 have a wide variety of compositions, with both n-type and p-type semiconductors as well as boron and phosphorous doped. This accounts for the range of conductivity values for the majority of data shown, but there is still an inconsistency of more than one order of magnitude for pure silicon below 20 K [104] [105].

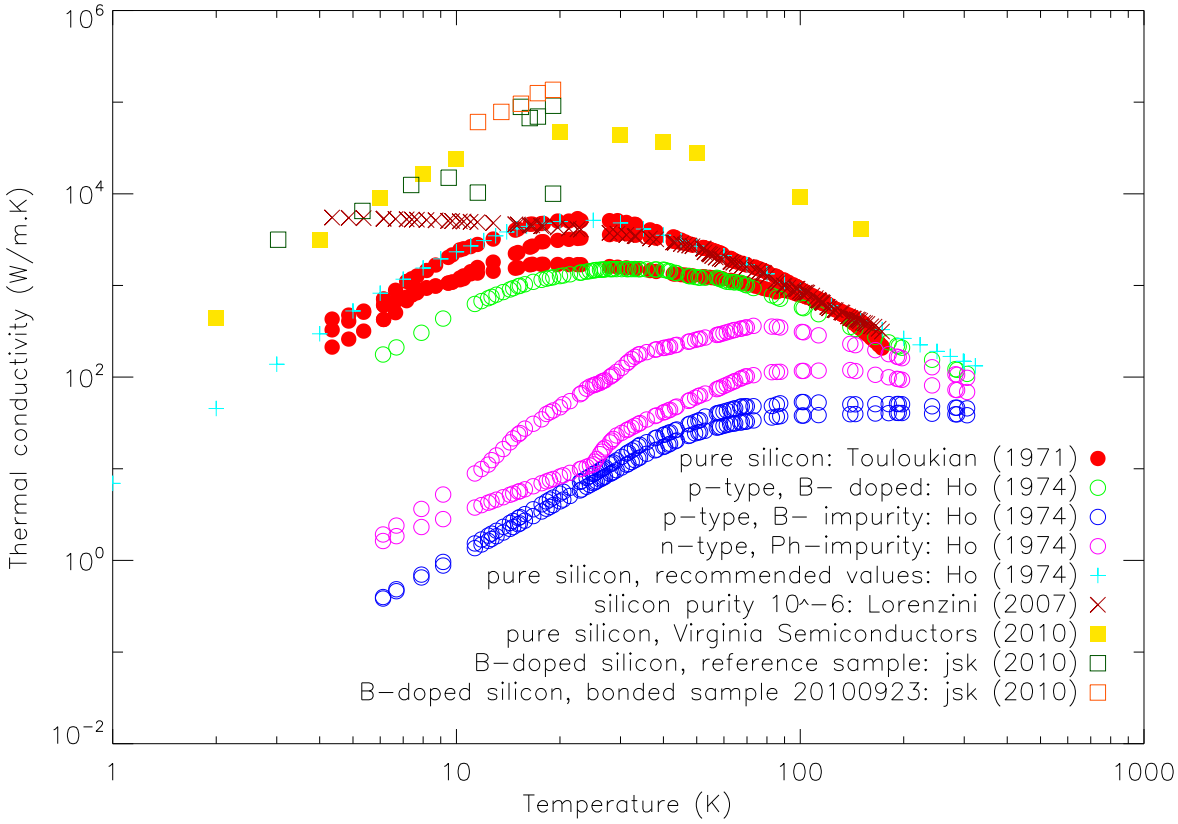

Figure 4.3: Thermal conductivity of boron doped silicon. Original experimental data by: [105], and experimental work contained in section 7.3.1. Secondary sources: [106] and [104].

The silicon tested in the experimental work contained within this thesis is p-type boron doped silicon and it can be seen that at 10 K there are 4 orders of magnitude difference in the thermal conductivity. A comprehensive review of silicon can be found in [104] but the data originates from a variety of laboratories so no information is available about the type of measurement, although from the information given about the sample dimensions it is assumed steady-state measurements were conducted. Different doping levels could have this effect on results, highlighting the importance of knowing the doping levels of each sam-

ple used. Companies which produce doped samples will provide a certificate of authentication of doping levels, although to receive a sample with very precise doping costs a vast amount more than one provided with doping in a larger range.

4.2.4 Kapton polyimide film

Kapton is a polyimide: a heat resistant polymer with high elasticity which is durable, reliable and an excellent choice for use within low temperature conditions. It is commonly used to secure electrical wires and insulation, but is also used in larger instruments in space research due to its excellent mechanical and electrical properties. Ribbon cables have been successfully made using Kapton as a base and running tracks of an electrically conducting material along as wires [107].

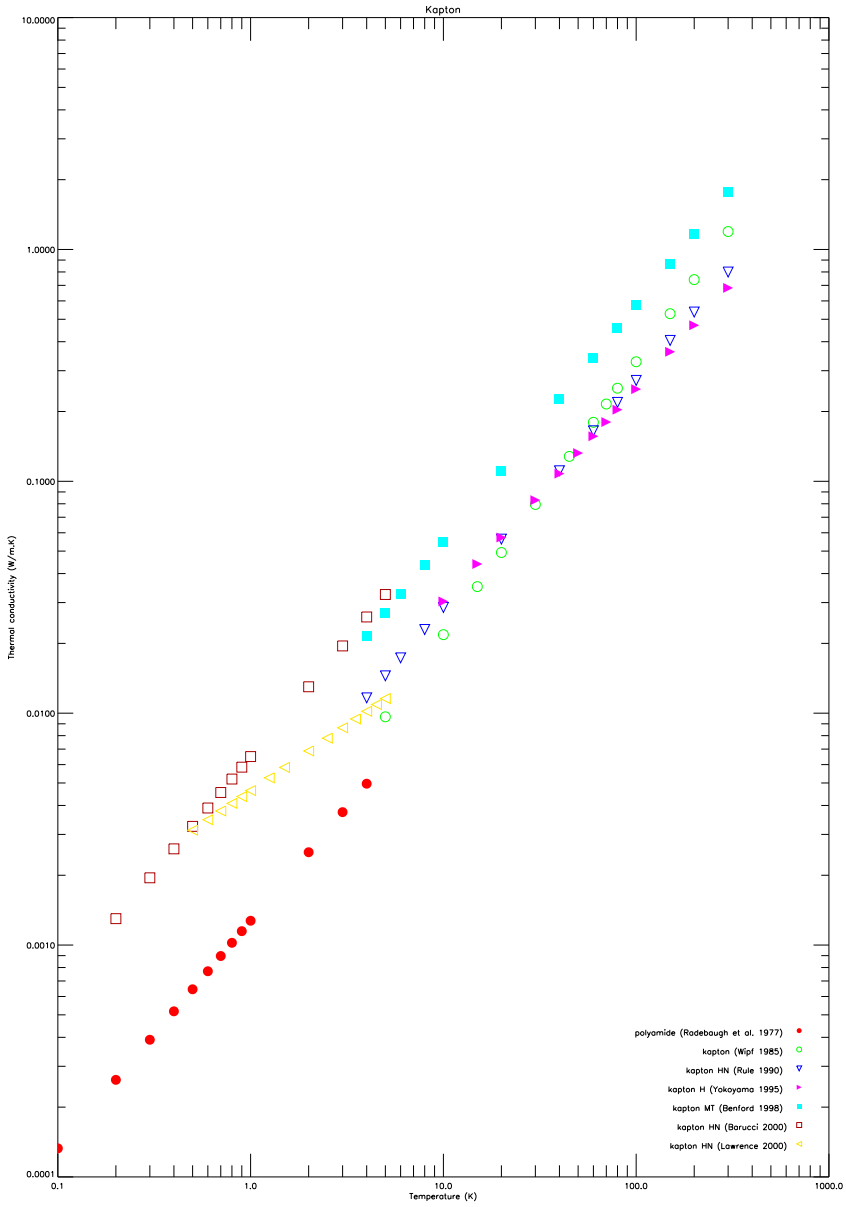

Figure 4.4: Thermal conductivity of Kapton with data points from [108], [109], [110], [111], [107], [112] and [113] with secondary sources from [110].

Although Kapton polyimide is a commonly used material, it can be seen from figure 4.4 that there is still a large disparity between results, as much as 83% difference at 0.2 K [114] [112]. Part of this inconsistency is believed to be due to

different forms of Kapton being measured, but as two of the laboratories measure Kapton HN, and although at 0.5 K they are in agreement, at all temperatures above this they are in disagreement [113] [112]. Although the work was published in the same year, the difference in technique may account for this: Lawrence used short and long stacks of Kapton layers and measured the thermal conductivity through the surfaces, hence introducing contact resistance between layers; Barucci measured a single layer of Kapton attached to a hollow copper tube to avoid the additional resistance caused by stacking the film.

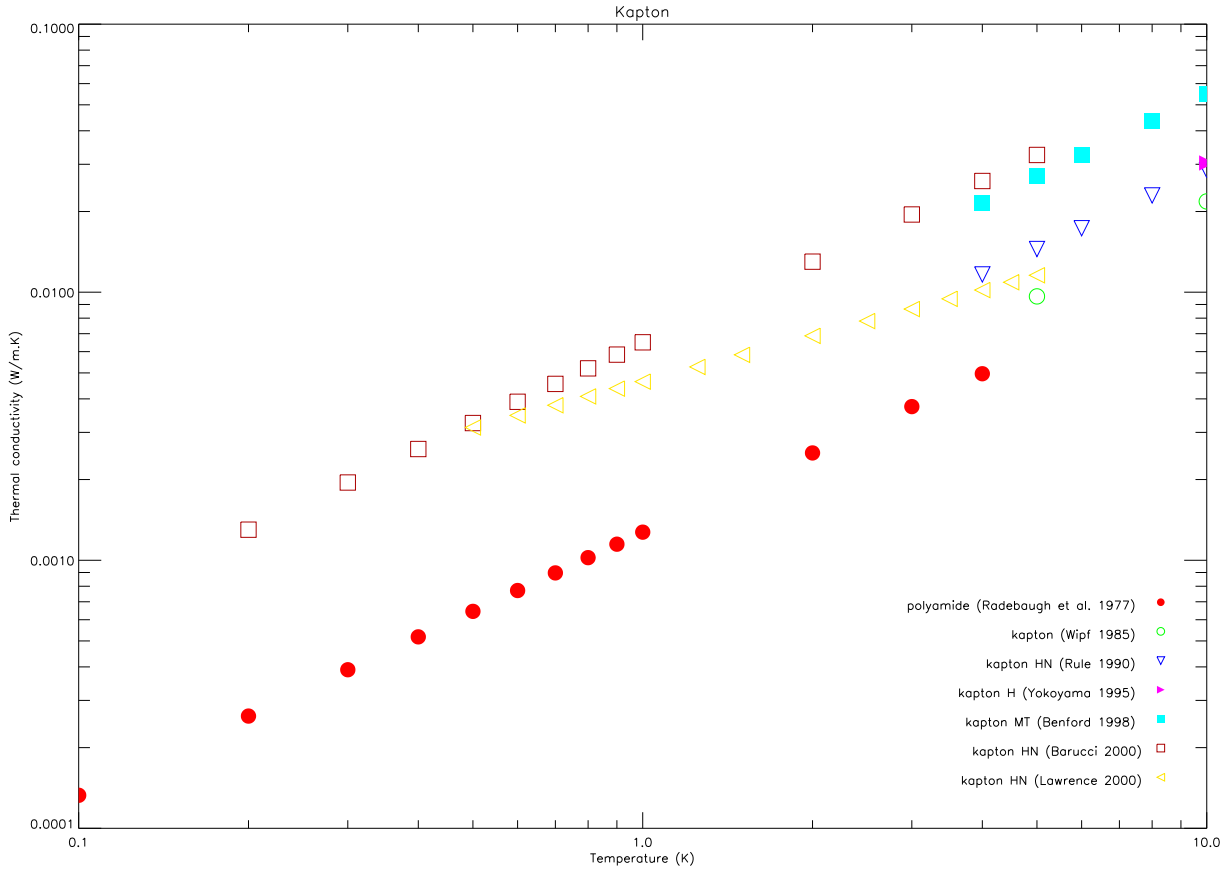

Figure 4.5: Thermal conductivity of Kapton below 10 K with data points from [108], [109], [111], [107], [112] and [113] with secondary sources from [110].

In many cases as the capability of instrumentation improves, the reproducibility of data also improves, but there is still this difference in experimental technique. For more recently published data is is possible to find more detail of experimental technique, which as previously mentioned can be a problem with older data such as is displayed in Louanasmaa (1973).

4.2.5 Nylon

Nylon is widely used as an insulating material and for support structures as it retains its high mechanical strength at low temperatures. Various compositions again exist for nylon, for example nylon-6 and nylon-66 with different lengths of repeating polymer chain. In later years, glass re-enforced nylon has been used as the addition of glass fibres creates a insulating material with even higher strength.

Although stated that there is agreement between data produced by different laboratories independent of the source of nylon [115], the work shown here would contradict that. On first examination, it appears there is a significant amount of agreement between the majority of results at low temperatures, as illustrated in figures 4.6 and 4.7, but the use of a log scale can be deceiving. For example, at 1 K there is a difference of 1×10^{-2} W/m K between Barucci (2000) and Scott (1973). 1×10^{-2} W/m K may not be much, but in an industry where the slightest incorrect calculation or implementation of material can be the difference between an instrument working or not, this is a huge value. As these laboratories both used the steady state heat flow method on a cylindrical sample, it is thought to be the glass fibres in the sample of Barucci which has made the difference.

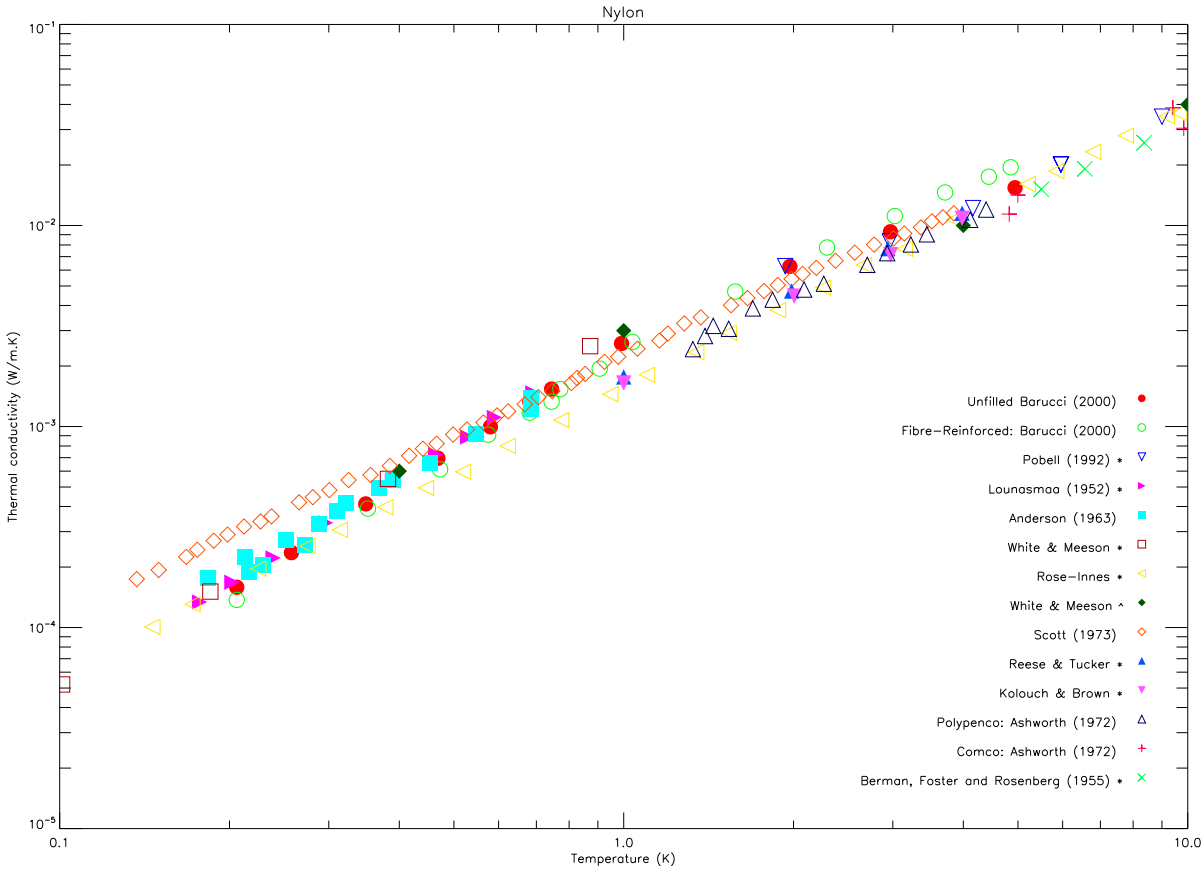

Figure 4.6: Thermal conductivity of nylon below 1K; Original experimental data by: Barucci: unfilled and fibre-reinforced nylon [116], Anderson [115], Scott [117] and Ashworth [54]. Values taken from a secondary source for: Pobell [51], Lounasmaa [86],White and Meeson [118], Rose-Innes [90], Ashworth [54], and finally Berman, Foster & Rosenberg [119].

Much of the data shown in the graphs is from prior to 1975. This makes a significant difference as the instrumentation and especially the support hardware used for data collection and analysis. State of the art hardware and software used for recent measurements increases the response time of heaters and the speed of data acquisition, meaning the confidence in measurements has been improved. Sen-

sors used have also been developed, meaning better thermal contact and response times can be used such as used for determining the low temperature thermal conductivity of materials such as Nylon-6/Cu nanoparticles, a new nanocomposite with potential use in future instruments [44].

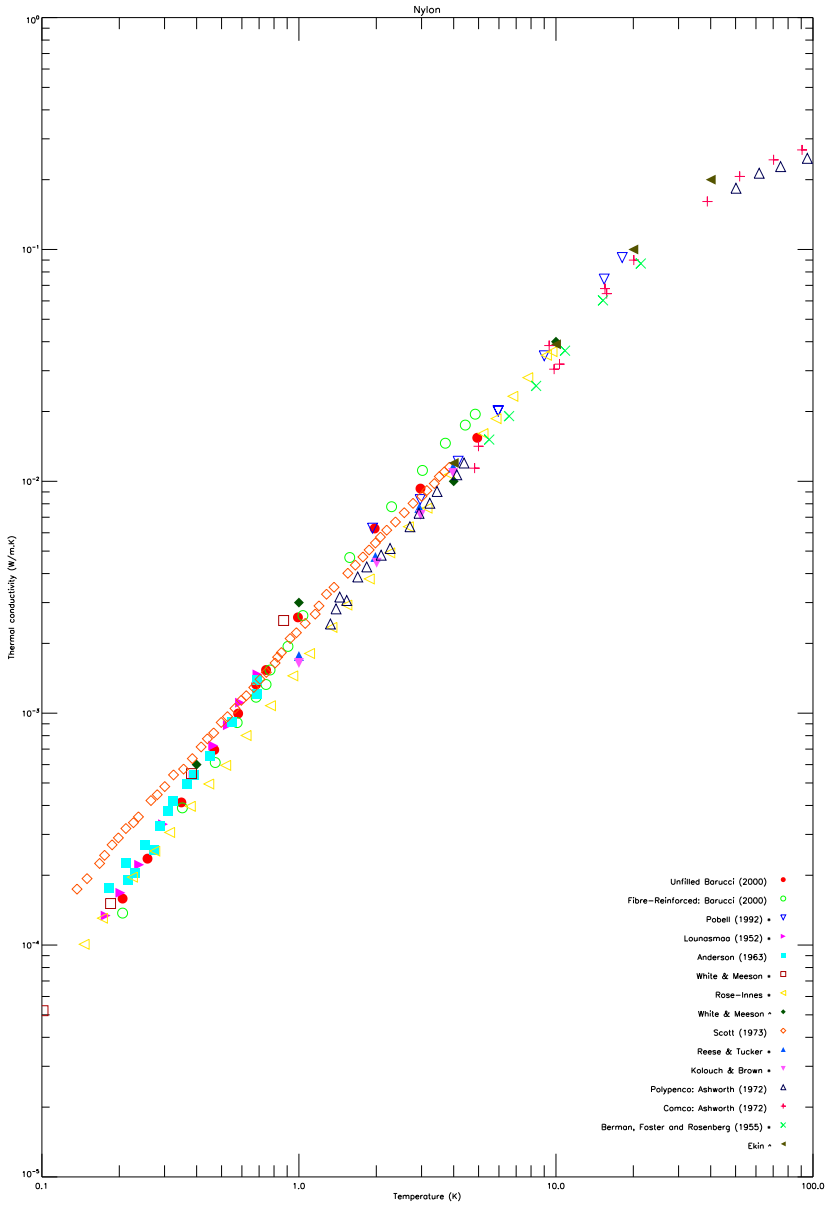

Figure 4.7: Thermal conductivity of nylon; Original experimental data by: Barucci: unfilled and fibre-reinforced nylon [116], Anderson [115], Scott [117] and Ashworth [54]. Values taken from a secondary source (indicated by a $*$) for: Pobell [51], Lounasmaa [86],White and Meeson [118], Rose-Innes [90], Ashworth [54], and finally Berman, Foster & Rosenberg [119].

The importance of using up-to-date information, collected for the designated purpose is required as there is variation in published data.

4.3 Conclusion

It has been highlighted here by using one commonly used construction and support material, stainless steel 316, one doped amorphous material, boron-doped silicon, and two polymers, nylon and kapton, that there is huge variety in published data for all types of material. As shown, there are a variety of reasons for this:

1. The level of doping, and knowledge of doping
2. Differences in experimental setup
3. Differences in support software (partly related to the decade results were obtained)
4. Experimental technique- as well as the differences in experimental setup, each scientist setting up a sample will do this slightly differently

so care must be taken not only to carry out the experiments as effectively as possible, but to make available fully documented information on the experiment so scientist either accessing the data or repeating the experiment have full knowledge.

The following chapters document the work completed on thermal conductivity measurements at low temperatures. The experimental work contained within this thesis has been fully documented in the main body with further details in the appendices so if experiments are repeated, the experimental conditions are known.

Chapter 5

Hardware and software

For thermal analysis experiments it is of paramount importance that a specialist system be built and characterised. This chapter describes the hardware and software used to carry out steady state thermal analysis of materials from 3 K to 30 K. This is followed by a description of the support hardware used to allow remote control and continuous monitoring of the system. Finally a number of suggestions for improving the system are discussed.

The cryostat used for these measurements is a Gifford McMahon cryocooler operating system as described in section 1.6.2 constructed by Janis Research company, Inc. [120] . This cryostat design is readily available and custom specifications can be stipulated before purchase.

5.1 Adopted experimental setup for thermal conductivity measurements

The capability of steady state methods have constantly improved through the last 50 years. These improvements, alongside the available computer facilities, made this the chosen method for thermal conductivity measurements for the work in this thesis. The cryostat to be used was a Gifford-McMahon system and the ideal configuration a sample on a removable cold head with maximum dimensions of 60 x 30 x 30 mm. Temperature sensors could be attached either directly to the sample or on removable mounts. Templates would be made for fitting of removable sensor blocks to ensure adjoining blocks are equally spaced. A variety of samples were to be tested, so an adaptable system was produced, but initially tests will only be carried out on $r = 20$ mm bar samples.

The following points were addressed when designing a sample holder and experimental setup for these experiments, as illustrated in figure 5.1:

1. Place to securely attach heater to top of sample.
2. Ability to position temperature sensor near the top of the material.
3. Ability to attach temperature sensor(s) near the centre of experimental setup, with the flexibility to move them when required.
4. Radiation shield and additional shielding (if required) to reduce radiative losses.
5. Method of fixing sample to the cold head.
6. Detachable sample mount.
7. Control of cold head temperature with temperature sensors built in to the cold head.

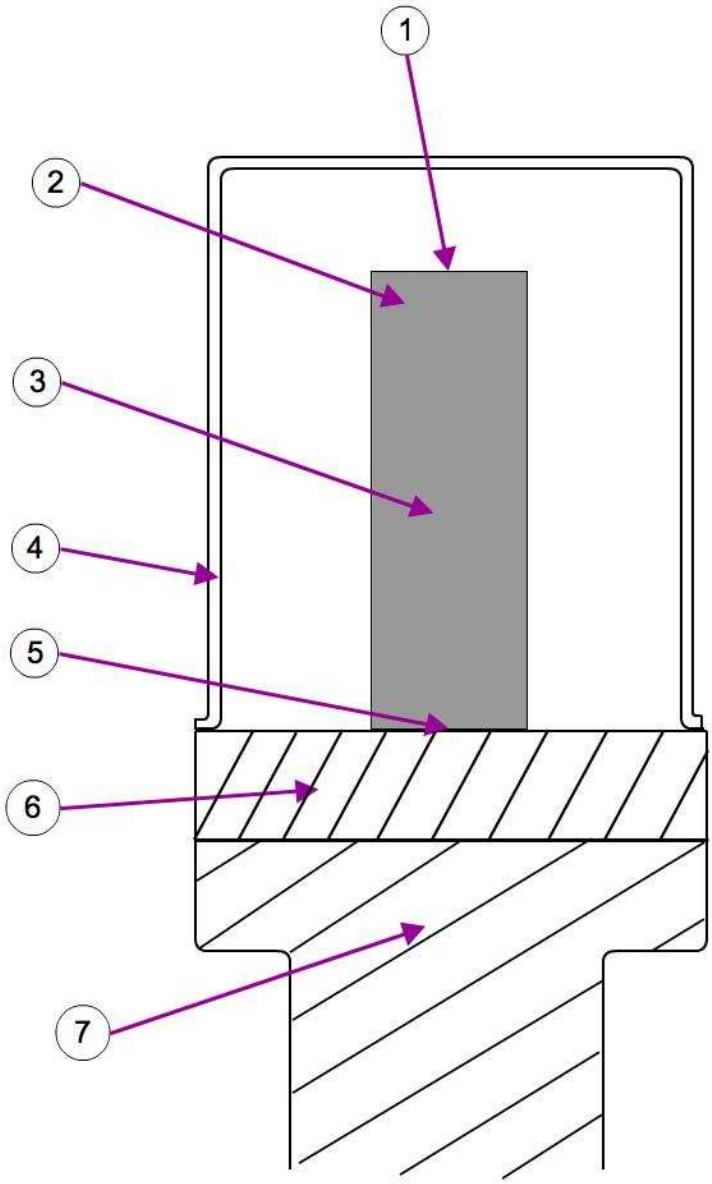

Figure 5.1: Ideal setup for steady state thermal conductivity measurements. (1) Place to securely attach heater to top of sample (2) Ability to position temperature sensor near the top of the material (3) Ability to attach temperature sensor(s) near the centre of experimental setup, with the flexibility to move them when required (4) Radiation shield and additional shielding (if required) to reduce radiative losses (5) Method of fixing sample to the cold head (6) Detachable sample mount (7) Control of cold head temperature with temperature sensors built in to the cold head.

The setup is based on the steady state longitudinal heat flow method. The exact configuration used to measure the thermal conductivity of samples is described below.

The sample is a bar set up as shown in figure 5.2. Copper clamps are used to affix it to the base plate, and to mount temperature sensors at the required points. The sensors used are Cernox™ thin film resistance temperature sensors. These sensors are compact in size, easy to mount and demonstrate excellent heat transfer resulting in a fast response time. My experiments have shown that they are very stable over repeated thermal cycling, making them ideal for this specific application. These qualities are of benefit because the sensors need to be accurately characterised and as stable as possible. The sensor wires are Phosphor-Bronze; a material of low thermal conductivity and high resistivity that serves to minimise heat loss through the wires. In order to reduce temperature reading errors, it is necessary to minimise heat loss and parasitic heat flow from room temperature to the sample by heat sinking all components of the apparatus. Apiezon grease is used between the copper clamps and sample, the sensors and copper clamps as well as between the base of the sample and the cold head. In addition, the wires are fixed around copper bobbins to anchor them thermally.

The apparatus is shown in figure 5.2 and is described as follows: the sample has copper clamps containing heaters at the top, followed by two central clamps and the base clamp holding the sample to the cold head. All four sets of clamps contain temperature sensors. The base sensor is used to ensure the lower end of the sample maintains a steady temperature. The calculation of thermal conductivity is carried out over the central section of the sample.

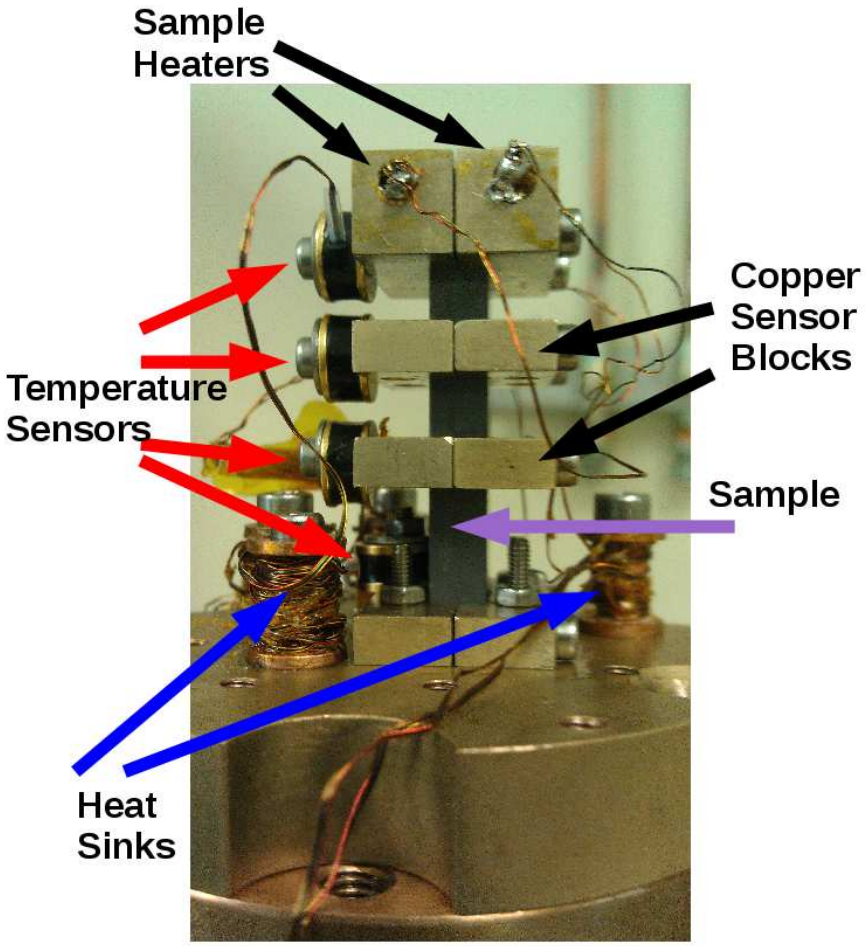

Figure 5.2: Experimental configuration for thermal conductivity measurements showing location of the sample with copper clamps, sensors, sample heater and copper heat sink bobbins.

5.2 Hardware

A number of hardware and software issues were encountered during the design and test phase of this experimental configuration. The following discussion will focus on the final configuration used for experimental measurements. More detailed configuration settings and further detail on issues encountered can be found in Appendix C.1.

A Gifford-McMahon cooling system was used, as shown in figure 5.3, comprising of a Helium compressor [121] (a) providing the high pressure helium gas to the test cryostat (b) through flexible stainless steel gas lines (c) with a Cosmotec chiller (d) [122] in place to chill the connections and lines to avoid overheating. Radiation shields (e),(g) enclose the sample (f), all enclosed in the vacuum shroud (h). When the cryostat is ready to run, an Oerlikon Rotary Pump [123] with a built in turbo pump is used to evacuate the sample space prior to cooling (i). The dual pump system can achieve pressures of up to 1×10^{-7} mbar, offering very good thermal insulation which is essential to achieve the target temperatures. The test cryostat base (j) is comprised of displacers, regenerators and the inlet/outlet valves which together perform the gas expansion (see section 1.6.2). The base has electrical feed-throughs (k) for further support hardware.

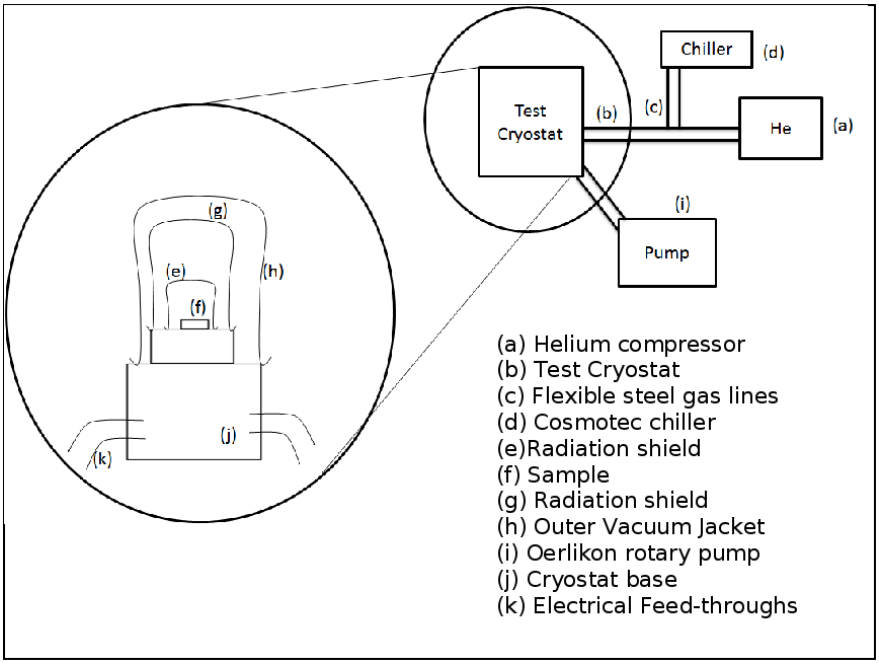

Figure 5.3: Setup of the Janis Cryostat and contributory hardware. The Helium compressor supplies the cooling power to the test cryostat where the sample is enclosed in radiation shields and a vacuum shroud.

The cryostat cold head offers a sample mount area, diameter 30 mm. The sample mount can be changed to allow different samples or setups to be fitted[1]. The sample and sensor wires attach to the electrical panel adjacent to the cold head on the cryostat central pole. The electrical panel consists of eight channels (marked Ch 0-Ch 7 on figure 5.4). This electrical panel is wired internally to a 32-pin feed-through on the cryostat base. Shielded cables connect these channels to the support hardware for controlling and monitoring the experiment. The control heater (T_c) is wired to a 10-pin feed-through alongside another sensor channel. A further 31-pin feed-through contains the power supply leads for the sample heater and finally a spare feed-through is available for any further use.

[1] A larger sample area of diameter 100 mm is also available alongside the relevant radiation shields and fittings. This larger setup was not used during the course of these studies.

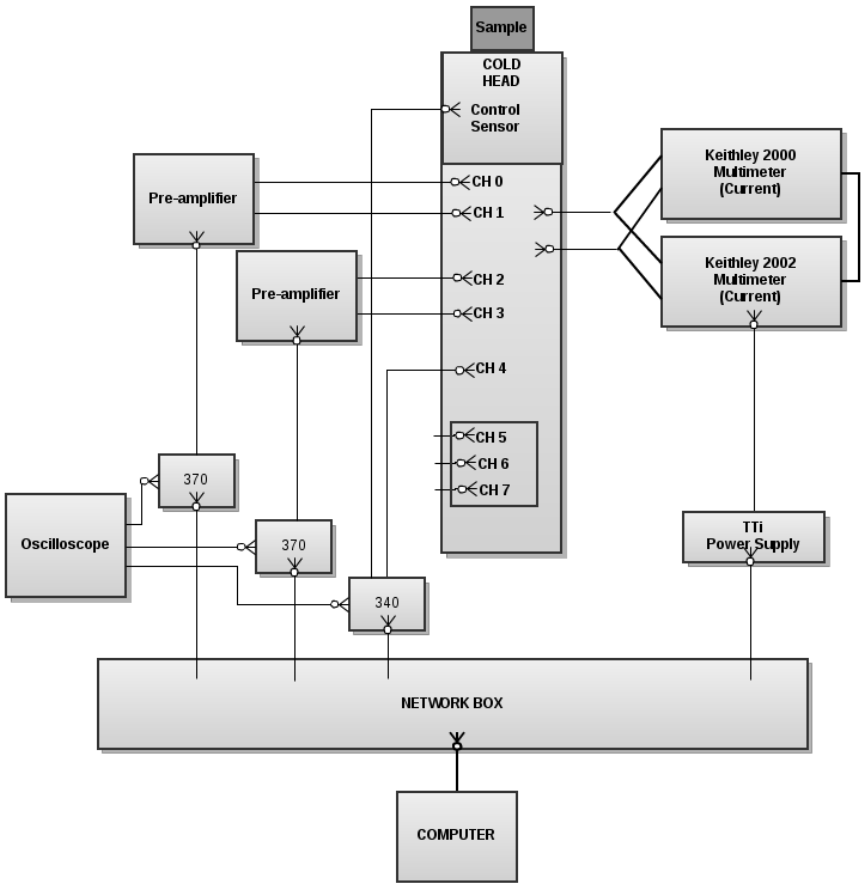

Figure 5.4: Setup of the control system for thermal conductivity measurements. The temperature is controlled by a Lakeshore 340 temperature controller while the Lakeshore 370 resistance bridges are used to monitor the temperature in different areas of the system. The TTi power supply is used alongside the Keithley devices to control the power fed to the sample heater.

The temperature of the system is controlled by a Lakeshore 340 Temperature Controller. This is connected to a control loop built into the base of the cold head, consisting of a temperature sensor and two heaters. When the user selects the desired temperature, this control loop adjusts the system until the temperature is stable. The temperature sensors are attached to Lakeshore 370 resistance bridges

which display their resistance and by using loaded temperature curves, they also display the sensor temperature assisting greatly when setting up the equipment and monitoring the experiment. This model of temperature controller is capable of reading up to 16 channels, but for the purpose of these experiments only 2 channels are used on each. Only one channel can be read out at a time on each Lakeshore 370 so efficiency is increased by implementing two devices reading out two channels each (as the only time lost is switching between monitoring two channels). Finally, the TTi power supply inputs power to the sample heater and a 4-wire measurement of power is taken across the sample heater using values read by the Keithley multimeters.

5.3 Temperature sensors

This section concerns the temperature sensors used in the test system and the calibration process for the sensors. The sensors used in the test system are Cernox™ thin film resistance sensors, with the chip mounted in a copper can. Insulated phosphor bronze wires and an epoxy strain relief are affixed to the temperature sensors to allow attachment to the resistance bridge for reading out resistance and hence temperature values. This copper can is screwed to the setup using an aluminium screw with Apiezon grease, creating a contact with the greatest possible surface area.

5.3.1 Calibration of sensors

Two sensors were acquired from Lakeshore, one calibrated in the range 300 mK – 325 K and the other in the range 4 K – 325 K with data for resistance and the corresponding temperature provided. Four un-calibrated sensors were also purchased; each had data for resistance values at 4 K, 77 K and room temper-

ature. The calibration method used by Lakeshore, in which they calibrate the sensors against a known standard, was repeated as closely as possible in the test cryostat. The sensors were mounted on a copper base plate using stainless steel screws alongside one of the calibrated sensors. A radiation shield was fitted over the sample area and the vacuum shroud used to close the system. Resistance measurements were recorded at temperature steps between 4 K and room temperature. Chebyshev polynomials were used to fit the data to give a full spectrum of results (Appendix A) which were then converted to temperature values using the calibrated sensor's temperature-resistance data.

Figure 5.5 shows the data collected for the calibrated and uncalibrated sensors. For the calibrated sensor it was possible to show the robustness of the sensor and setup as the same data values could be repeatedly collected (figure 5.4a). One of the problems faced with the uncalibrated sensor was the inability to reach the same base resistance value (figure 5.4b). This problem was resolved by applying a thin layer of Apiezon grease in between the sensor and the copper base plate to increase the contact surface area and therefore improve heat transfer. Once the setup had been improved, the experiment was repeated to consolidate the information, and the data used to calibrate the unknown sensors.

5.3.2 Systematic reliability of temperature sensors

The sensors have been repeatedly tested by Lakeshore Cryogenics with a quoted reproducibility accuracy of ±3 mK at 4.2 K. The combined uncertainty of the temperature measurement and the resistance measurement expressed as an equivalent temperature (as stated by Lakeshore for the calibrated sensors) from 1.4 K to 300 K are shown in table 5.3.2. The long and short term stability of the sensors were monitored before experimental work was carried out.

This uncertainty is based on a 95% confidence level of the Chebyshev polyno-

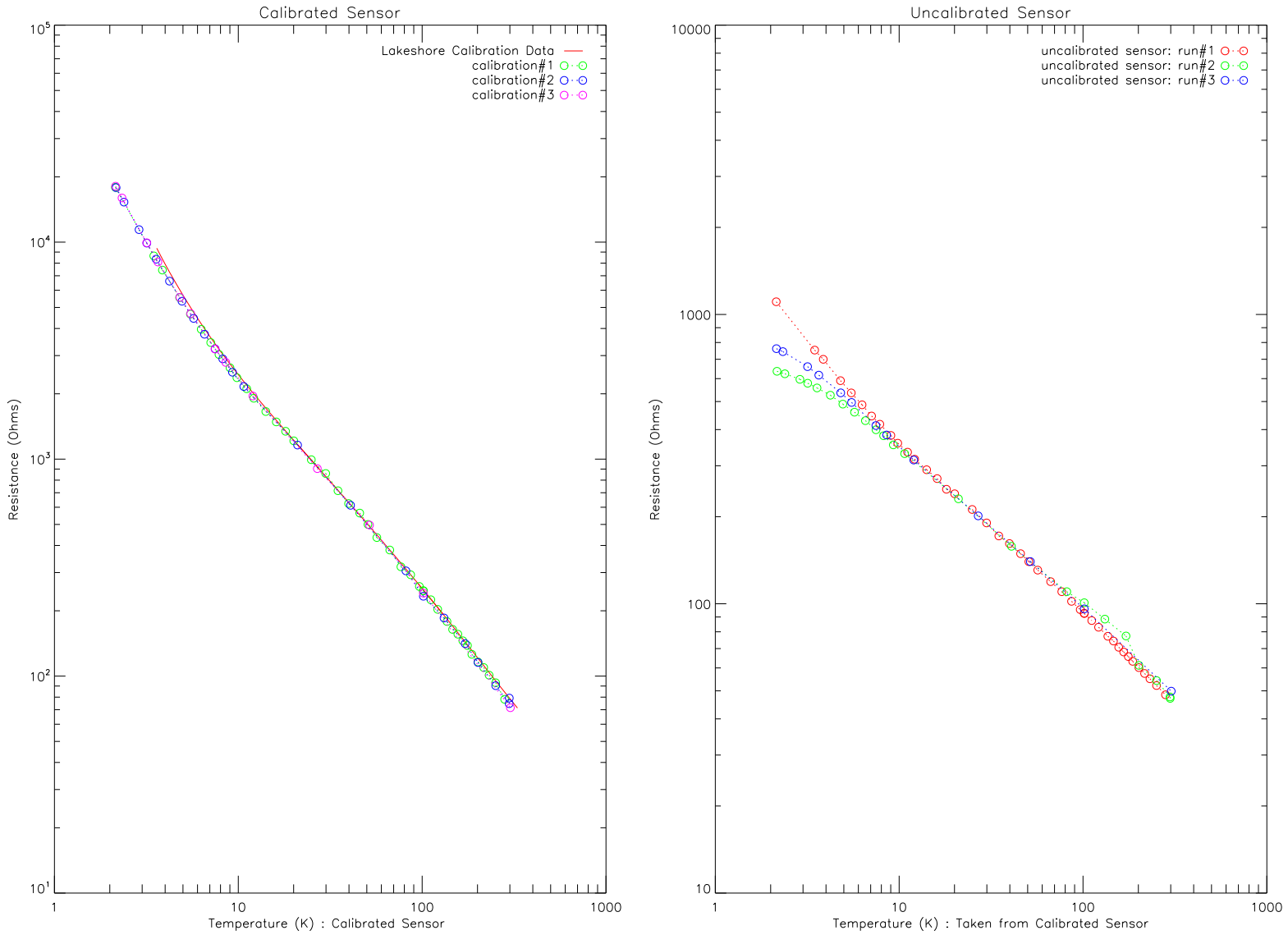

Figure 5.5: (a) Stability of calibrated sensor and repeatability of temperatures achieved and (b) uncalibrated sensor which did not return to the same base resistance on each cool down. The contact of the uncalibrated sensor was improved using Apiezon grease and a reproducible resistance was then achieved at low temperatures.

	Sensor Range: 0.3 mK – 325 K		**Sensor Range:** 4 K – 325 K	
Temperature (K)	(± mK)	Uncertainty (%)	(± mK)	Uncertainty (%)
1.4	4	0.29	4	0.29
4.2	4	0.1	4	0.1
10	5	0.05	4	0.04
20	9	0.045	8	0.04
30	11	0.036	9	0.03
50	16	0.032	12	0.024
100	24	0.024	16	0.016
300	72	0.024	40	0.013

mial fits obtained. The sensors calibrated in this work will have a slightly lower accuracy than those calibrated by Lakeshore Cryogenics. The overall error on temperature is discussed further in section 6.5.3.

5.4 Software

Complementary software was required to run the system and record results. This section describes the software system and briefly outlines the development of software in different computer packages.

The system and data collection were initially run manually. This allowed checks to be carried out on the consistency of data relative to the values measured prior to closing the cryostat (at room temperature only) and to ensure the equipment was operating as expected. As certain resistance readings were known for set temperatures, the system could be cycled through for the readout values to be confirmed. This also allowed the system to be monitored as the automated system software was developed. In initial tests, an AVS resistance bridge was used to manually capture data. The instabilities associated with this AVS bridge are shown in the next section. Prototype software was developed in Python [124] which enabled preset temperature and power set ups to be run.

The software was required to communicate between the Lakeshore devices and 6 temperature sensors in addition to the sample heater and control system. These were wired to three of the military pin points: one for the Lakeshore 340 temperature controllers, one for the heaters and one for the remaining four temperature sensors. After cooling the system down to the base temperature, the software was required to run through the process shown in figure 5.6 and listed below. Labview™ software was used as this was deemed to be the most appropriate and convenient computer interface to run the experiment [2].

[2]The Labview™ software used was initially designed and built by Dr. Adrian Glauser. It was incorporated and adapted to be used.

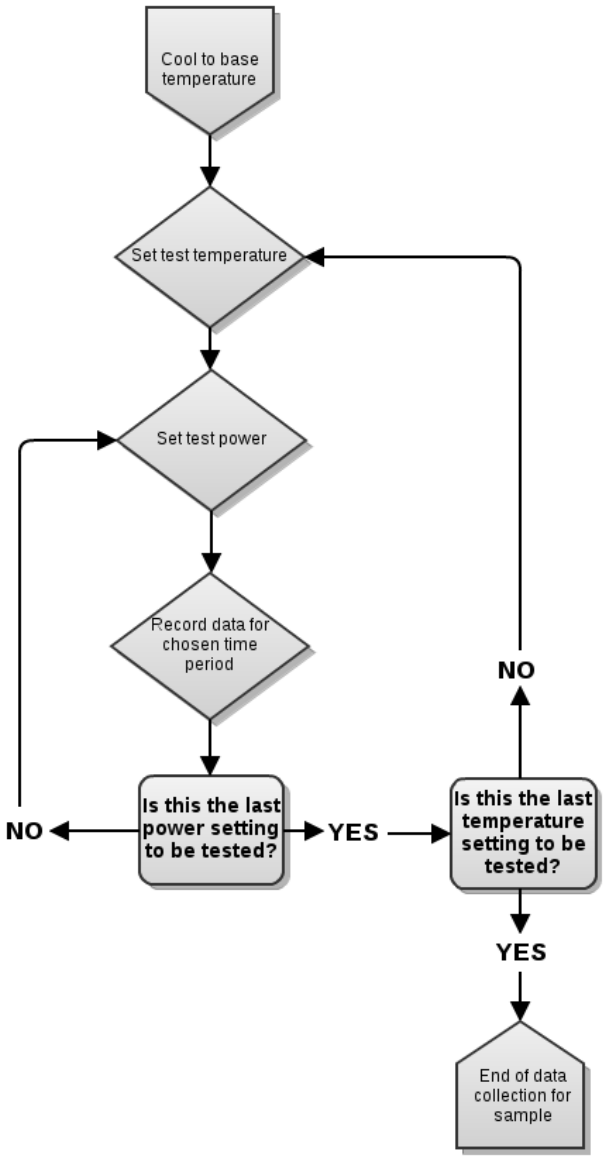

Figure 5.6: Data collection pipeline: the process the Labview program runs through to collect the experimental data.

After cooling the equipment to base temperature, the software runs through the following process:

1. Bring cryostat to required temperature and stabilise.

2. Record data for pre-set length of time with zero power to sample heater.
3. Increase power to sample heater, through all possible settings allowing each one to stabilise for pre-set length of time.
4. Increase temperature to the next defined temperature step and return to zero power to sample heater.
5. Run through temperature steps (recording data for each power to sample heater within this)
6. End of experiment

The Graphical User Interfaces (GUIs) in figure 5.7 show the software interface used for running and monitoring the experiment. The first panel shows the experimental output of the system- a plot of Time vs. Temperature and another of Time vs. Power. These offer the ability for the user to monitor the experiment as it is running so any obvious discrepancies can be identified. The side panel displays a numerical output of every temperature sensor in addition to the measured error between consecutive readings. The bottom panel allows the user to run the experiment using pre-loaded parameters and buttons to activate and deactivate the temperature controller and heaters. The user can also load settings for temperature setpoints and voltage setpoints, along with the time constants for refresh rate of screen and frequency of saving data (every 0.3 s).

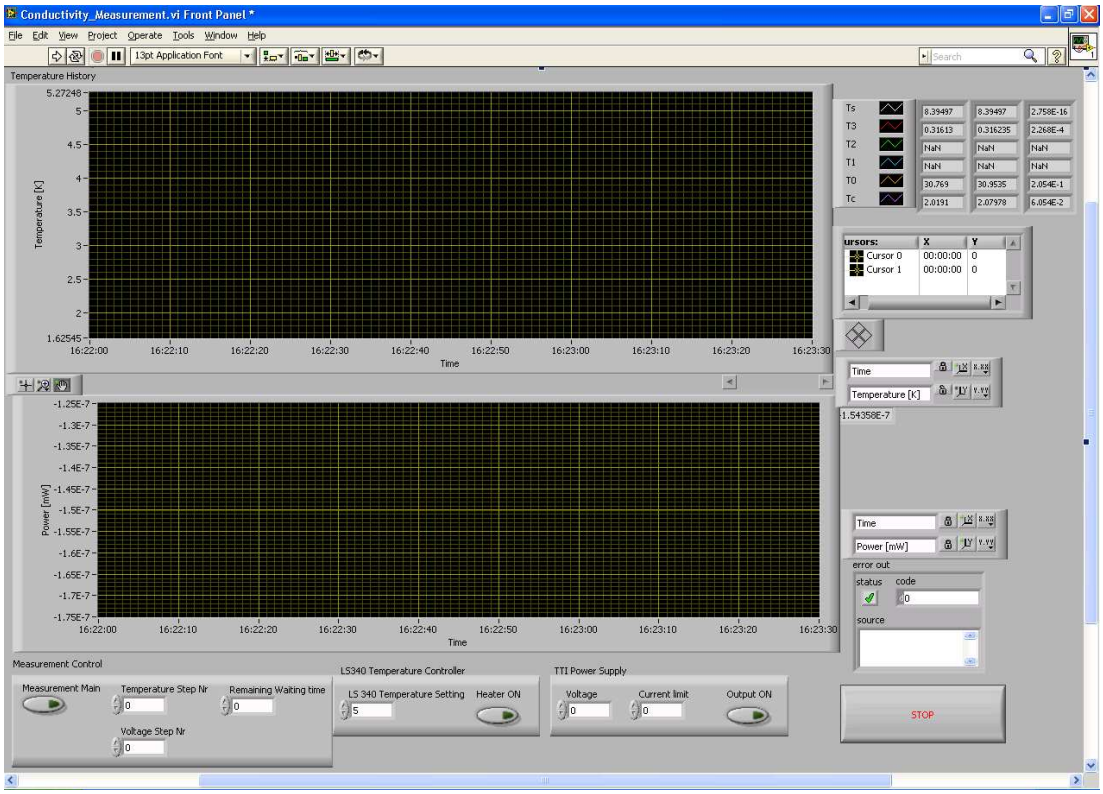

Figure 5.7: GUI for entering experimental parameters for monitoring and controlling of a running experiment. The top plot shows the temperature of each sensor relative to time and the bottom one shows the power of the sample heater.

5.5 Issues with equipment

The majority of issues in this case were associated with the prototype equipment set up rather than the final configuration. The following section describes the main problems encountered with the final experimental setup. Further detail is given in appendix C.

5.5.1 Thermal oscillations and temperature damping

Thermal analysis measurements rely heavily on accurate temperature readings. Ideally the temperature would be stable to reduce error in the temperature measurement. The system's temperature control was monitored and a number of investigations were made into reducing temperature fluctuations.

The original setup used an AVS Resistance Bridge [125] with a Labview™ program monitoring it. This resistance bridge was eventually removed from the cryostat system; this was due to its inability to remain steady. The stability was investigated in different temperature regions with an example of the instability during a cooldown seen in figure 5.8. Further details of the investigations with the AVS Resistance Bridge are included in Appendix C.1.1.

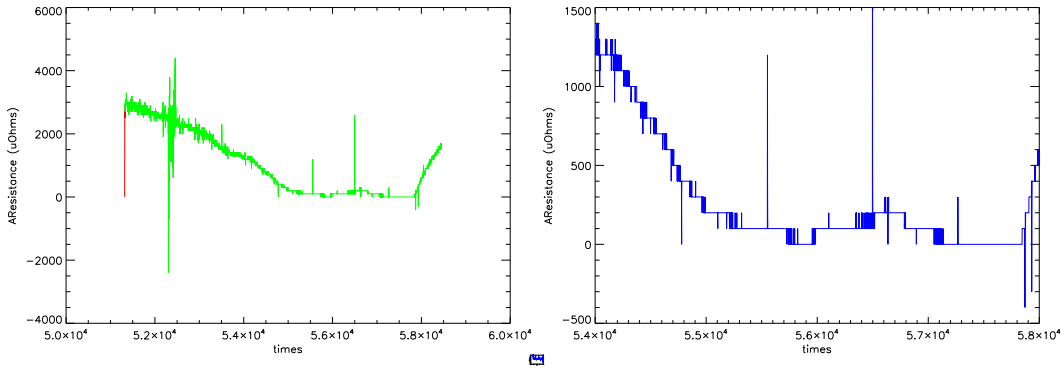

(a) **(b)**

Figure 5.8: Cooldown of system when monitoring using AVS resistance bridge. (a) Cool down from 295 K to 3 K and (b) zoomed in on the lower region. The 'lump' at times = 5.65×10^4s is where the temperature is raised from 8 K to 30 K and lowered again. This AVS resistance bridge was replaced with a Lakeshore 370 resistance bridge due to this instability in temperature.

The modified system, which was used for the bulk of measurements is temperature

controlled by a built-in sensor alongside two built-in heaters, held in a copper clamp on the cold head (figure 5.9). This is connected to the Lakeshore 340 temperature controller and from here two options are available for heating: the temperature can be set and the heaters in a loop with the sensor will stabilise around that temperature using the PID Algorithms for accurate control (appendix C.2.2); or a specific percentage of available power can be chosen and applied constantly to the heater. The long and short term stability were monitored before experimental work was carried out.

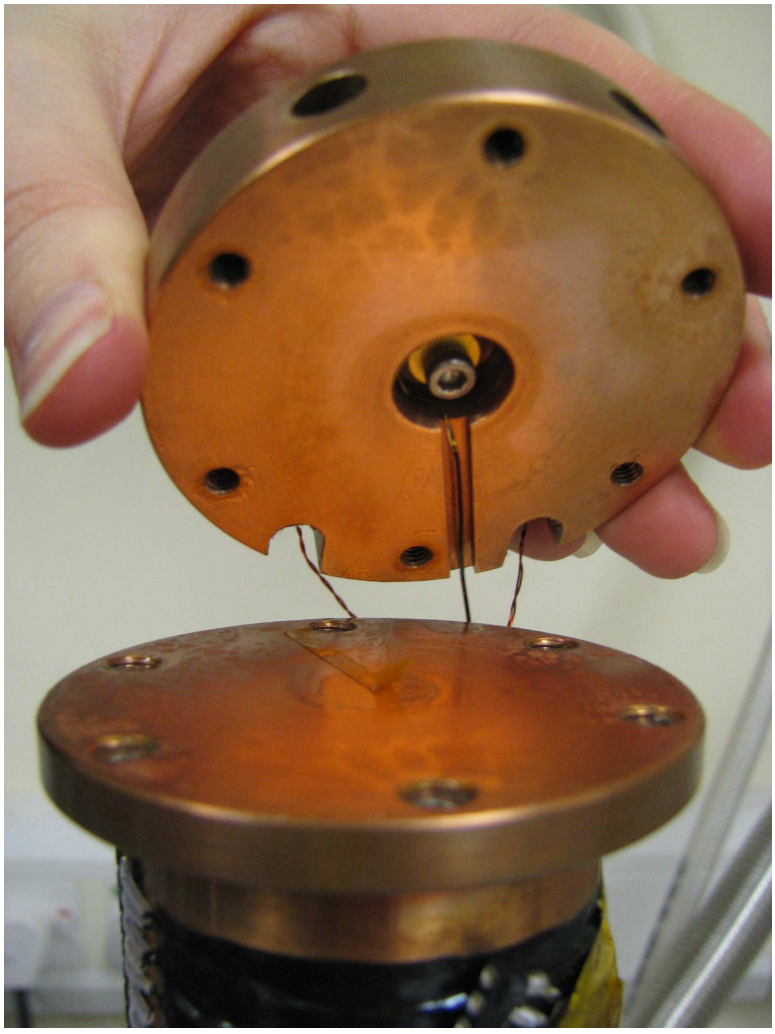

Figure 5.9: Built in temperature sensor (centre of copper block) and heaters (one either side built into the copper block, only the two holes they are fitted in are seen here).

Long term stability of system

When the Lakeshore 370 resistance bridges were first implemented into the system, long term stability was investigated by monitoring the temperature of the system using three sensors over a period of 64 hours. The system was held at a steady temperature of 4 K with a constant heater input of 25% with the results

shown in figure 5.10.

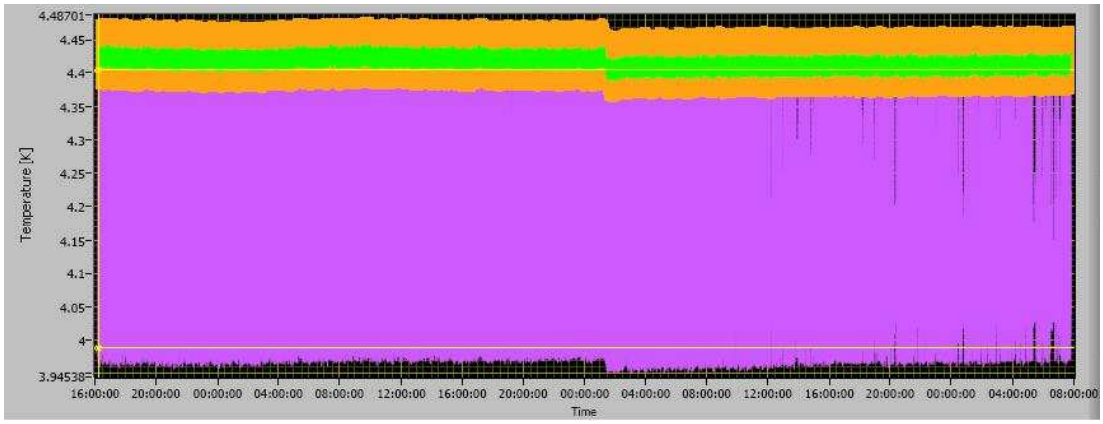

Figure 5.10: Stability of system as measured over a period of 64 hours. The purple is T_c (cold head), orange is T_0 (base of cryostat) and green is T_1 (on sample).

The control loop of the system remained stable within 500 mK for the duration of the experiment, with the lower end of the sample remaining stable within 110 mK and the sample sensor T_1 stable to 50 mK. It can be seen there was a drop in temperature near the middle of the measurement sequence; thought to be due to a dramatic change within the air conditioning system in the laboratory.

Short term stability of system

The short term stability was also investigated as it was required to be stable and temperature sensors reading out correct values before collecting sample data. The sensors' stabilities varied, with the built in sensor, T_c, having the greatest fluctuations in temperature. Figure 5.11 shows the stability of the cryostat system. The sensor data are also shown to be stable. However, Tc (shown in black) exhibits larger temperature fluctuations than T_0 (shown in red). At 3 K again T_0 is more stable than T_c, but there is an offset in temperature. This offset is in the order of

10 mK, 0.3%, and is accounted for in the analysis procedure as shown in section 6.2.

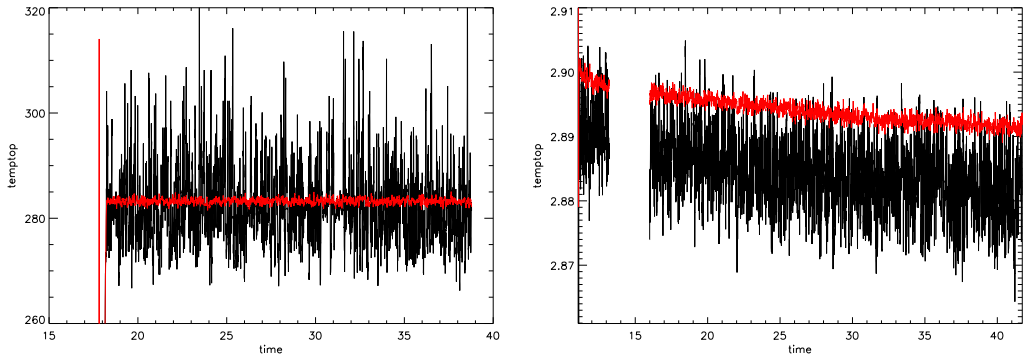

(a) **(b)**

Figure 5.11: Stability of the cryostat system at (a) room temperature and (b) 3 K. The control loop sensor T_c and sample base sensor T_0 are shown by the black and red lines respectively.

Fluctuations of up to 450mK exist at the temperature control loop, T_c, when held at the base temperature of 2.5 K which accounts for an 18% temperature fluctuation. This is damped slightly before reaching the sample base, T_0, but a fluctuation of 100 mK is still observed. The base of the sample needs to be kept at a constant temperature, as it has a relatively large influence on the system as a whole. This was investigated before continuing with measurements. These fluctuations were present due to the constant expansion and compression of gas occurring at the piston just below the positioning of the sensor and heaters. As the piston is part of the GM cooling process, this cannot be eliminated directly. The system above the cold head was examined and can be adapted to damp the fluctuations so the effect is not seen on the sample holder.

Initially the data filtering and averaging polynomials carried out directly by the Lakeshore temperature controller and resistance bridges were investigated

to find optimum settings for control and stability. The temperature controllers built in algorithms adjust the power directed to the built in heater to reduce the fluctuation, therefore stabilising at the desired temperature. The manufacturer states preferred settings for different temperature ranges [126], and these were found to be suitable for the system. Secondly the data filtering carried out by the Lakeshore devices was examined. The Lakeshore Resistance bridges are capable of filtering the data before the data file is written. An advantage of this is that fewer data points need to be collected, so that smaller data files are produced. In this case, filtering the data significantly affected the large instability in temperature, but this also removed the accuracy of the actual system temperature. For the remainder of the experimental work, no filtering was applied while collecting data. Detailed information of these tests are shown in appendix C.2.2

Thermal Modelling

Thermal models were produced to examine the effect of introducing a damping block between the cold head and the sample holder. The design of the cryostat offers two locations for this block to be included: between the cold head and the base of the control block where T_c is located, and between the control block and the sample holder. The aim is to keep the sample base at constant temperature, so it is logical to insert the damping block in the lower of these two locations. Consequently the fluctuations will have been damped before reaching the control block where the system is stabilised, hence the temperature control loop will be able to stabilise the system to greater precision.

The system was modelled by examining the temperature changes at points T_c and T_1 relative to the geometry and material of the damping block. A sinusodial wave function of temperature[3] was input to the model the temperature response

[3]The temperature fluctuations are not a perfect sine function, but for the purposes of this

over time, specifically investigating the size of temperature fluctuation and the stabilisation time.

The model was tested for Stainless Steels 310, 314, 314L and 316 as well as Brass UNS C26000. The stainless steels differ in exact content of Chromium, Molybdenum and Nitrogen and the 'L' denotes the low carbon version. These were modelled at temperatures of 4 K, 10 K, 20 K and 77 K. The resultant temperature fluctuations can be seen in figure 5.12 and also the stabilisation time in minutes for the sample to reach temperature equilibrium. Table 5.1 shows the results of temperature fluctuation and stabilisation time for Stainless Steel 316 (SS316) and Brass UNS C26000. These materials were identified as suitable materials to test as an experimental standard and would be used to test the experimental setup and robustness of the system. The highlighted boxes show the recommended material dimensions for implementation to the system for the optimum combination of length and diameter of damping block: a 0.01 m long block of stainless steel 316, radius 0.15 m. These materials were chosen as they are widely available and have confirmed known property data as shown in section 4.2.2.

5.6 Conclusions

This chapter described the setup of the hardware and software required for running thermal conductivity measurements on samples, based on analysis of a variety of systems (shown in chapter 3). The steady state heat flow method was found as the most suitable for the available cryostat, and a suitable system was constructed to hold the sample in a position offering the optimum heat sinking of both sample and wiring. The temperature sensors, calibrated by Cernox™,

modelling this function is sufficient to examine the relevance of material with regard to the temperature fluctuations.

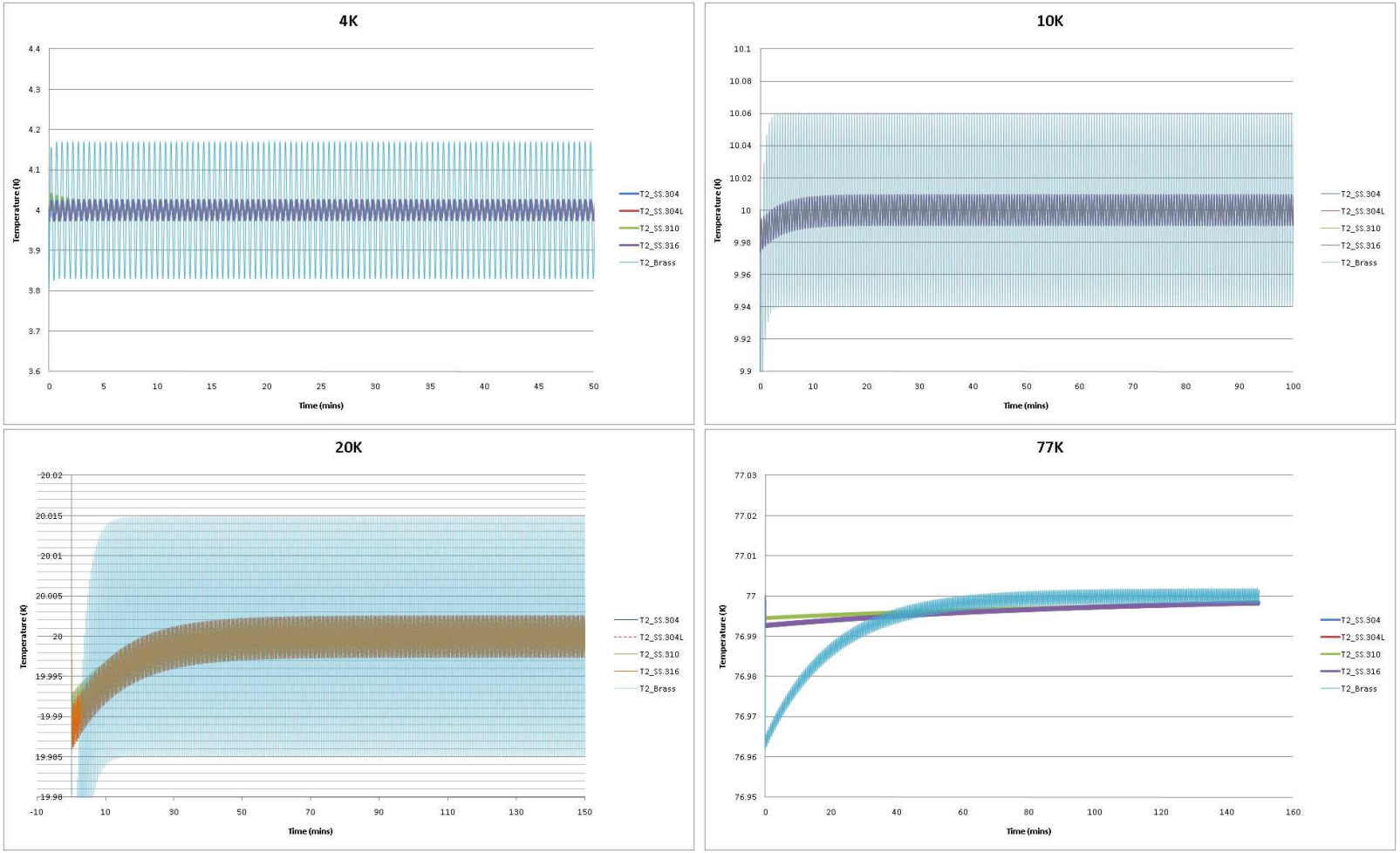

Figure 5.12: Modelled temperature fluctuations of sensors when damping block inserted in between the cold head and the control loop sensor, T_c, at 4 K, 10 K, 20 K and 77 K. A combination of reduced fluctuation alongside relatively low stabilisation time was required.

4K	Radius (m)	0.005		0.01		0.015		0.02	
Length (m)	Material / Function	S.S.	Brass	S.S.	Brass	S.S.	Brass	S.S.	Brass
0.02	Stabilisation (min)	<40	10	20	10	15	10	10	5
	Amplitude (K)	0.0029	0.02	0.0111	0.08	0.02	0.18	0.05	0.3
0.01	Stabilisation (min)	time too		10	5	10	3	10	5
	Amplitude (K)	long		0.02	0.16	0.095	0.33	0.09	0.53
0.005	Stabilisation (min)	time too		5	3	5	3	10	5
	Amplitude (K)	long		0.04	0.3	0.1	0.06	0.18	0.78

10 K	Radius (m)	0.005		0.01		0.015		0.02	
Length (m)	Material / Function	S.S.	Brass	S.S.	Brass	S.S.	Brass	S.S.	Brass
0.02	Stabilisation (min)	300	80	60	20	50	10	20	10
	Amplitude (K)	0.001	0.2266	0.0042	0.027	0.009	0.06	0.016	0.104
0.01	Stabilisation (min)	time too		30	10	15	5	15	10
	Amplitude (K)	long		0.02	0.05	0.035	0.12	0.04	0.22
0.005	Stabilisation (min)	time too		15	5	10	5	5	3
	Amplitude (K)	long		0.011	0.104	0.04	0.24	0.055	0.4

20 K	Radius (m)	0.005		0.01		0.015		0.02	
Length (m)	Material / Function	S.S.	Brass	S.S.	Brass	S.S.	Brass	S.S.	Brass
0.02	Stabilisation (min)	>300	250	>250	60	150	40	100	30
	Amplitude (K)	0.0003	0.0016	0.0011	0.0066	0.002	0.0147	0.005	0.026
0.01	Stabilisation (min)	time too		100	30	60	20	50	20
	Amplitude (K)	long		0.0025	0.014	0.005	0.03	0.01	0.0527
0.005	Stabilisation (min)	time too		110	15	50	10	40	5
	Amplitude (K)	long		0.0045	0.026	0.01	0.06	0.02	0.104

Table 5.2: Thermal stability and temperature fluctuations for Stainless Steel 316 and Brass damping blocks when inserted between the cold head and control sensor, T_c.

were further calibrated and implemented for the thermal conductivity measurements. The hardware system was designed to allow continuous measurements of the sample, with the support software developed alongside.

The stability of the full system was investigated as fluctuations were apparent in the measured data. The initial change from using an AVS resistance bridge to a Lakeshore 370 resistance bridge increased the time response of the system and decreased the error in temperature fluctuations. Optimum settings for control and stability of the system were chosen and implemented using the Lakeshore devices. Finally, thermal modelling of the temperature responses were completed for future adaptations to the system. The following chapter shows the analysis methods and software implemented for the steady state thermal conductivity measurements.

Chapter 6

Analysis and calibration techniques

The research carried out on other authors' work, presented in chapter 3, contributed to designing an experimental configuration and analysis method for the test cryostat. This chapter presents a simplified system and detailed explanation of the analysis method used for the experiments contained within this thesis. The results shown are those of the experimental standard Stainless Steel 316.

6.1 Analysis method

For the purpose of the analysis the simplified system of a length of sample, L with a sensor clamp, c, at each end is used as shown in figure 6.1. A heater is built in to the top copper clamps at T_3 which will be used to change the heat flux across the sample. The base sensor, T_0 will be kept at a constant temperature using the cryostat temperature control loop, T_c. This setup allows us to compare two separate experiments with different sample lengths, meaning the end effects of the copper clamps on the conductivity of the sample can be eliminated. A

heater is built in to the top clamps in the experimental setup, and a variety of powers can be applied to create a temperature gradient in the sample. The sample is said to be in steady state once $P_{in} = P_{out}$. This will be achieved and monitored for various electrical heater powers, P, and base temperatures, T_0. At each measurement point this creates a temperature difference over a length, L, of $\Delta T = T_2 - T_1$ for cross sectional area, A.

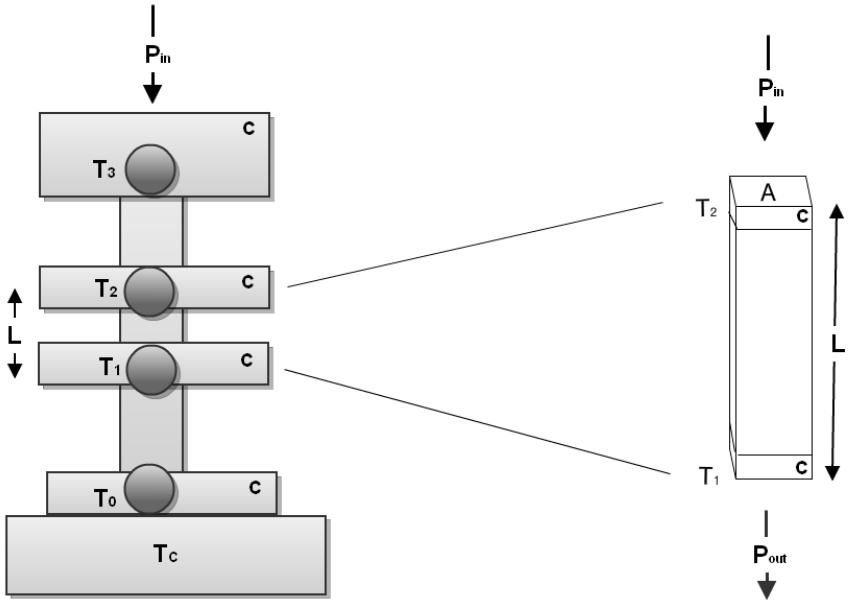

Figure 6.1: The sample setup has been simplified for analysis purposes:- the section for analysis consists of the length of sample, L and two copper clamps, c. Power, P is applied to a heater in the top copper clamps at T_3 and the base, T_0, is kept at a constant temperature using the cryostat temperature control system, T_c.

Labview™ was used to automate this process for chosen values of base temperature and heater power. The output results from this are shown in figure 6.2 where the large steps of T_0 are the changes in base temperature, and within each of these large steps 5 smaller steps can be seen; these steps are the resultant increase in temperature due to applying electrical power to the sample heater.

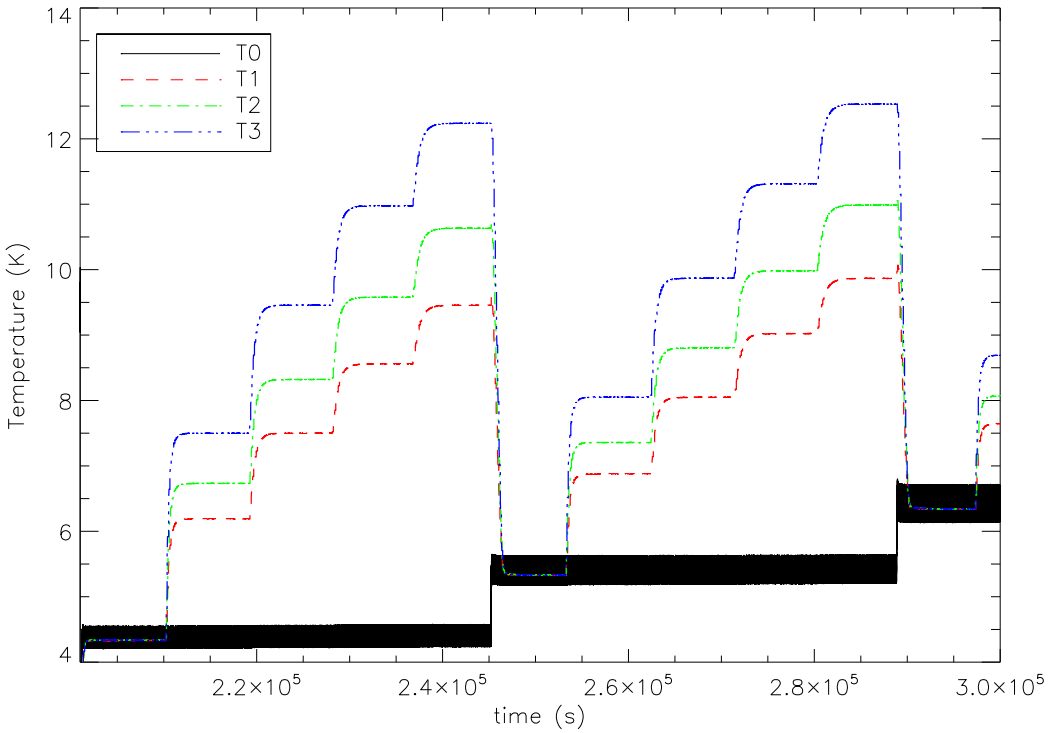

Figure 6.2: Data as collected by the Labview™ software [127]. The large steps in T_0 show the changes in base temperature and the smaller steps within this relate to changes in applied heat through the sample heater at the top of the experimental configuration. Constant T_0 shows stability in the system.

A measurement was recorded every 0.3 s with each temperature step recorded for 3600 seconds. The data recorded contained values for the resistance and equivalent temperature of every sensor as well as the applied heater power and a time stamp. These data were processed to analyse the heat flow at every power step within each temperature setting. Through experimental investigation it was determined that recording data for this length of time would allow the system to stabilise and a large number of data points would remain which could be used for statistical analysis of the system. Temperature oscillations were still visible

in the system, most dominantly in sensor T_0 as seen by the broad black line in figure 6.3. Section 5.5.1 details methods investigated to reduce these thermal fluctuations. This time window allows the data remaining after stabilisation to be sufficient to reduce the error on the statistical analysis carried out.

Binning data:

The data were binned in base temperature and in applied heater power so each step could be analysed separately, giving a direct analysis of the effect of increasing heater power on the temperature of the sample and therefore the thermal conductivity of the sample to be determined. It was apparent that at the edge of each bin there was a time frame for the stabilisation to allow the sample to return to its steady state after the change in conditions. This transient overshoot was present for a change in base temperature, figure 6.3, and a stabilisation time also occurs on change of heater power, figure 6.4.

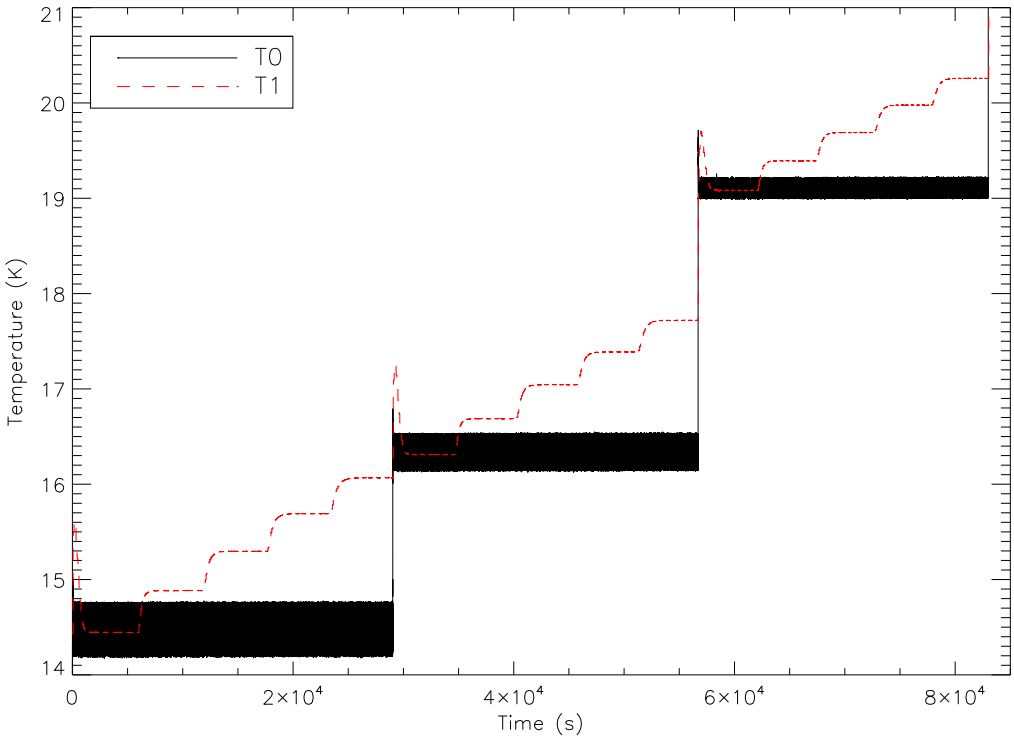

Figure 6.3: It can be seen that when the temperature of the cold head, T_0, is changed the temperature of the sensor overshoots the desired temperature. This is accounted for in the analysis process as described in the text. The individual increases in temperature of sensor T_1 seen within each increase in T_0 are due to increase in power to the sample heater.

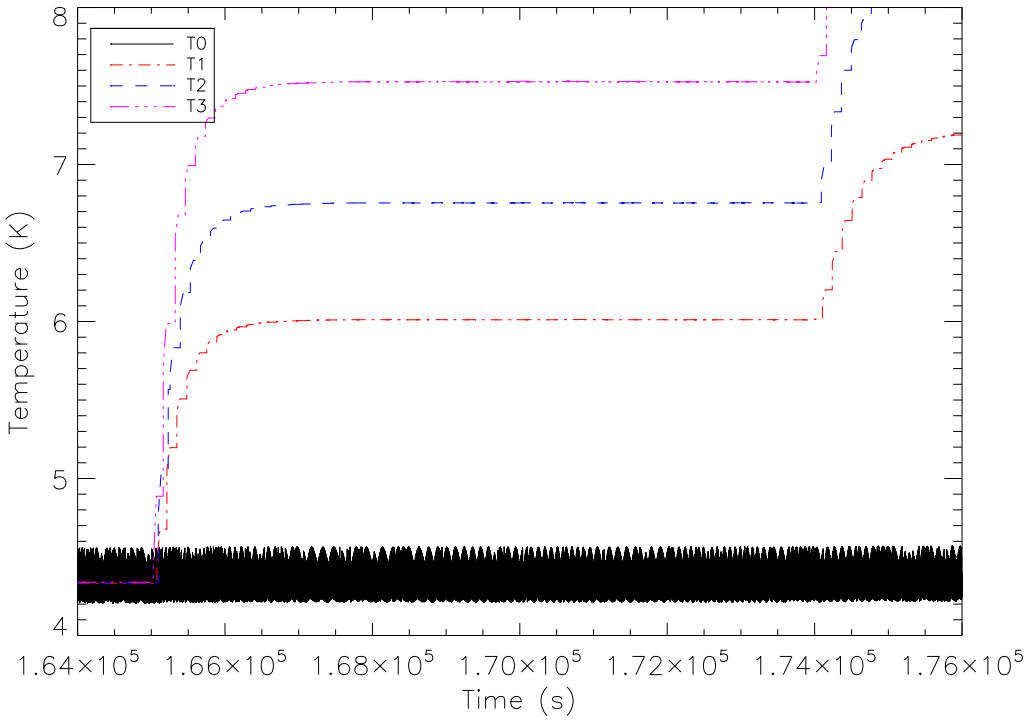

Figure 6.4: An allowance is required for the temperature to stabilise. This is accounted for in the analysis process as described in the text. The increase in temperature of the sensors at time $1.74 \times 10^5 s$ is where the power to the sample heater has been increased as the end of the time constant for measurement has been reached.

To account for the overshoot in temperature and the overall stabilisation time required when changing temperature or heater power, a significant proportion of the dataset had to be eliminated. Each bin contains approximately 9000 data points, and together the overshoot and stabilisation periods comprise 40% of these data. To ensure all steps had stabilised and to allow for any bin where there may be an abnormality in stabilisation time, the first 60% of each bin was discarded. The remaining 3600 data points represented a 20 minute time period and this was sufficient for analysis.

6.2 Temperature stability

Further to the regular temperature oscillations in the system which are reviewed in section 5.5.1 and can be clearly seen in figure 6.5 (a), the overall stability of the system over a long time period had to be monitored. The temperature of each sensor had to be determined so an accurate temperature difference can be determined for each temperature step. Although a stable temperature could be achieved on the three sample sensors (T_1, T_2 and T_3) of ± 1.5 mK, there was an offset between them at zero power, illustrated in figure 6.5 (b). In correcting this temperature offset for zero power (to make all sensors the same temperature as the base) this reduces their temperature slightly for the higher temperature steps. This normalisation removes the effects of calibration errors.

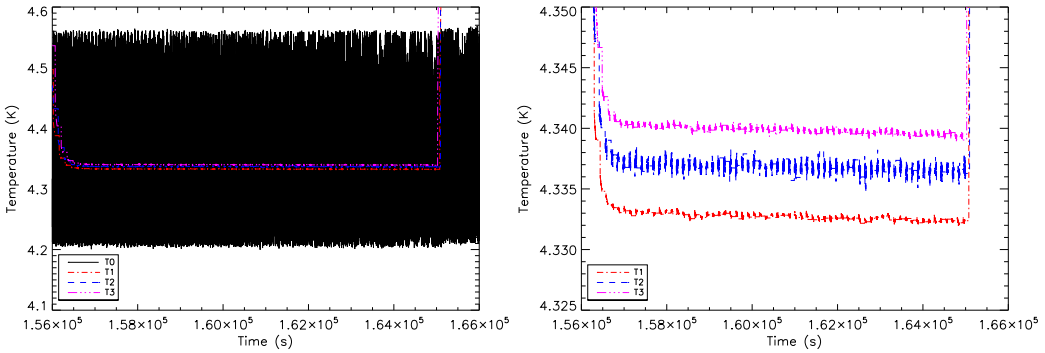

(a) Temp offset of base heater, T_0

(b) Temp offset of sample sensors, T_1, T_2, T_3

Figure 6.5: Temperature oscillations when power is applied to the sample heater: with (a) T_0 has the largest fluctuation (see section 5.5.1) and (b) it can be seen that there is a temperature offset between the different sensors when no power is applied to the sample heater.

After the temperatures had been normalised the actual temperature of the measurement ($\bar{T}$) and the temperature difference between the sensors (ΔT) were

calculated using:

$$\bar{T} = \frac{(T_1 + T_2)}{2}, \qquad \Delta T = \overline{(T_2 - T_1)} \tag{6.1}$$

where T_1 and T_2 represent the two sensors being examined. To reduce error in this calculation the temperature difference was taken at every recorded point, and then the median of the resultant temperature difference taken. This aims to reduce the error in the median temperature as any instabilities in the system would be evident in all sensors. Alternatively, the temperature could have been analysed using:

$$\bar{T} = \frac{\bar{T_1} + \bar{T_2}}{2} \qquad \Delta T = \left(\bar{T_2} - \bar{T_1}\right) \tag{6.2}$$

however this increases the error in measurement as the resultant temperature may be raised or lowered due to lengthened settling time, furthermore random fluctuations which occur in both sensors would also have an effect.

6.2.1 Power measurement

The input power to the sample heater is controlled by the Labview program, and a separate 4-wire measurement is carried out of the actual power over the resistor heater and the Keithley devices. This is combined with calculations of the parasitic heat conduction and electrical heat dissipation to calculate the total power input to the sample heater. The electrical heat dissipation through the wires is below 3×10^{-7}W. The parasitic heat conduction is the heat conducted by the wires from the hot end to the cold end. Both ends of sensor and heater wires need to be efficiently heat sunk to ensure any excess heat in the system can be drained out. The median power of the power measured across the heater was

taken and the other contributing power factors were included. The power factor used for the analysis procedure is as follows:

$$\text{Total Power} = P_{\text{Heater}} + P_{\text{parasitic conductance}} + P_{\text{heat dissipation}} \tag{6.3}$$

$$= P_{\text{resistor}} + \frac{A}{L}\left(\lambda_{\text{hot}} - \lambda_{\text{cold}}\right) \cdot \Delta T + P_{\text{wires}} \tag{6.4}$$

6.2.2 Length measurement

The accuracy of length measurement is of paramount importance in thermal conductivity calculations, especially when dealing with samples this small, as even a small error can have a significant effect on the final result. The following investigations were carried out, with a view to normalising the length between sensors.

The sensors were placed on the copper clamps as shown in figure 5.2. It can be seen that the length can be taken in two different ways as shown in figure 6.6: the length between clamps (Y1) or the length from the centre of each temperature sensor (Y2). Here measurement Y2 is used as this is a more accurate description of the effective length being measured, although the copper clamps create an additional channel of conductivity.

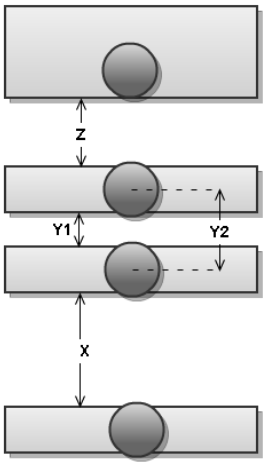

Figure 6.6: Positioning of sensors on the thermal conductivity apparatus. Distances X, Y and Z were varied during the testing phase to correctly determine the thermal conductivity of the sample. The central section being tested can be described as either the length between clamps, Y1, or the length from the centre of each sensor, Y2.

6.3 Testing a standard

This section will introduce the measurements carried out on an experimental standard specimen: stainless steel 316. The method of removing the end effects of the copper clamps is also shown.

6.4 Differential thermal conductivity calculation and example results

To calculate the total conductivity of the sample, the following equation is used:

$$\lambda = \frac{P \cdot L}{\Delta T \cdot A} \tag{6.5}$$

The derivation of temperature and power from the data and the cross sectional area is a standard measured length, as has already been discussed. The effective length of a sample can be calculated by comparing the conductivity of two differing lengths of sample as shown in figures 6.7 and 6.8:

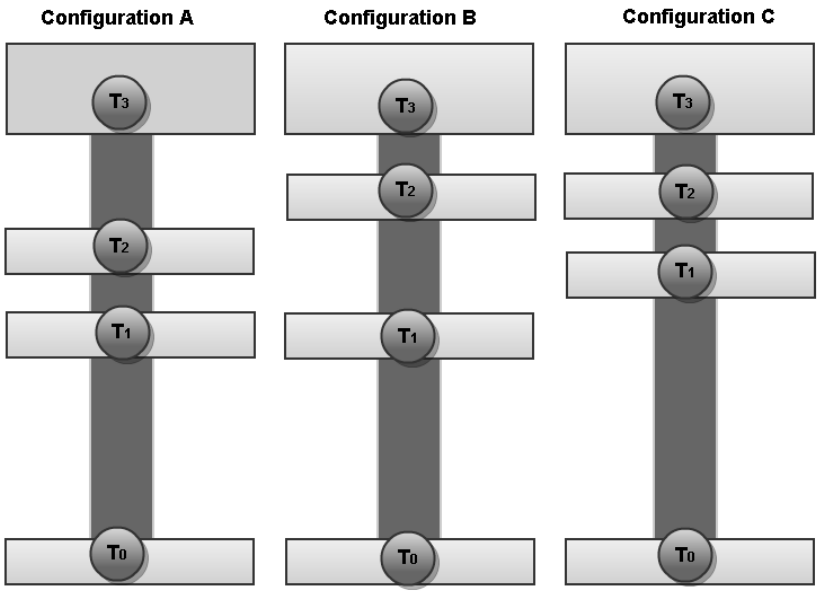

Figure 6.7: Three configurations for completing differential length measurements. The length $T_2 - T_1$ is changed so a comparison of the two experimental setups can be calculated to remove the end effects of the copper clamps.

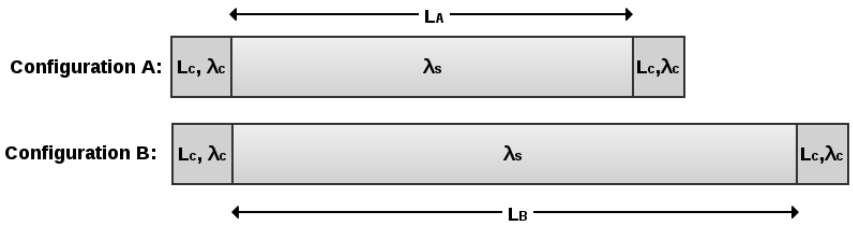

Figure 6.8: Configurations A and B as used for the differential analysis for calculating thermal conductivity. The copper clamps cause unknown end corrections that are taken to be the same in each case.

Both samples have end effects introduced by the presence of the copper clamps. In the two experiments the same clamps are used, but the quantity of Apiezon grease used may vary as might the torque applied to the screws, thus in both cases changing the contact area. The influence of the clamps was tested in the different experimental configurations (figure 6.7), with the result of thermal conductivity for configurations B and C illustrated in figure 6.9:

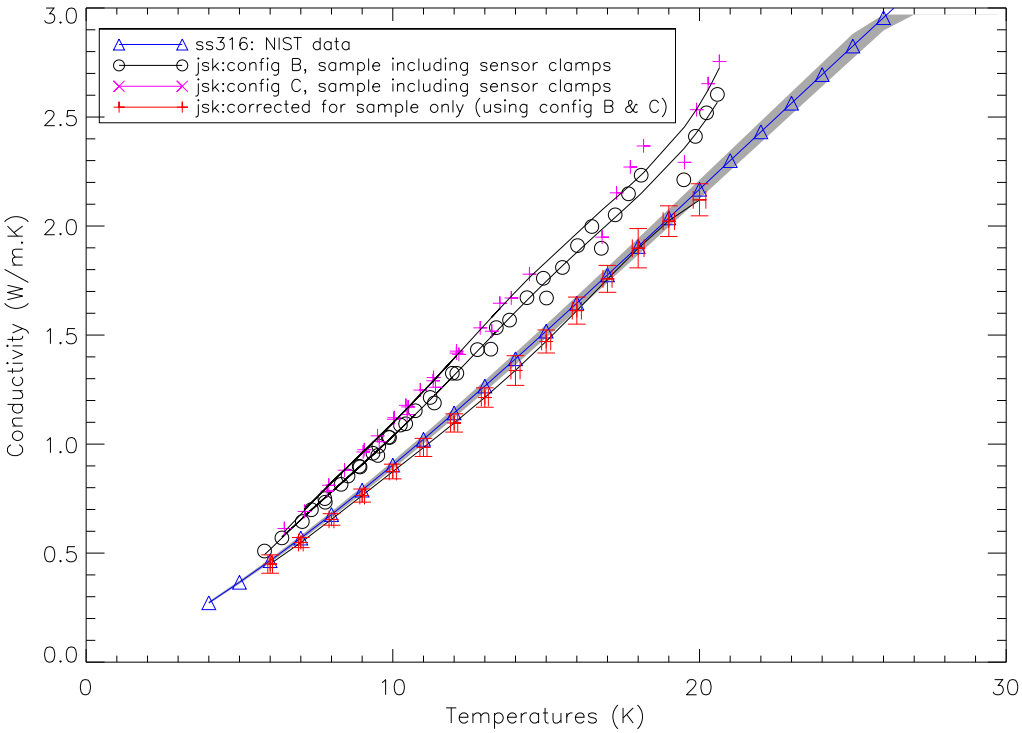

Figure 6.9: The effect of the copper clamps on the system can be seen by the deviation of thermal conductivity away from the expected result from NIST [91].

After removing the end effects caused by the copper clamps by using the differential method, the thermal conductivity of the sample can be estimated by applying:

$$\lambda_{sample} = \frac{L_B - L_A}{A \cdot [(\frac{\Delta T}{P})_B - (\frac{\Delta T}{P})_A]} \tag{6.6}$$

assuming that it is independent of temperature. The full general derivation for the thermal conductivity of a sample using this differential method is available in appendix B.

6.4.1 Example results: Stainless Steel 316

This section presents results for the Stainless Steel 316 standard tested as described using the differential method. Configurations A, B and C were measured with length $T_2 - T_1$ of 7.3045 mm, 9.0707 mm and 7.0861 mm respectively. The differential method used to calculate the conductivity of two combinations of lengths; B-A and B-C. The resultant conductivity was higher than the expected conductivity for each sample, without taking into consideration the end effects of the copper clamps, figure 6.9.

A differential length was calculated to remove the end effect created by the copper clamps. The initial results, figure 6.10, showed that differential measurement B-C was in agreement with NIST [91] to 4.2 %, whereas there was a discrepancy of 20 % between NIST values and measurement B-A.

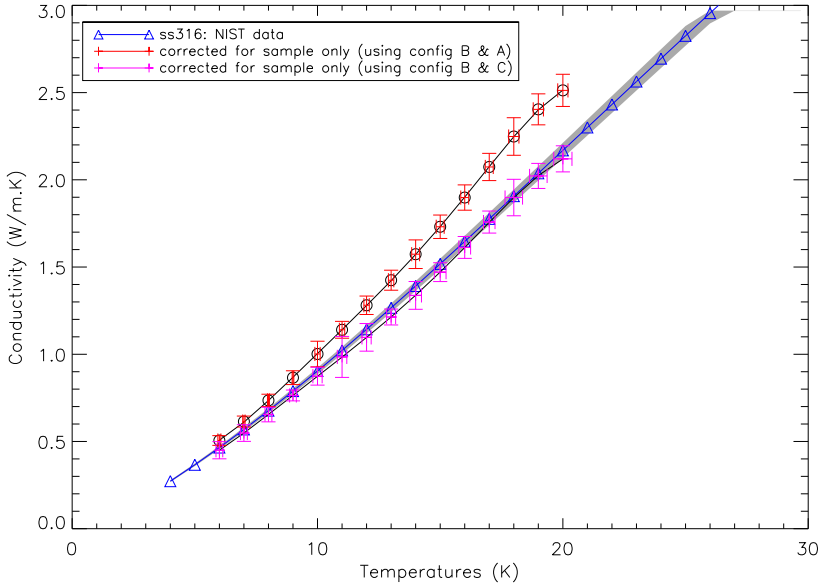

Figure 6.10: Result of thermal conductivity of stainless steel 316 as measured using the differential method. Three configurations were measured so two combinations of lengths could be used to test the robustness of the experimental setup. A discrepancy in the measurement when using configurations A and B can be clearly seen.

Configuration A was the first measured in the final setup. The manual setting up of the experiment had been practised multiple times by this point. The analysis code was examined for error which could occur in the data reduction for one of the data sets. No errors or problems were found in the analysis software which could have an effect on only one data set, so the values relevant to each data set were individually checked. Values used for length of sample sections were then cross referenced with the values noted in the lab book to check for inconsistencies. It was found that an error had been made when taking the length values from the lab book to the analysis program. Although the mistake only introduced a 0.16mm difference in the length of $T_2 - T_1$, this gave an associated error of 11 % at 6 K increasing to 20 % at 20 K.

This 2.27% increase in length [1] clearly demonstrates the importance of accurate distance measurement between the sensors. The final result of both differential measurements is shown in figure 6.11 to show the robustness of the system and the capability to make repeat measurements within a margin of 5 %.

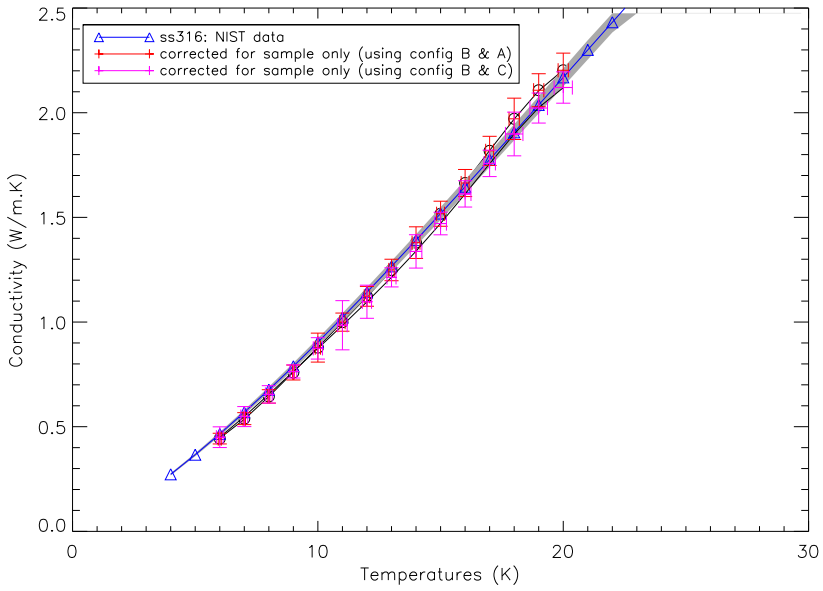

Figure 6.11: Initial results of thermal conductivity of stainless steel 316 as measured using the differential method. Three configurations were measured so two combinations of lengths could be used to test the repeatability of the experimental setup.

As shown with this instance, even an error of less than 2.5 % in length can have a dramatic effect on the results. Templates were manufactured to assist setup of the copper clamps for each of the three configurations to ensure error both in the positioning of the clamps is reduced, and also to ensure the clamps are parallel to one another. This meant that in all later experiments this distance was known to a sufficient accuracy, using a well defined procedure for measurement and checking

[1] This 2.27% increase in the increased length of the distance between sensors T2 and T1 in configuration A.

results.

6.5 Errors in system

Having discussed the measurement process, the errors in the system need to be accounted for. In a system of this complexity, there are a large number of devices which create unwanted errors to the final result of the thermal conductivity measurement. Here these errors are discussed and results for stainless steel 316 with associated errors shown are presented, as calculated using:

$$\sigma_\lambda = \left(\sqrt{3\left(\frac{\sigma_{\text{length}}}{\text{length}}\right)^2 + \left(\frac{\sigma_{\text{power}}}{\text{power}}\right)^2 + \left(\frac{\sigma_{\Delta T}}{\Delta T}\right)^2} \right) \cdot \lambda + \text{systematic errors} \quad (6.7)$$

6.5.1 Hardware errors

The errors due to hardware devices are summarised in table 6.1. Although some of the hardware errors would be negligible, the combined error is significant hence will be used in calculating the total error in the system. The combined error in the system due to hardware devices is 0.163 %.

6.5.2 Heat transfer model

Although power to the sample heater is measured using a 4-wire measurement, heat can enter and leave the system via other routes. The sample needs to be carefully set up with efficient heat sinking to ensure heat does not leak from the laboratory at room temperature into the sample area. The adverse effect this can have was shown during the manufacture of ISOCAM [35], as mentioned in section 1.4. Furthermore, radiation shields need to be in place to intercept any

Device	Setting	Range	Origin of Error	Error	% error
TTi	V	30 V		0.032 V	0.107
	V	15 V	0.1% ± 2 mV	0.017 V	0.013
	V	2 V		0.004 V	0.2
	I	0.001	0.3% ± 20 mA	20.003×10^{-3} A	0.3
		200 V range	± [(ppm reading ×	0.122 V	0.061
Keithley		20 V range	measured value + (ppm)	0.0188 V	0.094
2002	V	2 V range	range × range used)]	0.00224 V	0.112
Keithley	I	Range: 10mA	as Keithley 2002	8.105×10^{-5} A	8.1
2000		Reading: 1μ A			
Lakeshore		200 ohm, 2 mV, 8 nW		From	0.03
370	R	2 k, 2 mV, 80 pW		table in	0.03
		20 k , 2 mV, 800 fW		manual	0.05
Lakeshore	T	Heater Noise	50μV +1% output V		
340					
Sensors	T=4 K		± 0.2 mK at 4 K	0.005	0.005
				TOTAL:	0.163

Table 6.1: Hardware errors as detailed by instrument manufacturers. The settings of the devices were as follows: (V) Voltage, (I) Current, (R) Resistance, (T) Temperature.

incoming radiation. The heat transfers in the system are now discussed and a profile presented for the system to account for any further heat sources.

Heat sinking

When wires are used in a cryogenic system, they are both an electrical connection and a thermal connection. Heat sinking the wires to a part of the instrument at the correct temperature is of utmost importance to reduce heat dissipation effects. In this system, heat sinking has been done by two different methods: the wires at the second stage have been wound around the cryostat central post and secured

with kapton tape. At the lower temperature end of the cold head, copper bobbins have been used to maintain the wires at the temperature of the cold head. The bobbins are first covered with cigarette paper held on by General Electrical (GE) varnish (creating a boundary to avoid electrical shorting) and more GE varnish is used to hold the wires in place (illustrated in figure 5.2). As a varnish it can easily be removed using ethanol if required. The wire is then wound round the bobbin with the required length of wire anchored depending on the gauge and material of the wire [128]. Here 35 AWG Phosphor Bronze wires were used with a minimum length of 7 mm required for anchoring: something which was easy to achieve. A length of approximately 200 mm was anchored, with a short amount between the bobbin and sensor. The remaining wire should not be taut as this would cause scope for the wires to snap and put stress on the connection with the sensor/heater.

Heat can be conducted through these wires from room temperature to the cold head so efficient heat sinking is vitally important. The heat flow to the cold head was reduced by making some very minor modifications: lengthening wires, using wire with a smaller cross section, using wire with low thermal conductivity and heat sinking wires to a temperature as close to cold head temperature as possible. The electrical insulation on wires can be reduced to allow more efficient heat sinking. The insulation was not altered in the setup of this experiment, but wires with thin electrical insulation were chosen.

Radiation

Radiative transfer in the sample area of a cryostat can exist because there are many temperature differences within the system. Radiation shields need to be implemented between any hot and cold surfaces to intercept this heat flow. Copper and aluminium are commonly used materials for making these radiation shields.

The net exchange of heat between two surfaces can be calculated using:

$$P_{\text{radiation}} = A\varepsilon\sigma(T_{\text{hot}}^4 - T_{\text{cold}}^4) \tag{6.8}$$

where σ is the Stephan-Boltzmann constant, $5.67 \times 10^{-8}\text{W}/(\text{m}^2 \cdot \text{K}^4)$, A is the radiating surface area, here $A = 0.0005\text{m}^2$, and ε is the emissivity of the surface at temperature T:

$$\varepsilon = \frac{\varepsilon_1\varepsilon_2}{\varepsilon_1 + \varepsilon_2 - \varepsilon_1\varepsilon_2} \tag{6.9}$$

with $\varepsilon_{\text{ss316}} = 0.071$, $\varepsilon_{\text{Al shield}} = 0.039$, $\varepsilon_{\text{Cu}} = 0.02$.

The radiation effects calculated for this experimental setup are 5 nW at 4 K and 10nW at 9 K which corresponds to a maximum of 0.0004% of the power produced by the heater, hence is negligible.

Convection

Heat transfer by convection occurs due to particle collisions in air. As the cryostat is in vacuum at 2×10^{-7}mbar the heat transfer due to convection is negligible.

Heat conduction along wires

The parasitic heat conduction, Q, of a wire is the heat conducted along it from any warm part to the cold part, for example from the cold head to the sample. For a wire of cross sectional area A and length L this can be calculated using:

$$P(T) = \frac{A}{L}\int_{\text{cold}}^{\text{hot}} \lambda(T)dT \tag{6.10}$$

$$P = \frac{A}{L}\left(\lambda_{\text{hot}} - \lambda_{\text{cold}}\right) \cdot \Delta T \tag{6.11}$$

These were calculated for the wires to the heater (x4) and wires to sensors T3, T2, T1 and T0. The wires to the heater and T3 were 0.05 m long and the wire lengths used for T2, T1 and T0 were 0.03 m, 0.03 m and 0.01 m long respectively between the heat sink and attachment. The values calculated vary from 1.75×10^{-4}W to 1.46×10^{-6}W.

Electrical heat dissipation

The electrical heat dissipation is the heat created by the resistance of the wire and can be calculated using $P = IV$ as the current and voltage being passed through the wires are known values. The values calculated are in the order 7.5×10^{-8}W for 15 V and 3.0×10^{-7}W for 30 V.

Summary of heat transfer

Table 6.2 summarises the heat transfer within the sample are and cryostat system:. It can be seen that overall the influence of heat transfer within the system is 0.144 %.

Factor	Minimum Error	Maximum Error	Max. Percentage Error
Radiation	5 nW	10 nw	0.0004
Convection	N/A	N/A	Negligible
Electrical Dissipation	1.2024×10^{-6}W	3.006×10^{-7}W	0.05
Heat Conduction	$1.75 \times 10^{-4} \frac{\text{W}}{\text{m}\cdot\text{K}}$	$1.46 \times 10^{-6} \frac{\text{W}}{\text{m}\cdot\text{K}}$	0.135
		TOTAL:	0.144

Table 6.2: Summary of heat transfer in the test cryostat system.

6.5.3 Statistical errors

After the binning procedure and elimination of raw data, there are of the order of 3600 data points left for each temperature step. At each step the power is calculated from the 4-wire measurement across the resistor heater and temperature is calculated from the conversion of resistance into temperature [129]. These data are sufficient to calculate the standard deviation of error on both temperature and power.

Power

Statistical fluctuations are visible in the recorded power data so the error in the applied power to the system was calculated. A 4-wire measurement of power is calculated using the voltage and current values from the Keithley devices [130]. This power reading is taken alongside the temperatures every 0.3 seconds. Once the start of each data bin had been removed, a mean power was taken of the remaining power data. The standard deviation of all remaining data points was taken for each bin and the largest deviation away from the median was found to be 0.420%.

Temperature

The temperature error originates from a multitude of areas: thermal fluctuations, sensor calibration, electronic noise, readout accuracy, thermal coupling and parasitic heat load. The majority of these have been dealt with already when investigating the influence of hardware devices on the system. The key area focused on now is the thermal fluctuations and how the temperature offset between sensors affects the overall results.

The temperature is measured at the base of the setup, T_0, and two measurement sensors, T_1 and T_2 as shown in figure 6.1. In the collected data, a

temperature offset is observed between the sensors as shown in figure 6.5. This temperature offset is corrected to the value of T_0 to reduce the error due to calibration uncertainties.

Fitting Error

After this correction has been made, the median temperature of each sensor is calculated for every step in heater power. The calculation of mean temperature has been discussed in section 6.2. For the differential method of calculating thermal conductivity of the sample, data is fitted to the temperature and thermal resistance ($\Delta T/P$) is calculated and then data for sample only is achieved. The error on these fits must be used together to calculate the error on the final data to be used for the thermal conductivity calculation. The magnitude of error of fit is calculated at each temperature point and the mean magnitude of these is calculated for each is done. The resultant mean magnitude error of fit on temperature is 1.97%.

Length

The sample is setup using a template to assist the copper blocks to be horizontal and parallel to the others in the setup. The distance between these blocks is then measured repeatedly using vernier callipers. The scatter in a repeated set of measurements is ± 5 μm. A further error is introduced due to linear contraction of the sample at low temperatures. At these low temperatures, the sample contracts by 0.0097% of its original length with respect to 300 K [131]. This is taken as negligible. A statistical error can be calculated due to the repeatability of the measurements: this has been done by taking the standard deviation of measurements resulting in an additional error of 1.5×10^{-5} m which calculates to be 0.5% of the total length.

Summary of errors

As shown, there are many sources of error in the system and these have all been investigated either statistically or through calibrations. The total error on thermal conductivity due to these factors can be combined using:

$$\sigma_\lambda = \sqrt{\sigma^2_{\text{length}} + \sigma^2_{\text{power}} + \sigma^2_{\text{temperature}} + \sigma^2_{\text{hardware errors}} + \sigma^2_{\text{heat transfer}}} \tag{6.12}$$

$$= \sqrt{0.5^2 + 0.420^2 + 1.97^2 + 0.163^2 + 0.144^2} \tag{6.13}$$

$$= \ 2.1\ \% \tag{6.14}$$

and the total error on the thermal conductivity is taken as 2.1%

6.5.4 Final result

The final calculated result of the thermal conductivity of stainless steel 316, with the 2.1% error is shown in figure 6.12:

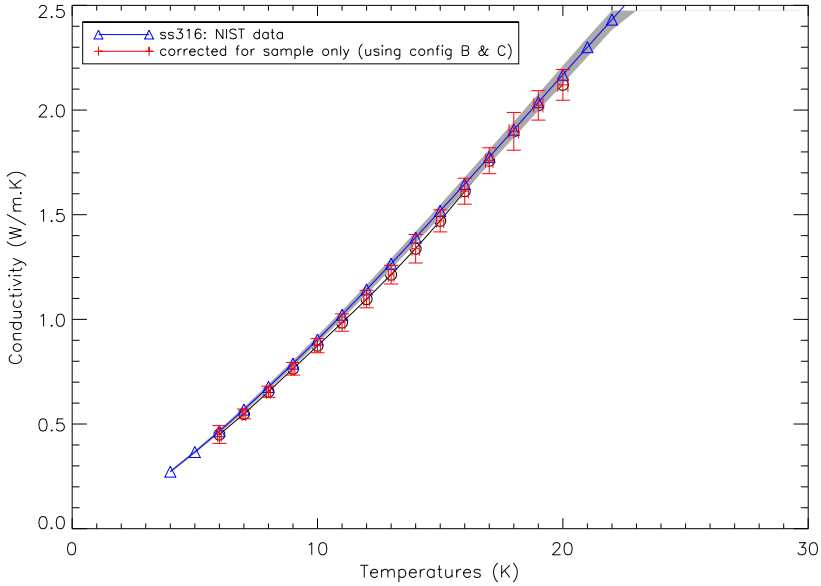

Figure 6.12: Thermal Conductivity of SS316 as quoted by NIST, including their stated 2.1% error margin, and thermal conductivity of SS316 as calculated by the differential method as shown in figure 6.4 [91].

6.6 Conclusions

This chapter has introduced the analysis method used for thermal conductivity measurements. The differential method was implemented to eliminate end effects caused by the copper clamps. Labview™software was used to automate the system, allowing a measurement programme to be entered with the software implementing any changes in experimental setting required. This was monitored over long time periods, at times the system would run for multiple days continuously.

The statistical analysis of data has been shown, including binning data where time frames were allowed for changeover of experimental settings. The issues with temperature stability were improved as shown in section 5.5.1 and the tempera-

ture of the remaining sensors were monitored to accurately determine the temperature at different parts of the sample and system. The total power input to the sample was calculated using the power of devices, parasitic heat conduction and electrical heat dissipation. The effective length of the sample was determined using the differential method to ensure end effects of the copper clamps were eliminated. Stainless steel 316 was tested in the completed system, with initial results showing a 4.2% difference between these results and those published by NIST [91].

All errors in the system were determined, resulting in a combined error of 2.1%. The next chapter will detail the experiments performed using this experimental setup.

Chapter 7

Experiments and Results

Various experiments were conducted in the cryostat system: thermal cycling of materials for the Mid-Infrared Instrument for the James Webb Space Telescope, electrical resistivity measurements of aluminium foam for the ISIS experiment, thermal conductivity measurements of an experimental standard of stainless steel 316 and latterly thermal conductivity across a hydroxy-catalysis bond in boron-doped silicon.

This chapter presents the procedure of each experiment alongside results. Suggestions for further work in each area is discussed.

7.1 Thermal cycling

Thermal cyclic testing was carried out using a Janis Gifford-McMahon closed cycle cryostat with Helium-4 as the liquid cryogen. The cryostat operated alongside a Lakeshore 370 Temperature controller and a Lakeshore 340 Resistance bridge as described in chapter 5. The sample areas a cool down time is of approximately

one hour. The system was automated to allow a temperature change to be made once a stable period of 90 minutes had been identified

7.1.1 Samples

The following samples, as shown in 7.1 were tested:

Spectral black anodised samples Three spectral black anodised samples (#364, #366, #370) with the following specification were tested: Part number MIRI-DW-00099-ATC with front surface diamond fly cut then finished with: Inorganic Specular Black Anodise to MIRI-PR-00009-ATC. (Protection des Metaux Process reference OA0MB000 O (XI) S. Noir Minéral Brillant).

Filament unit disc One filament unit disc (#0006) with the following specification was tested: MIRI-DW-00008-CDF serial number #0006, nickel/gold plated to MIL-G-45204 type II grade C by Pender Plating, Dorset. This component was coated at the same time as the flight hardware (ref MIRI-DP-00004-CDF issue 3).

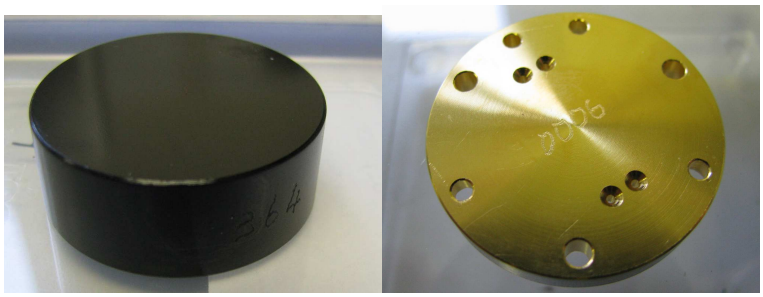

(a) **(b)**

Figure 7.1: MIRI samples: (a) Black anodised sample, part #364 and (b) Filament unit disc, part #0006.

7.1.2 Setup/measurement method

The samples were affixed to a copper sample holder as shown in figure 7.2. The cryostat was closed, pumped to a vacuum of 3×10^{-3}mbar and lowered to a temperature of 3 K. This temperature was held until the sample temperature had stabilised for a period of 90 minutes. The temperature was then increased to 290 K using heaters built into the cold head. After the same stabilisation time of 90 minutes had been reached the cycle was repeated. The stable period was held to ensure the sample had cooled to the required temperature.

The samples were tested in two runs; the first with the gold plated disc #0006 and the black anodised disc #364 and the second with the two black anodised sample #366 and #370. The samples were screwed on to the sample holder and a Cernox thermometer was attached to sample #0006 (7.2) and used to carry out resistance thermometry. In the first run the thermometer was attached to the sample with a screw. In the second run, a method was tested by attaching the thermometer to the sample using Kapton tape, a polymer tape commonly used in astronomical instruments. The contact between the thermometer and the sample was not sufficient to record the temperature so the experiment was re-run with the thermometer attached to the sample holder. The stability below 10 K was shown in the second run by the correlation between results for the two runs.

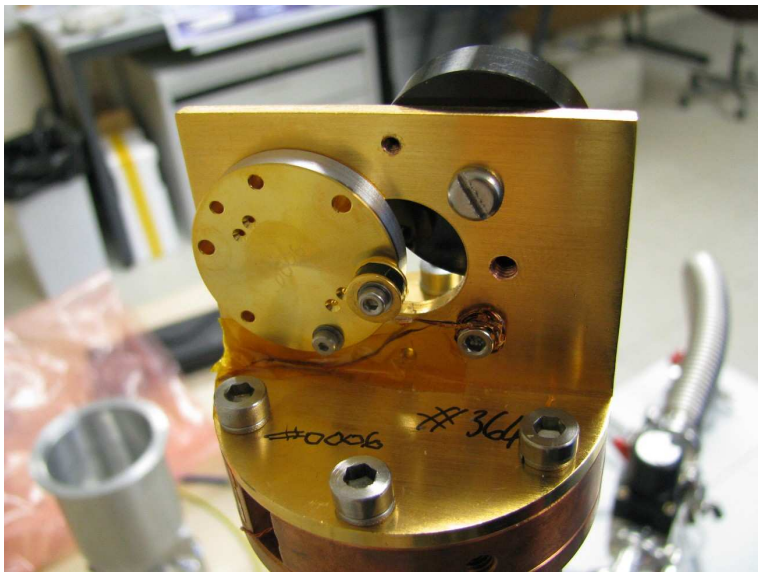

Figure 7.2: Spectral Black Anodised Sample and Filament Unit Disc as setup on cryostat cold head.

Adhesion testing

Post thermal cycling adhesion testing was performed by the United Kingdom Astronomy Technology Centre (UKATC) by applying a strip of tape across the face and down one edge of the component. The tape was then withdrawn by a slow manual pull perpendicular to the surface. Following the adhesion test the samples were inspected for surface damage and the tape was inspected against a white background for signs of the coating coming off. Note that no optical measurements were performed since because the function of both coatings does not depend on optical flatness, and a visual check of surface damage is sufficient to be sure that there is no change in optical properties. The test was performed on samples #366, #364, #370. Inspection of the samples and the tape following the adhesion test showed no sign of any damage to the coating and no sign of any particles adhering to the tape. The samples all passed the adhesion test.

7.1.3 Results

The data shows that all samples have been thermally cycled 10 times between the temperatures 3 K and 290 K as required.

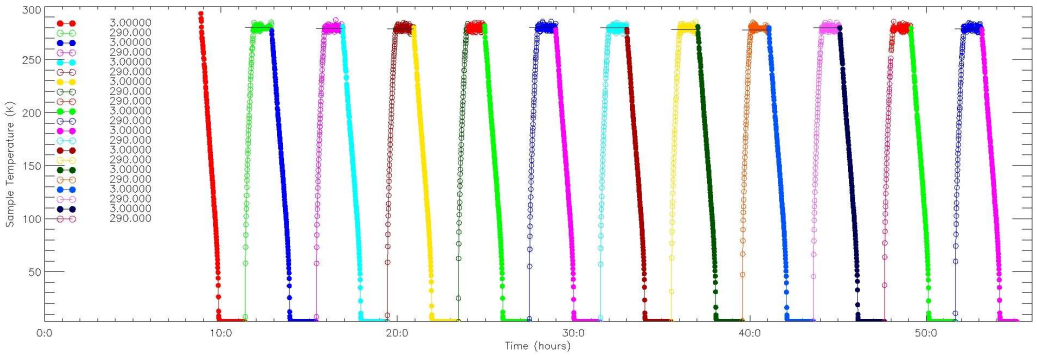

Figure 7.3: MIRI sample temperature as a function of time, #366 and #370.

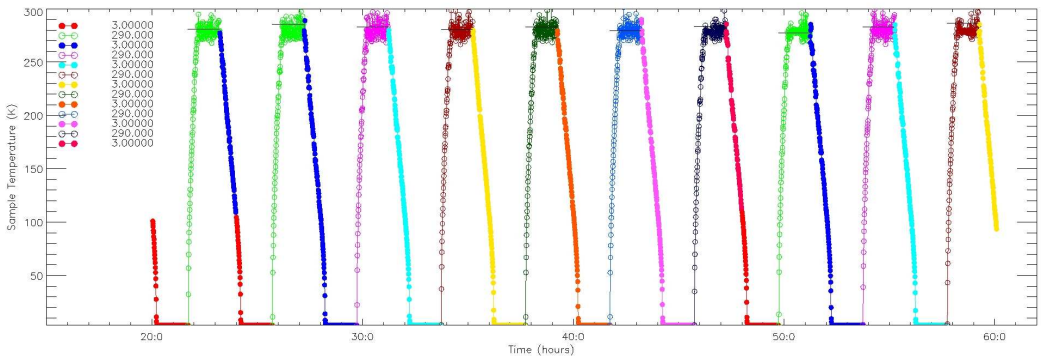

Figure 7.4: Sample temperature as a function of time, #0006 and #364.

7.1.4 Conclusion

It can be seen from the graphs in figures 7.3 and 7.4 that the thermal cycling was completed successfully. Although these tests were carried out before the system was completely debugged, the results were conclusive to the aims of the experiment. The UKATC were looking for the parts to be cooled repeatedly to below 10K and although there is a large instability in temperature as shown in the

graphs, I am confident that the temperatures reached were true temperatures as calibrated temperature sensors were used. This temperature cycling has achieved the prerequisites of the experiment plan. The Adhesion carried out by UKATC staff testing showed that both coatings were undamaged by the thermal cycling [132].

7.2 Electrical resistivity

Once the cryostat system was thermally stable, measurements of the electrical resistivity of commercially available Alloy 1199 Aluminium Foam were undertaken for the ISIS experiment at the Rutherford Appleton Lab, UK [133]. This section introduces the experimental procedure and discusses results.

7.2.1 Sample and measurement procedure

Two samples of Aluminium foam were provided as shown in figure 7.5 and were bent into an 'S' shape to fit the sample area. Silver epoxy was used to attach tabs to allow the sample to be screwed to the sample holder and to connect four manganin wires to allow a 4-wire resistance measurement to be carried out. The temperature of the system was incrementally raised from 4.4 K to 295 K while the resistance of the sample was measured at each step. The resistance values were converted into resistivity using the known room temperature resistivity value of Aluminium, 2.7×10^8 Ω m, as the effective geometric factor of the foam was unknown. This room temperature value does not vary much with purity at high temperatures, unlike at low temperatures where the variation is greater.

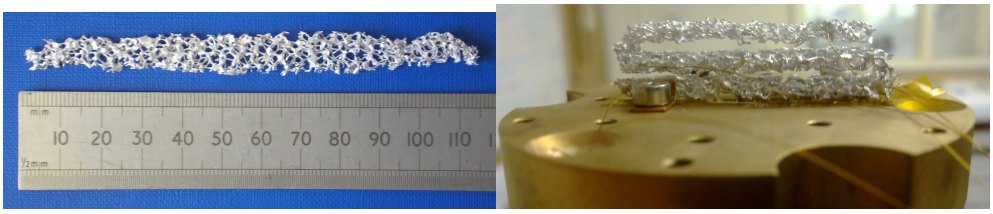

(a) Original form of aluminium foam

(b) Aluminium foam bent to fit in sample space

Figure 7.5: Alloy 1199 aluminium foam: (a) original form (b) bent for the experimental setup.

7.2.2 Results and conclusion

Theoretical fits to the resistivity data were plotted, these are calculated using the equations taken from the book by Hust & Lankford [134]. We note that the value for the parameter P4 is given as 1.26 in the original text, but this appears to be a misprint of the value -1.26 giving agreement with the figures in reference [134]. It can be seen in figure 7.6 that the data collected for both Aluminium foam samples were in agreement with the theoretical predictions for RRR (Residual Resistivity Ratio) values of 11 and 15 respectively.

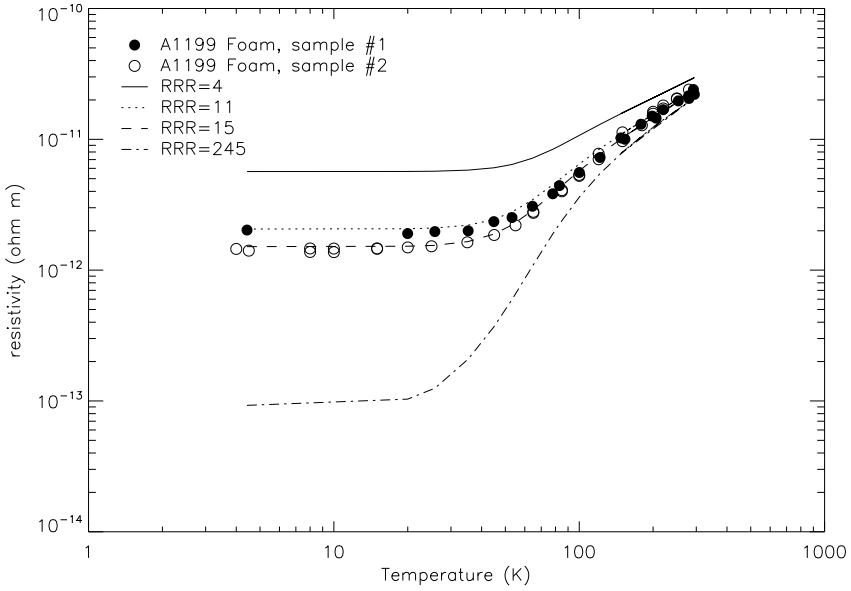

Figure 7.6: Resistivity measurements of Aluminium foam from 4 K to Room temperature. The lines represent theoretical fits calculated from the equations in Hust and Lankford [134] for various RRR values.

7.3 Thermal Conductivity

The main purpose of the cryostat system was to determine the thermal conductivity of samples. Initially stainless steel 316 was tested as a reference sample to confirm the accuracy of the system. Further details of these tests and results are in section 6.4.1. The thermal conductivity of hydroxy-catalysis bonded p-type boron-doped silicon was investigated. Initial experiments were carried out using the differential method to determine the exact conductivity of the boron-doped silicon over a range of temperatures. The exact doping is unknown so these are shown with a selection of boron-doped silicon samples. Tests were then carried out on the bonded pieces. This section gives a description of the experiments completed, results and further work.

7.3.1 Bonded silicon

Silicon is being used more in developments of new instrumentation, especially those operating below 25 K. Methods have been developed for bonding silicon to ensure high stability, low stress joins can be constantly produced. Hydroxide catalysis bonding is a technique which was developed and used successfully for the telescope construction in the Gravity Probe B space experiment mission [135]. It is compatible with requirements for low temperature, high vacuum and precision alignment. These bonds can be created between a variety of materials if a silicate-like network can be formed at the material surfaces; this is the case for most oxide containing materials [135] and is created using an alkaline bonding solution dissolved in water. When the bonding solution comes into contact with the bonding surfaces the hydroxide catalysis commences; this consists of three steps; hydration and etching, polymerization and dehydration [136]. These steps have been described in detail in previous papers [137, 138].

This bonding technique has been successfully been adapted for use in the construction of the mirror suspensions of laser interferometric gravitational observatories; it was applied in the GEO 600 detector in order to create a 'monolithic' suspension of the fused silica mirrors. Fused silica fibres were welded to fused silica interface pieces, called 'ears' [139] bonded onto the sides of the mirror using the hydroxide catalysis bonding technique [140].

Currently, many experiments have been performed to test the mechanical properties of the hydroxide catalysis bonds, but the thermal conductivity has not been investigated in great detail. This study was planned to examine the thermal conductivity across a variety of thicknesses of bond between two 'ears' of silicon.

Block No.	Oxide Thickness (nm)	Difference in Oxide Layers (nm)
2133	156.3	
2147	131.4	24.9
2131	168.1	
2143	131.2	36.9
2127	133.9	
2135	161.9	27.7

Table 7.1: Thickness of bonded silicon samples: particular attention has been paid to test samples with differing oxide thicknesses.

7.3.2 Samples and experimental procedure

The rectangular silicon blocks used (20 mm × 10 mm × 5 mm) were from Prolog, boron doped P-type boron-doped silicon ingot with <100> crystal orientation. The bonding surface was one of the 5 mm × 10 mm surfaces, so that after bonding a sample was created with dimensions 40 mm × 10 mm × 5 mm.

The samples were placed in a tube furnace at $\sim 1000°C$ for periods of time between 5 and 55 minutes to grow thermal SiO_2 layers of various thicknesses. A wet nitrogen method was used; nitrogen gas saturated with water was passed through the furnace for the duration of the oxidation. The bonds in the samples tested vary in thickness from 209 nm – 295.8 nm with full details given in table 7.1. The difference in thickness of oxide layers on the two bonded silicon ears vary from 0.4 nm to 27.7 nm. An additional sample was available with oxide thickness of around 25 nm on each ear but it was broken before testing began.

7.3.3 Results

Unbonded sample The thermal conductivity of one unbonded, 'blank' sample was determined from 4 – 19 K. It was shown to increase from 24.06 – 46.44W/m K. The result of these tests were compared to previously published data, but as the boron-doping levels of this sample are unknown, two results were chosen which also were a p-type structure with boron doping [104]:

- **Holland (1961):** p-type single crystal; boron doped; cross-section 0.616×0.623 cm.
- **Slack (1964):** polycrystalline; p-type; major impurity boron; 1.24 cm effective diameter; 3.2 cm long.

The thermal conductivity of the measured sample in the temperature range 4–19 K remains under 50 W/mK and follows a similar trend to the sample previously measured by Slack [104]. The large errors seen in the measured sample at 9–10 K were thought to be due to temperature instabilities in the system as this is where the changeover of PID settings for filtering temperature data occurs (for further information see appendix C.2.2).

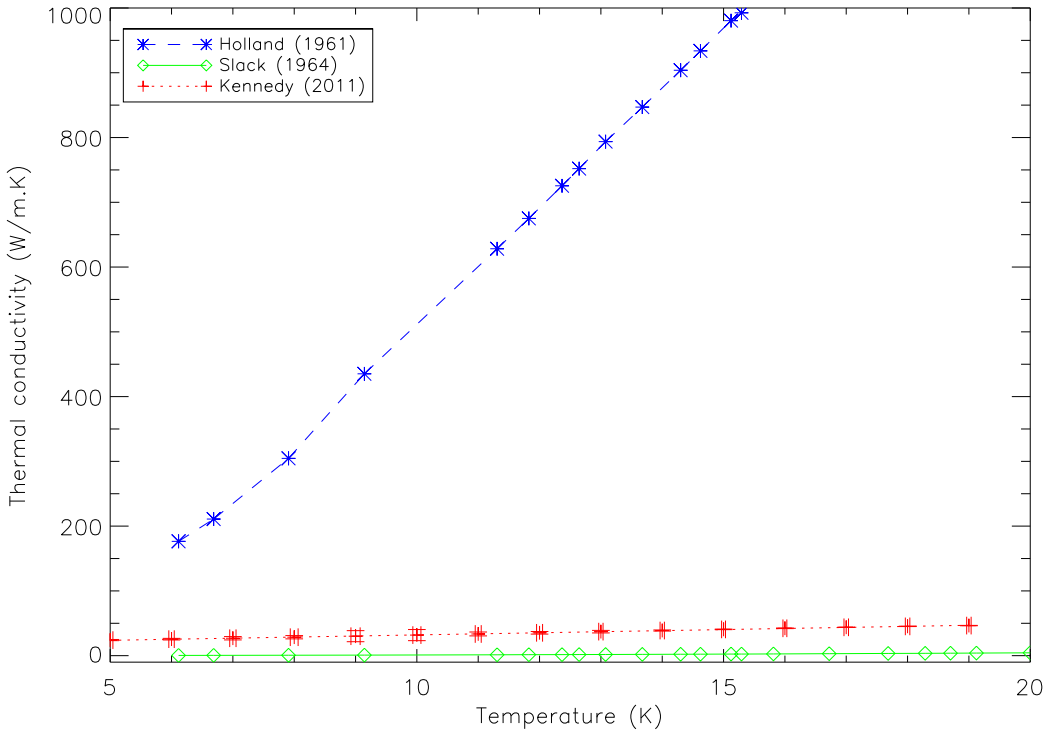

Figure 7.7: Thermal conductivity of unbonded boron-doped silicon, as compared to Holland, line 25 and Slack, line 38, in [104].

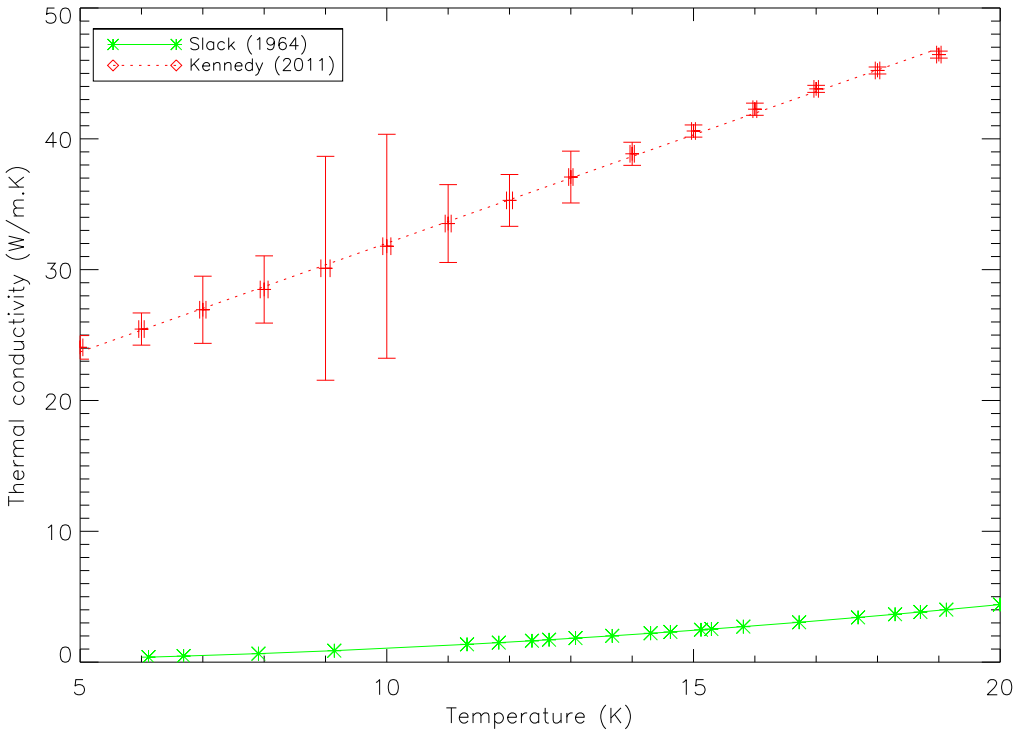

Figure 7.8: Thermal conductivity of unbonded boron-doped silicon, as compared to Slack, line 38 in [104].

Bonded samples The three available bonded samples were available, each with a varying thickness of oxide layer hence varying thicknesses of bonds. Investigations in to the thermal conductivity across the silicate bond were initiated. Due to time constraints of the project, only one bonded sample entered the test programme. After the first cool down the sample was found to be broken as illustrated in figure 2.1. It is thought to have broken as the system was returned to room temperature after collecting data, as the cold head heater was used to increase the temperature of the experimental setup. As the system is optically closed and the exact time of the break cound not be determined, the data was disregarded and the experiment re-run. As the measurement programme drew to an end, two data sets had been collected but they were not sufficient to calculate

the thermal conductivity across the bond.

7.3.4 Conclusions

The measured thermal conductivity of p-type boron-doped silicon is in a reasonable range for the expected results. Further testing would be required on bonded samples to determine the conductivity across the bond prior to implementation in an instrument. The results obtained have been used to advise the University of Glasgow on the experimental setup and process of measurements for further tests to be completed.

7.4 Further work

This section looks at carrying out a more in depth critical analysis of previously published data, and suggests further work which could be carried with the system designed for the work contained within this thesis.

7.4.1 Critical analysis

The critical analysis completed for this thesis was severely limited by access to published papers and availability of information on systems used for data collection. Further data was digitised but not included due to the following recurring reasons:

- Access to data through limited access to published papers
- Difficulty in securing information on primary source of data
- Limited access on systems used for data capture
- Limited ability to digitise data through quality of published data

A more in depth analysis could be completed if these points were addressed and further information was accessible for a variety of materials.

7.4.2 Hardware

Thermal fluctuations

As discussed in section 5.5.1, a huge contributor to the thermal fluctuations is the mechanism of the Gifford McMahon cryostat: the pistons are very close to the cold head, so the continued compression and expansion of gas means there is also a fluctuation in the cold head. It is proposed that the integration of a damping block would reduce these fluctuations further. Inserting the block would be an intricate process as indium foil would be required to act as a filler and the 6 screws connecting the cold head and sample holder would need to be evenly tightened to avoid any misalignment of the blocks.

Conversely, if when inserted it does not correct for the thermal fluctuations then this could cause further problems as remnants of indium would be left on the cold head and thermal contact would be reduced.

Temperature sensors and sample holder

The Cernox™sensors used during the course of these experiments were sufficient for setting up the system, but due to the large size of them compared to the small samples being measured it is felt that other sensors would be more suitable. If smaller temperature sensors were used instead, the sample holder could be redesigned. The suggested sample holder would have minimal end effects, and be more robust, removing the further errors introduced by the current setup by mis-alignment of clamps.

Support hardware

Ideally, this system would have more resistance bridges so all channels could be monitored simultaneously. This would allow the temperature changes to be monitored more fluidly and therefore any temperature changes could be tracked instantly. The integration of further support hardware would allow a more thorough analysis to be obtained for materials.

7.4.3 Materials measurement programme

The materials measurement programme would be continued, beginning with testing further hydroxy-catalysis bonded p-type boron-doped silicon. Further investigations in to the thermal conductivity across different bond thicknesses would be completed, examining the effect of repeated cool-downs. This work is planned to take place in the Institute for Gravitational Waves at the University of Glasgow.

As polymers are being more widely used in instrumentation, but data is still sufficiently limited, the continued programme would conduct investigations in to materials such as peek, torlon and vespel. A collaboration would be set up with a partner department so the same samples could be tested in two different systems to ensure reproducibility. Although data is most sparse at low temperatures, ideally the system would be calibrated so accurate results could be obtained from room temperature down to a few Kelvin. Specifically, this would include further work on reducing radiative effets at temperatures above 50 K by implementing a material such as Multilayer Insulation (MLI)

7.4.4 3ω measurements

Samples were prepared for the 3ω measurements, although due to issues with the system and a greater time spent on calibrating than planned, they were

not implemented. Figure 7.9 illustrates the two layouts which were designed to investigate the surface thermal conductivity of materials. It is proposed that steady state and 3ω analysis could be carried out in the same instrumentation. This would involve sputtering the 3ω tracks on the side of a sample prepared for steady state measurements. Although it is not thought the measurements could be done simultaneously, it is proposed that at each temperature step a measurement could be made with each apparatus hence determining in depth details of each material.

This would be a large piece of work which would require a great amount more development before results could be obtained.

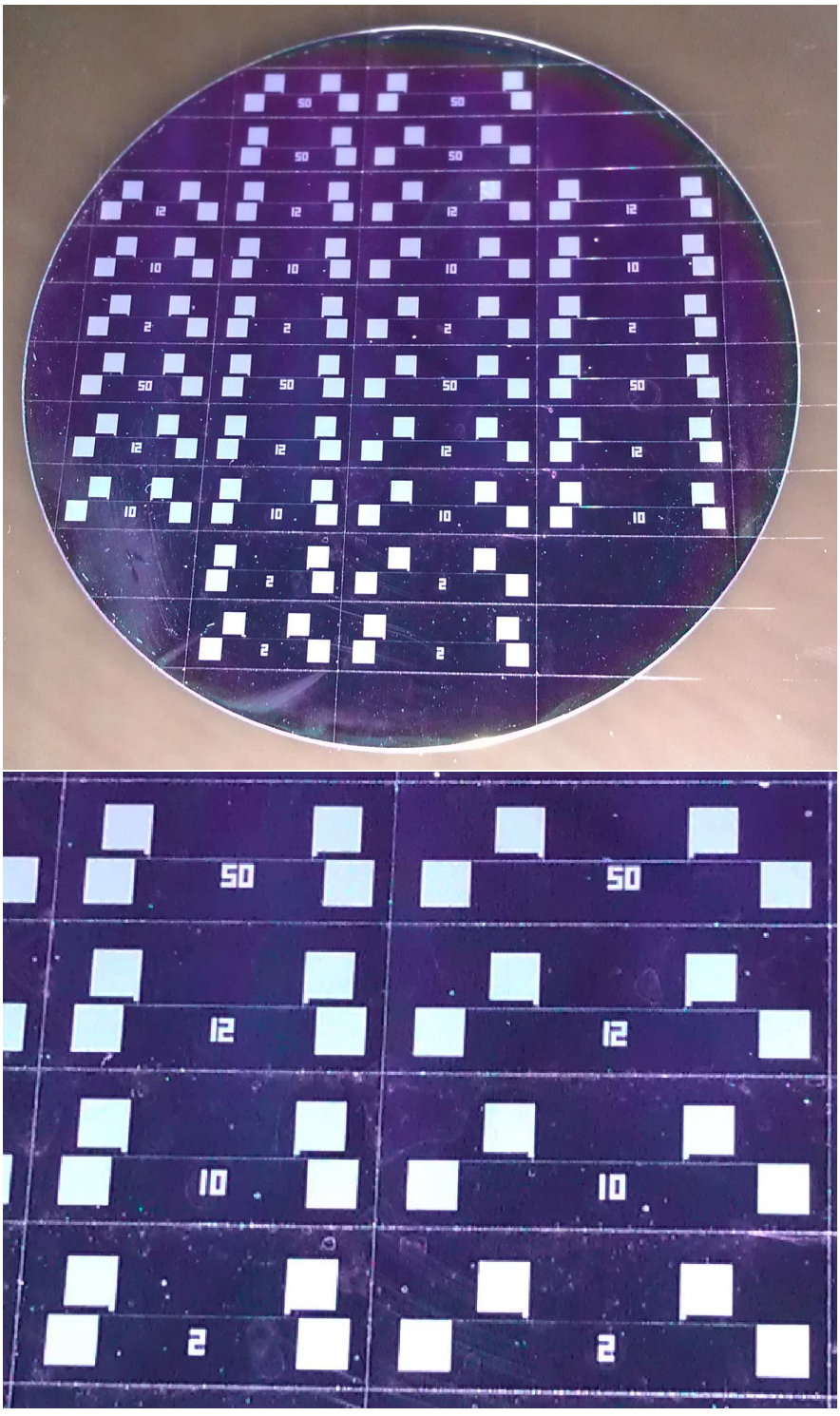

Figure 7.9: 3ω samples showing one track to act as a heater and temperature sensor, with four pads for electrical connections.

7.5 Final comment

The work contained within this thesis demonstrated the difficulties with setting up a material measurement process at low temperatures. While the whole purpose of the instrument was to make thermal conductivity measurements, various problems were still encountered and overcome. If organisations are to run these measurements in an unsuitable system during the construction stage of a large instrument to assist with identifying suitable materials, these issues could be detrimental to an instrument as a whole.

The preparatory work for thermal conductivity measurements has been completed with initial results for p-type boron-doped silicon determined. This work is currently being used to advise the University of Glasgow on continuing the measurements in a specially tailored system.

Appendix A

Fitting Regimes

A.1 Chebyshev Fitting for Temperature Sensor Calibration

The temperature (T) can be calculated by doing the sum of Chebyshev coefficients (a_n) and Chebyshev polynomials (t_n):

$$T(x) = \Sigma a_n t_n(X) \tag{A.1}$$

where $T(x)$ is the temperature in Kelvin, t_n is a Chebyshev polynomial, a_n is a Chebyshev coefficient and:

$$X = \frac{(Z - Z_L) - (Z_U - Z)}{Z_U - Z_L} \tag{A.2}$$

using the resistance of the sensor to compute $Z = log_{10}R$ with Z_U and Z_L being the upper and lower limits of Z over the fit range. The polynomials can be calculated from:

$$t_{n+1}(X) = 2XT_n(X) - t_{n+1}(X) \tag{A.3}$$

$$t_0(X) = 1 \tag{A.4}$$

$$t_1(X) = X \tag{A.5}$$

$$\tag{A.6}$$

or alternatively using:

$$t_n(X) = cos[n.arccos(X)] \tag{A.7}$$

with uncertainty of fit, σ_{fit}:

$$\sigma_{fit}^2 = \frac{\Sigma\left(T_i - T_{calc}^2\right)}{N-n} = \frac{N}{N-n}\left(\Delta T_{RMS}^2\right) \tag{A.8}$$

where T_i is temperature of point i, T_{calc} is temperature calculated from polynomial equation for point i, N is the number of data points in the fit range, n the number of fit coefficients and ΔT_{RMS} is the root mean square deviation of the fit.

Appendix B

Differential method of calculating thermal conductivity

As explained in section 6.4, the end effects of the copper clamps must be removed to calculate the thermal conductivity of the sample only.

B.1 Derivation of sample conductivity

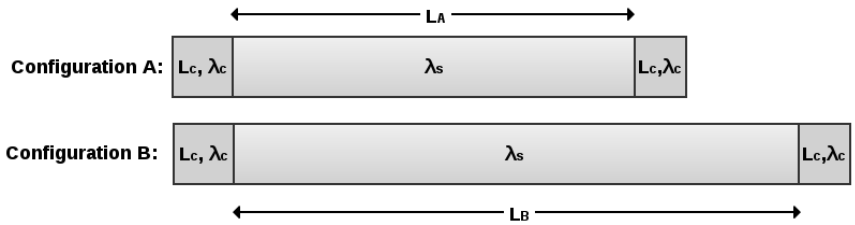

Figure B.1: Configurations A and B as used for the differential analysis for calculating thermal conductivity. The copper collars cause unknown end corrections that are the same in each case.

Each configuration is a complex system made of the sample and two copper sensor clamps as shown in figure B.1. This gives us the conductance, G, of each section as:

$$G_A = \frac{A \cdot \lambda_{sample}}{L_A} \qquad G_B = \frac{A \cdot \lambda_{sample}}{L_B} \qquad G_c = \frac{A \cdot \lambda_c}{L_c} \tag{B.1}$$

Using the above equations, we can define the conductance of each configuration taking into account the two copper clamps plus the sample itself. In examining the resistance of each configuration so we can make a direct comparison. As $R = 1/G$ we combine these as follow:

$$R_{\text{configuration A}} = \frac{1}{G_{\text{configuration A}}} = \frac{1}{G_c} + \frac{1}{G_A} + \frac{1}{G_c} = \frac{2}{G_c} + \frac{1}{G_A} \tag{B.2}$$

$$\tag{B.3}$$

$$R_{\text{configuration B}} = \frac{1}{G_{\text{configuration B}}} = \frac{1}{G_c} + \frac{1}{G_B} + \frac{1}{G_c} = \frac{2}{G_c} + \frac{1}{G_B} \tag{B.4}$$

$$\tag{B.5}$$

furthermore we know from equation B.1 that:

$$\frac{1}{G_{\text{configuration A}}} = \left(\frac{\Delta T}{P}\right)_c + \left(\frac{\Delta T}{P}\right)_A + \left(\frac{\Delta T}{P}\right)_c \tag{B.6}$$

$$\frac{1}{G_{\text{configuration B}}} = \left(\frac{\Delta T}{P}\right)_c + \left(\frac{\Delta T}{P}\right)_B + \left(\frac{\Delta T}{P}\right)_c \tag{B.7}$$

$$\tag{B.8}$$

so we can look at each complete configuration as:

$$G_{\text{configuration A}}: \quad \frac{1}{\frac{2}{G_c}+\frac{1}{G_A}} = \left(2\cdot\frac{P}{\Delta T}\right)_c + \left(\frac{P}{\Delta T}\right)_A \tag{B.9}$$

$$G_{\text{configuration B}}: \quad \frac{1}{\frac{2}{G_c}+\frac{1}{G_B}} = \left(2\cdot\frac{P}{\Delta T}\right)_c + \left(\frac{P}{\Delta T}\right)_B \tag{B.10}$$

$$\tag{B.11}$$

Now to calculate the conductivity of the sample using the systems of configurations A and B as described above, the conductance of the shorter sample, A, needs to be subtracted from the longer sample, B. As mentioned previously, the clamps are assumed to be the same although the contact conductance will vary slightly [1]. The sample conductivity can then be defined by:

$$\frac{1}{G_{\text{sample}}} = \left(\frac{1}{G_{\text{configuration B}}}\right) - \left(\frac{1}{G_{\text{configuration A}}}\right) \tag{B.12}$$

so:

$$\left(\frac{2}{G_c}+\frac{1}{G_B}\right)-\left(\frac{2}{G_c}+\frac{1}{G_A}\right) = \left[\left(2\cdot\frac{\Delta T}{P}\right)_c + \left(\frac{\Delta T}{P}\right)_B\right]-\left[\left(2\cdot\frac{\Delta T}{P}\right)_c + \left(\frac{\Delta T}{P}\right)_A\right] \tag{B.13}$$

the effects of the sensor clamps cancel out leaving:

$$\frac{1}{G_B} - \frac{1}{G_A} = \left(\frac{\Delta T}{P}\right)_B - \left(\frac{\Delta T}{P}\right)_A \tag{B.14}$$

putting back in the terms from equation B.1:

$$\lambda_{\text{sample}} = \frac{L_B - L_A}{A\cdot[(\frac{\Delta T}{P})_B - (\frac{\Delta T}{P})_A]}. \tag{B.15}$$

[1] The exact difference in the effect of these clamps is unknown, but can be partly investigated.

Appendix C

Further details of measurement system

C.1 Problems with initial setup

Various problems were discovered with the initial setup of the cryogenic measurement system. This section gives further details on some of those problems.

C.1.1 Instability with AVS resistance bridge

The cryostat system was run with a sample of solder looking at the electrical resistance using an AVS resistance bridge. This was carried out to check the system was in full working order and the support hardware was sufficient for the tasks in hand. An initial cool down showed a huge instability in the resistance measurements during the cool down and an unexpected trend of resistance was found, illustrated in figure C.1. It can be seen that the trend of the resistance

is very regular and square, as if there is filtering on the results to take away any background signals. The resistance either fluctuates over an $100\mu\Omega$ range or is steady. Random large fluctuations of up to $6000\mu\Omega$ also exist

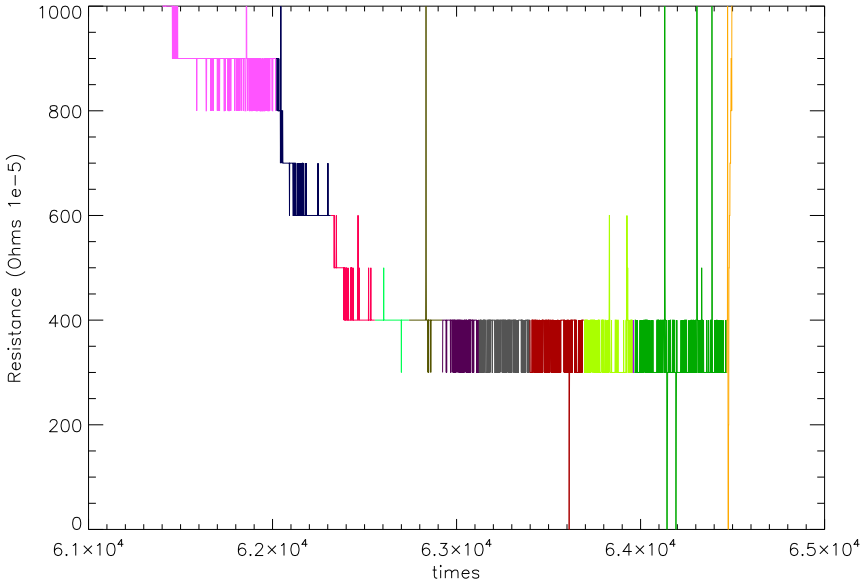

Figure C.1: Lower temperature region of solder resistance values.

During further testing carried out with the AVS resistance bridge, this discontinuity in resistance values can be seen. Further to the trends seen in figure C.1, we can see a huge discrepancy in resistance values during the next cool down, leading to such an instability in the system a short circuit was assumed. Figure C.2 shows an example of the resistance values being recorded in the system. In this case, when the system was warmed up this discrepancy disappeared and we were left with the regular trend instead.

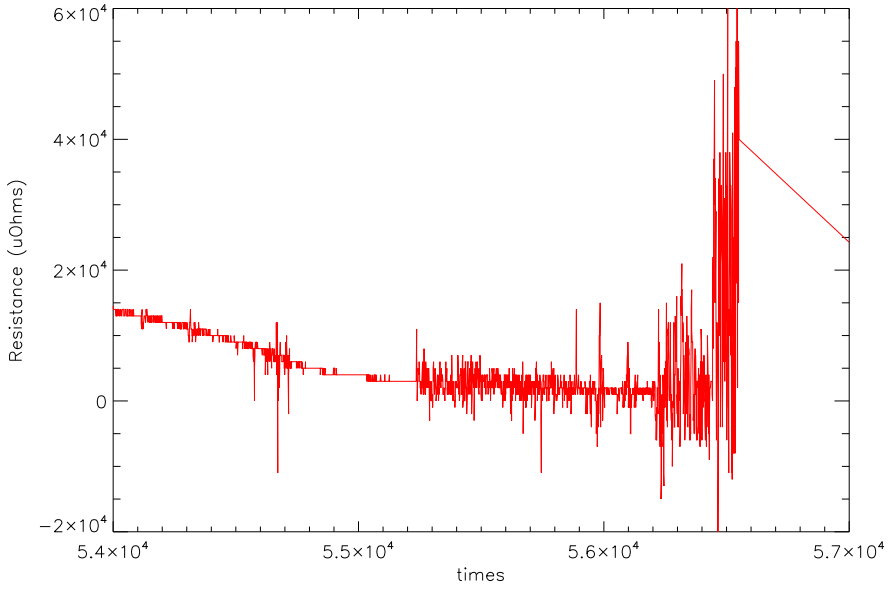

Figure C.2: System instability using the AVS resistance bridge

Some of the problems with instability of the system were addressed by improving the manual setup of the sample, improving electrical insulation and by investigating the AVS Resistance bridge settings to have optimum 'real' results coming through.

At this point in time, the AVS resistance bridge only recorded resistance and time, so temperature needed to be calculated using the calibration conversions of the sensors. One sensor had this provided and the others were calibrated using it.

A copper sample was loaded into the system to look further at the stability and fluctuations. Figure C.3 shows a cool down (with a slight warming in the middle) to base temperature then the beginning of warming up again. It can be seen that large random fluctuations are still occurring, but the general trend of the resistance with varying temperature is steadier. Manual data collected was compared to the data collected by the labview system to ensure continuity of

manually collected data.

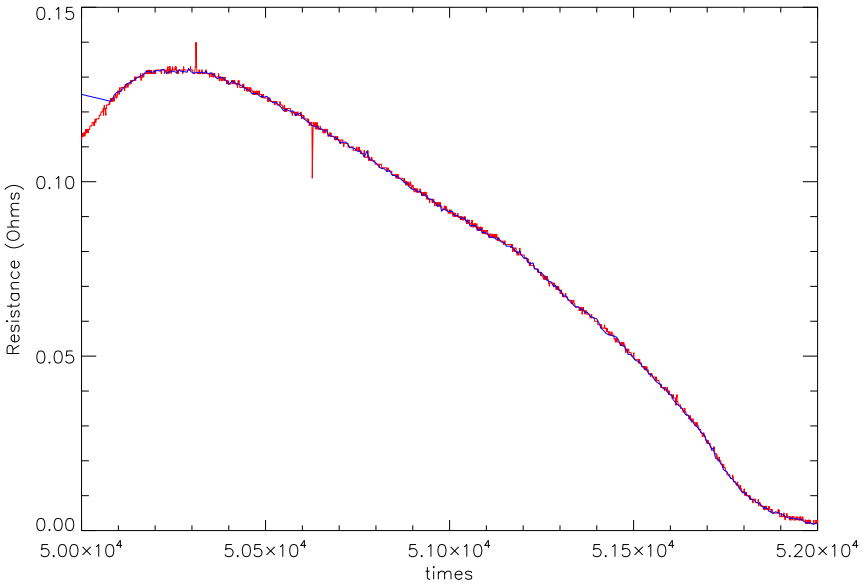

Figure C.3: Comparison of manually collected data (black) and automatically collected data (red).

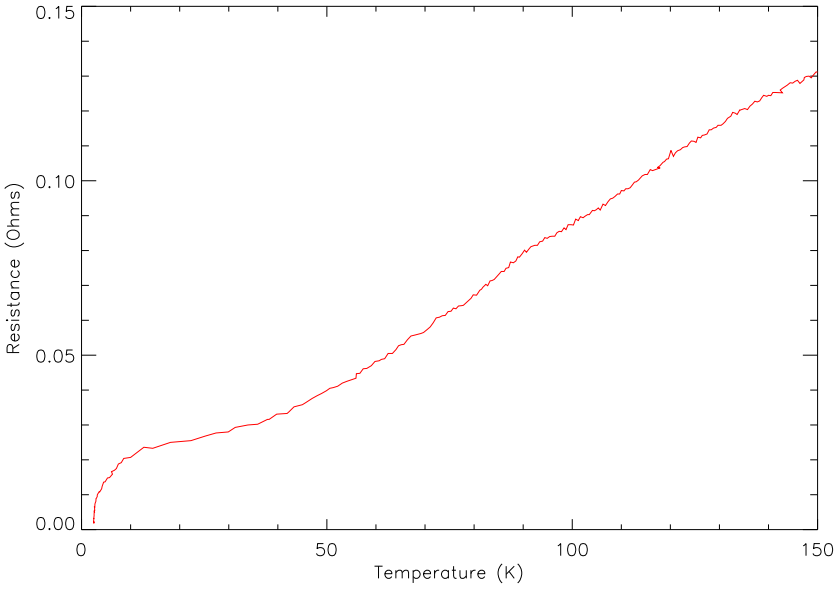

Figure C.4: Copper ribbon resistance varying with Temperature.

C.2 De-bugging of the final experimental setup

C.2.1 Shielding

Radiation Shield The cryostat has two radiation shields built into the setup: one on the first stage at 60 K and cone on the second stage (cold head and sample holder) at 2 K.

Cable Shielding The outer cables of the cryostat (leading to support hardware) needed to be shielded to reduce electrical noise and electromagnetic radiation which may cause interference. The shield can be created by braiding two conducting wires into a twisted pair hence inductively cancelling some of the noise. An alternative method is to have the twisted pair surrounded by a grounded metallic layer.

Some of the cables were already shielded. One of the cables which was not grounded was the cable for the Lakeshore 370 Resistance Bridges. A shielding was made from wrapping the cable in aluminium foil with copper wire wound round and grounded to both the cryostat and pre-amplifiers.

C.2.2 Manual settings on hardware

PID Controls With the system held at low temperatures, the Partial, Integral and Differential (PID) settings of the Lakeshore 340 Temperature Controller were investigated to find the optimum stability. The PID settings control and analyse the error in the amount of power sent to the built in heaters and adapts to narrow the error. This gives the outcome of the smallest error possible, hence the smallest fluctuations in temperature for keeping the system stable at a pre-set temperature.

Filtering Data was collected with both filtering and no filtering by the Lakeshore instruments. When the filter setting is implemented, the Lakeshore automatically filters the data before the output is produced. This means if the filter is on, the extreme real points of measurement may not be defined in the output.

Settings: **Temperature:** 4K, **Heater:** None, **PID:** None, **Output:** Manual Output.

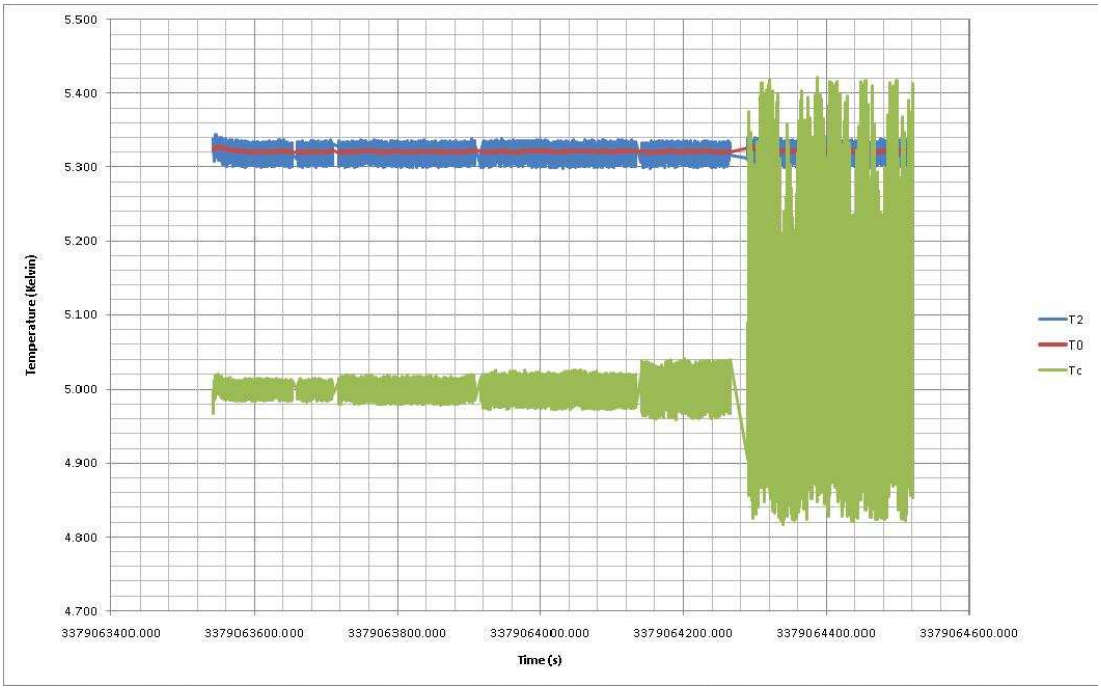

Figure C.5: *Results of tests for filtering data using the Lakeshore 370 Resistance Bridge, monitoring sensors* T_c, T_0 *and* T_2 *placed on the cold head, mid-sample and the top of the sample respectively.*

The filter settings applied were as follows:

FILTERED	
Temperature	Base - 30K
Heater	auto
PID	20, 100, 5
Manual Output	25%
Filter Settings	40 points, 1% window

(a) Before

UNFILTERED	
Temperature	Base - 30K
Heater	10W
PID	20, 100, 5
Manual Output	25%
Filter Settings	none

(b) after

Figure C.6: *Filter settings tested for Lakeshore 370 Resistance Bridge.*

Reading No.	Points	Window (%)	Approx. Drift (K)
1	50	5	0.035
2	50	1	0.035
3	40	1	0.04
4	30	1	0.05
5	20	1	0.09
6	none	none	0.6

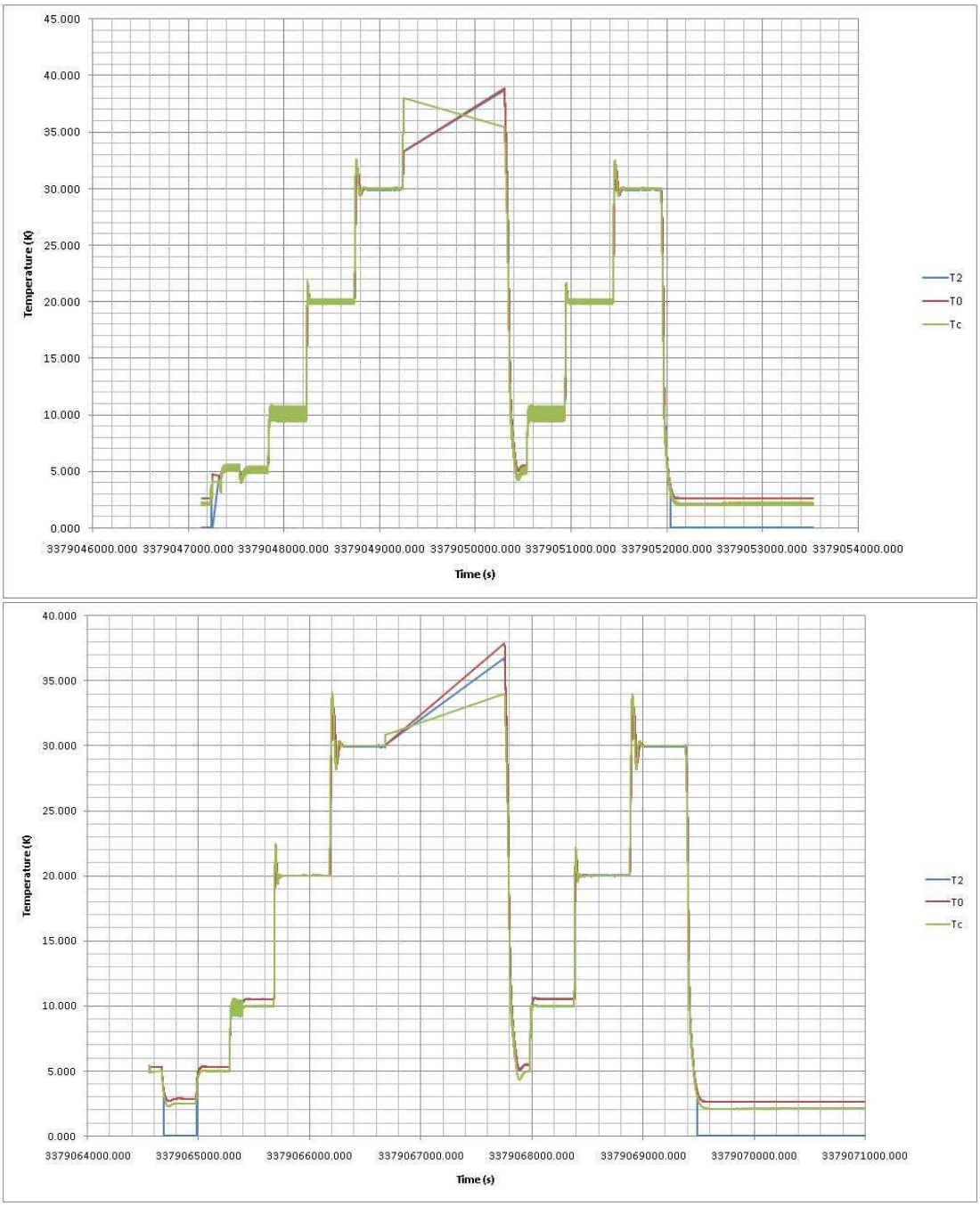

Figure C.7: *Data sets from Lakeshore 370 Resistance Bridge: (a) Unfiltered data set (b) Filtered data set. Central 'jump' relates to removing the 80 K data from the set.*

It can be seen that filtering reduces the noise in the system somewhat, but this is merely reducing the number of data points output from the device, it is not actually altering it in any way. This filtering can be done in the IDL pipeline if necessary rather than in the device.

Algorithms for PID Settings

The Proportional, Integral and Differential (PID) settings can be set manually or automatically by the Lakeshore 340. The Lakeshore 340 Temperature Controller uses an algorithm called PID control for closed-loop control operation. The control equation for the PID algorithm has three variable terms, P, I and D. The system can be tuned using these. The system was tested with and without PID settings chosen, with the following settings and the results shown in figure C.8.

Settings:

Temperature: 4K-20K

Heater: 10W

PID: Varies

Manual Output

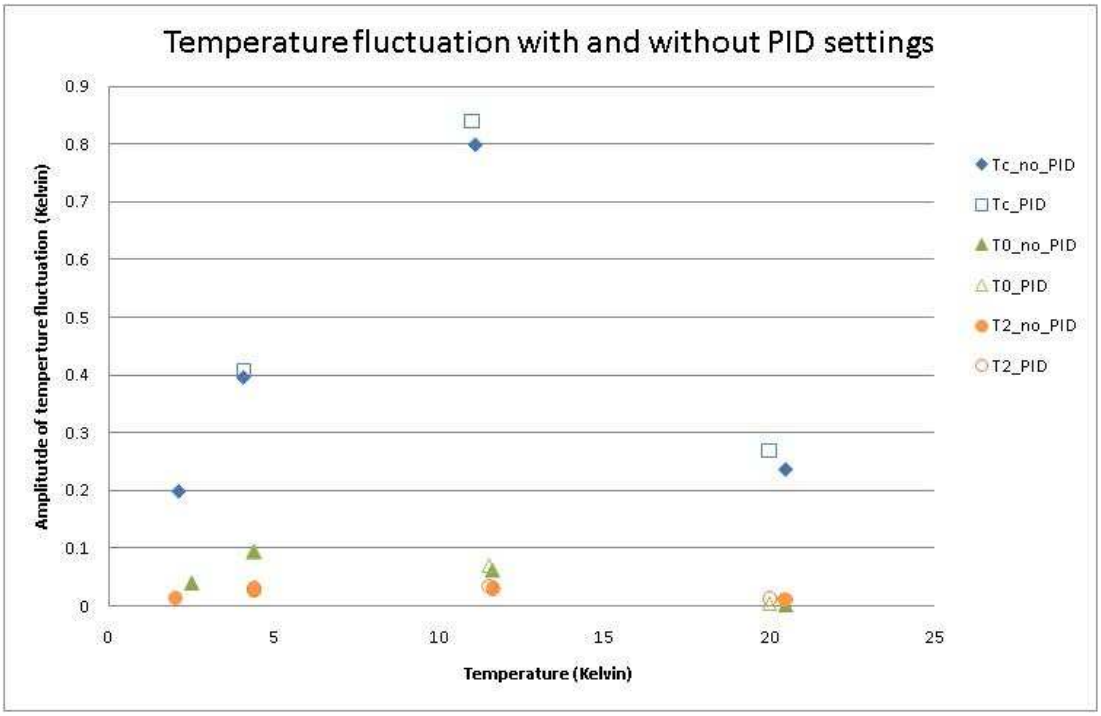

Figure C.8: *Proportional, Integral and Differential (PID) settings were tested for the Lakeshore 340 Temperature Controller. The graph above shows the influence of adjusting the PID settings of the system- the PID values can automatically altered for different for the lower and upper temperature ranges.*

An oscilloscope was used to monitor the real time temperature fluctuations. The output numbers of the Lakeshore devices was set to monitor the voltage output. Data of mean temperature and overall fluctuations were read out and converted to temperature to plot this graph.

C.3 Thermal model of system

To complement the experimental setup and the calculations done for thermal conductivity a thermal model of the system was produced using Ansys Workbench

[141]. This program allows the user to input properties of the materials being used as well as including information on contact surfaces, bonding, radiation effects, heat leaks etc. A thermal analysis can be run on the completed model to demonstrate the heat flow within. Figure C.9 shows the steady state thermal analysis result for 9 mW of power from one heater. This model demonstrates the heat flow when the sample is held at a constant temperature on the base plate and a constant power being input to the heater.

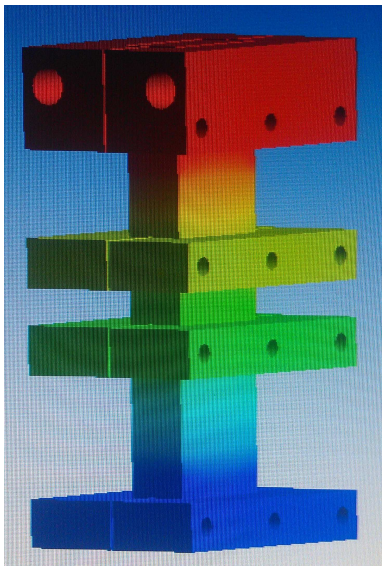

Figure C.9: Thermal analysis of the experimental setup showing the isothermal conditions reached after the stabilisation time has been reached.

References

[1] S. Howell, *Handbook of CCD Astronomy*. The Edinburgh Building, Cambridge CB2 2RU, UK: Cambridge University Press, 2 ed., 2006.

[2] D. Goddard and D. Milne, *Parkes: Thirty Years of Radio Astronomy*. 150 Oxford Street, PO BOX 1139, Collingwood, VIC 3066, Australia: CSIRO Publishing, 2 ed., 2001.

[3] M. Sarazin, "Measuring Seeing, The Differential Image Motion Monitor (DIMM)." 2002.

[4] P. Charles and F. Seward, *Exploring the X-ray Universe*. The Pitt building, Trumpington Street, Cambridge CB2 1RP, UK: Cambridge University Press, 1 ed., 1995.

[5] J. Vernin, C. Munoz-Tunon, and M. Sarazin, "E-elt site characterisation status," *Procedings of SPIE 7012*, 2008.

[6] H. Spoon, "Galaxy Crash course." , 6 2008.

[7] F. Roddier, *Adaptive Optics in Astronomy*. The Edinburgh Building, Cambridge CB2 2RU, UK: Cambridge University Press, first ed., 1999.

[8] H.-U. Kaeufl, P. Ballester, P. Biereichel, B. Delabre, R. Donaldson, R. Dorn, E. Fedrigo, G. Finger, G. Fischer, F. Franza, D. Gojak, G. Huster, Y. Jung, J.-L. Lizon, L. Mehrgan, M. Meyer, A. Moorwood, J.-F. Pirard, J. Paufique, E. Pozna, R. Siebenmorgen, A. Silber, J. Stegmeier, and S. Wegerer, "CRIRES: a high-resolution infrared spectrograph for ESO's VLT," in *Society of Photo-Optical Instrumentation Engineers (SPIE) Conference Series* (A. F. M. Moorwood and M. Iye, eds.), vol. 5492 of *Society of Photo-Optical Instrumentation Engineers (SPIE) Conference Series*, pp. 1218–1227, Sept. 2004.

[9] H. Kaufl, R. Esteves, E. Fedrigo, D. Gojak, J.-L. Lizon, E. Marchetti, S. Oberti, J. Paulique, E. Pozna, and S. Tordo, "Crires: Commissioning of the macao adaptive optics module and general status report," *Telescopes and Instrumentation*, vol. 124, pp. 2–4, 2006.

[10] A. Woodcraft, "Cryogenic Detectors in Astronomy." http://cirl.lowtemp.org/background_astronomy.html. Accessed 4/2008.

[11] T. L. Wilson, K. Rohlfs, and S. Huttemeister, *Tools of Radio Astronomy*. Springer, fifth ed.

[12] G. Rieke, *Detection of Light: From the Ultraviolet to the Submillimeter*. The Edinburgh Building, Cambridge CB2 2RU, UK: Cambridge University Press, 2 ed., 2003.

[13] G. Ventura and L. Risegari, *The Art of Cryogenics*. Linacre House, Jordan Hill, Oxford OX2 8DP, UK: Elsevier, first ed., 2008. .

[14] E. Sutton, *Observational Astronomy: Techniques and Instrumentation*. The Edinburgh Building, Cambridge CB2 2RU, UK: Cambridge University Press, 1 ed., 2012.

[15] M. Fich, "SCUBA-2: A Submillimeter Wavelength Camera for Astronomy." , 2004.

[16] United Kingdom Astronomy Technology Centre, "Unveiling the Universe at Submillimeter Wavelengths." , Jan. 2002.

[17] M. Hollister, "SCUBA-2 instrument- an application of large-format superconducting bolometer arrays for submillimeter astronomy." , 01 2009.

[18] J. Gardner, "Science with the james webb space telescope," *Proceedings IAU Symposium No. 232*, pp. 87–98, 2006.

[19] M. Clampin, "The james webb space telescope (jwst)," *Advances in Space Research*, vol. 41, pp. 1983–1991, 2008.

[20] The WMAP Science working group, "Wilkinson Microwave Anisotropy Probe (WMAP) Explanatory Supplement," 2003.

[21] J. Raab and E. Tward, "Northrop grumman aerospace systems cryocooler overview," *Cryogenics*, vol. 50, pp. 572–581, 2010.

[22] D. Bugby, C. Stouffer, J. Garzon, M. Beres, and A. Gilchrist, "Advanced devices for cryogenic thermal management," in *Proceedings of Advances in Cryogenic Engineering conference*, pp. 1790–1798, 2006.

[23] G. Wright, G. Reike, P. Barella, T. Boeker, L. Colina, E. van Dishoeck, P. Driggers, G. Goodson, T. Greene, A. Heske, T. Henning, P.-O. Lagage, M. Meixner, G. Nøorgaard-Nielson, G. Oloffson, T. Ray, M. Ressler, J. Thatcher, C. Waelkens, D. Wright, and A. Zhender

[24] G. Wright, G. Reike, L. Colina, E. van Dishoeck, G. Goodson, T. Greene, P. Lagage, A. Kamik, S. Lambros, D. Lemke, M. Meixner,

H. Norgaard, G. Oloffson, T. Ray, M. Ressler, C. Waelkens, D. Wright, and A. Zhender, "The jwst miri design concept," *Proceedings of the SPIE*, vol. 5487, pp. 653–663, 2004.

[25] N. Jessen, H. Nørgaard-Nielsen, and J. Schroll, "Cfrp lightweight structures for extremely large telescopes," *Composite Structures*, vol. 82, pp. 310–316, 2008.

[26] K. Makowski, M. Larson, A. Loc, B. Z. R. Leland, and B.Hayashi, "Development of a low leak cfrp stand for miri cooler jt heat exchanger stage," *Proceedings of Advances in Cryogenic Engineering conference*, 2010.

[27] CERN, "The Large Hadron Collider." , 08 2012.

[28] Conseil Européen pour la Recherche Nucléaire, "CERN experiments observe particle consistant with long-sought Higgs boson." , July 2012.

[29] T. F. Flower, *Great Ideas In Science.* http://www.stkate.edu/physics/phys100/Chapt10.html: Online Textbook, first ed., 2005.

[30] University of Glasgow, Institute for Graviatational Research. http://www.physics.gla.ac.uk/igr/index.php?content=research, . Accessed 6/2008.

[31] S. Miyoki, T. Uchiyama, K. Yamamoto, H. Ishitsuka, M. Ohashi, K. Kuroda, D. Tatsumi, S. Telada, M. Ando, T. Tomaru, N. Sato, T. Suzuki, T. Haruyama, A. Yamamoto, and T. Shintomi, "CLIO Cryogenic Laser Interferometer Observatory," in *International Cosmic Ray Conference*, vol. 5 of *International Cosmic Ray Conference*, pp. 3073–+, July 2003.

[32] M. Griffin, B. Swinyard, and L. Vigroux, "The Herschel-SPIRE Instrument," in *Proc. "The dusty and Molecular Universe"*, vol. SP-577, pp. 27–29, Jan. 2005.

[33] James Webb Space Telescope Image. http://spacewire.esa.int, . Accessed 3/2009.

[34] A. L. Woodcraft, "Lessons learned from SCUBA-2 for future cryogenic instrumentation in space," *Proc. SPIE*, vol. 7010, p. 70102M, 2008.

[35] sci.esa.int/science-e/www/object/index.cfm?fobjectid=31401fbodylongid=847. Accessed 4/2011.

[36] NASA, "Report of the Presidential Commission on the Space Shuttle Challenger Accident," vol. 1, p. 72, 6 1986.

[37] M. C. Runyan and W. C. Jones, "Thermal conductivity of thermally-isolating polymeric and composite structural sup-

port materials between 0.3 and 4 K," *Cryogenics*, 2008. doi:10.1016/j.cryogenics.2008.06.002.

[38] L. Risegari, M. Barucci, E. Olivieri, E. Pasca, and G. Ventura, "Very-low-temperature thermal conductivity of polymeric supports for massive cryogenic detectors," *Proc. of Astroparticle, Particle and Space Physics, Detectors and Medical Physics Applications*, vol. 2, 2003.

[39] G. Ventura, G. Bianchini, E. Gottardi, I. Peroni, and A. Peruzzi, "Thermal expansion and thermal conductivity of Torlon at low temperatures," *Cryogenics*, vol. 39, no. 5, pp. 481–4, 1999.

[40] M. Barucci, E. Olivieri, E. Pasca, L. Risegari, and G. Ventura, "Thermal conductivity of Torlon between 4.2 and 300 K," *Cryogenics*, vol. 45, pp. 295–299, 2005.

[41] R. Richardson and E. Smith, *Experimental Techniques in Condensed Matter Physics at Low Temperatures*. Perseus Books, 1988.

[42] C. Enss and S. Hunklinger, *Low-Temperature Physics*. Springer, 1 ed., 2005.

[43] J. Weisend, *Handbook of Cryogenic Engineering*. 325 Chestnut Street, 800, Philadelphia, PA, USA: Taylor and Francis, first ed., 1 1998.

[44] V. Martelli, N. Toccafondi, and G. Ventura, "Low-temperature thermal conductivity of nylon-6/cu nanoparticles," *Physica B*, no. 405, pp. 4247–4249, 2010.

[45] W. R. G. Kemp, P. G. Klemens, and R. J. Tainsh, "The lattice thermal conductivity of copper alloys: effect of plastic deformation and annealing," *Phil. Mag.*, vol. 4, pp. 845–857, 1959.

[46] J. W. Ekin, *Experimental techniques for low-temperature measurements*. Oxford: Oxford University Press, 2006.

[47] D. Krause and H. Bach, *Low Thermal Expansion Glass Ceramics*. Springer, 2nd ed., 2005.

[48] T. Barron and G. White, *Heat capacity and thermal expansion at low temperatures*. Springer, 1 ed., 1999.

[49] W. Phillips, "Tunneling states in amorphous solids," *Journal of Low Temperature Physics*, vol. 7, no. 314, pp. 351–360, 1972.

[50] G. K. White, *Experimental techniques in low-temperature physics*. Oxford: Clarendon Press, 1979.

[51] F. Pobell, *Matter and Methods at Low Temperatures*. Heidelberg: Springer-Verlag, first ed., 1992.

[52] T. Barratt, "Thermal conductivity part ii: Thermal conductivity of badly-conducting solids," pp. 81–93, 1914.

[53] F. W. Jordan, "Some novel laboratory experiments," *Proceedings of the Physical Society of London*, vol. 27, no. 1, pp. 470–471, 1915.

[54] T. Ashworth, L. R. Johnson, C. Hsiung, and M. Kreitman, "Use of the linear heat flow for poor conductors and its applications to the thermal conductivity of nylon," *Cryogenics*, vol. 13, pp. 34–40, 1973.

[55] J. M. Corsan, "A compact thermal conductivity apparatus for good conductors," *Journal of Physics E: Scientific Instruments*, vol. 17, no. 9, pp. 800–807, 1984.

[56] G. Ventura, "Thermal expansion and thermal conductivity of torlon at low temperatures," *Cryogenics*, vol. 39, pp. 481–484, 1999.

[57] A. L. Pope, B. Zawilski, and T. M. Tritt, "Description of removable sample mount apparatus for rapid thermal conductivity measurements," *Cryogenics*, vol. 41, no. 10, pp. 725–31, 2001.

[58] F. Rondeaux, P. Bredy, and J. M. Rey, "Thermal conductivity measurements of epoxy systems at low temperature," *Poster presented at CEC 2001 Madison, WI*, 2001.

[59] G. Ventura, E. Gottardi, I. Peroni, A. Peruzzi, and G. Ponti, "Low temperature thermal conductivity of polyamide-imide," *Elsevier. Nuclear Physics B-Proceedings Supplements*, vol. 78, pp. 571–2, 1999.

[60] M. Barucci and G. Bianchini and T. Del Rosso and E. Gottardi and I. Peroni and G. Ventura, "Thermal expansion and thermal conductivity of glass-fibre reinforced nylon at low temperature," *Cryogenics*, vol. 40, no. 7, pp. 465–7, 2000.

[61] M. Barucci, G. Ventura, T. D. Rosso, E. Gottardi, E. Pasca, and G. Bianchini, "Low-temperature thermal characterization of support material for massive cryogenic detectors," *Submitted to World Scientific*, 2002.

[62] M. Barucci, E. Gottardi, E. Olivieri, E. Pasca, L. Risegari, and G. Ventura, "Low-temperature thermal properties of polypropylene," *Cryogenics*, vol. 42, no. 9, pp. 551–5, 2002.

[63] G. Haacke and D. P. Spitzer, "Method for thermal conductivity measurements on solids," *Journal of Scientific Instruments*, vol. 42, no. 9, pp. 702–704, 1965.

[64] A. Hofmann, "The thermal conductivity of cryogenic insulation mateirals and its temperature dependence," *Cryogenics*, vol. 46, pp. 815–824, 2006.

[65] NASA, "Cassini: Unlocking Saturn's Secrets." , 07 2012.

[66] M. Imamuddin and A. Dupre, "Heat loss due to radiation in a thermal conductivity apparatus," *Journal of Physics E: Scientific Instruments*, vol. 6, no. 6, pp. 540–544, 1973.

[67] D. J. Dickson, "Measurement of the thermal conductivity of thermal insulations using miniature heat flow sensors," *Journal of Physics E: Scientific Instruments*, vol. 6, no. 11, pp. 1074–1076, 1973.

[68] D. Hands and F. Horsfall, "A thermal conductivity apparatus for solid and molten polymers," *Journal of Physics E: Scientific Instruments*, vol. 8, no. 8, pp. 687–690, 1975.

[69] D. Salmon, "Thermal conductivity of insulations using guarded hot plates, including recent developments and sources of reference materials," *Measurement Science and Technology*, vol. 12, no. 12, pp. R89–R98, 2001.

[70] T. A. Marshall, "An apparatus for measuring the coefficient of thermal conductivity of solids and liquids," *British Journal of Applied Physics*, vol. 4, no. 4, pp. 112–114, 1953.

[71] H. Xie, H. Gu, M. Fujii, and X. Zhang, "Short hot wire technique for measuring thermal conductivity and thermal diffusivity of various materials," *Measurement Science and Technology*, vol. 17, no. 1, pp. 208–214, 2006.

[72] L. Vozar, "A computer-controlled apparatus for thermal conductivity measurement by the transient hot wire method," *Journal of Thermal Analysis and Calorimetry*, vol. 46, no. 2, pp. 495–505, 1996.

[73] M. Maqsood, M. Arshad, M. Zafarullah, and A. Maqsood, "Low-temperature thermal conductivity measurement apparatus: design assembly, calibration and measurement on (y123, bi2223) superconductors," *Superconductor Science and Technology*, vol. 9, no. 4, pp. 321–326, 1996.

[74] J. Y. Chen, A. Chen, and L. Halldahl, "Application of the transient plane source (tps) technique for measuring thin coating layers." , . Accessed 5/2009.

[75] H. R. Meddins and J. E. Parrott, "An apparatus for the high-temperature measurement of thermal diffusivity, electrical conductivity and seebeck coefficient," *Journal of Physics D: Applied Physics*, vol. 2, no. 5, pp. 691–697, 1969.

[76] N. Savvides and W. Murray, "Apparatus for the measurement of thermal diffusivity featuring a low-frequency sine-wave generator and a digital phase meter," *Journal of Physics E: Scientific Instruments*, vol. 11, no. 9, pp. 941–947, 1978.

[77] D. G. Cahill and R. O. Pohl, "Thermal conductivity of amorphous solids above the plateau," *Phys. Rev. B*, vol. 35, pp. 4067–4073, Mar 1987.

[78] D. G. Cahill, H. E. Fischer, T. Klitsner, E. T. Swartz, and R. O. Pohl, "Thermal conductivity of thin films: measurements and understanding," *Journal of Vacuum Science Technology A-Vacuum Surfaces Films*, vol. 7, no. 3, pp. 1259–66, 1989.

[79] R. G. Morris and W. G. Delinger, "Series comparative measurements of thermal conductivity with thermistors," *Journal of Scientific Instruments*, vol. 42, no. 12, pp. 910–911, 1965.

[80] R. L. Powell, H. M. Roder, and W. M. Rogers, "Low-temperature thermal conductivity of some commercial coppers," *J. App. Phys.*, vol. 28, no. 11, pp. 1282–1288, 1957.

[81] H. Zierfuss, "An apparatus for the rapid determination of the heat conductivity of poor conductors," *Journal of Scientific Instruments*, vol. 40, no. 2, pp. 69–71, 1963.

[82] M. J. Laubitz and D. L. McElroy, "Precise measurement of thermal conductivity at high temperatures (100–1200 k)," *Metrologia*, vol. 7, no. 1, pp. 1–15, 1971.

[83] C. Arnaboldi and I.I.I.F.T. Avignone and J. Beeman and M. Barucci and M. Balata and C. Brofferio and C. Bucci and S. Cebrian and R.J. Creswick and S. Capelli and L. Carbone and O. Cremonesi and A. de Ward and E. Fiorini and H.A. Farach and G. Frossati and A. Giuliani and D. Giugni and P. Gorla and E.E. Haller and I.G. Irastorza and R.J. McDonald and A. Morales and E.B. Norman and P. Negri and A. Nucciotti and M. Pedretti and C. Pobes and V. Palmieri and M. Paven and G. Pessina and S. Pirro and E. Previtali and C. Rosenfield and A.R. Smith and M. Sisti and G. Ventura and M. Vanzini and L. Zanotti, "CUORE: A Cryogenic Underground Observatory for Rare Events.." Subm. to NIM A, 1 2002.

[84] E. Previtali, C. Arnaboldi, D. Artusa, F. Avignone, M. Balata, I. Bandac, M. Barucci, , J. Beeman, , J. Brofferio, C. Bucci, S. Capelli, F. Capozzi, L. Carbone, S. Cebrian, O. Cremonesi, R. Creswick, A. de Ward, H. Farach, E. Fiorini, G. Frossati, A. Giuliani, P. Gorla, E. Haller, I. Irastorza, R. McDonald, A. Morales, E. Norman, A. Nucciotti, E. Olivieri, V. Palmieri, E. Pasca, M. Paven, M. Pedretti, G. Pessina, S. Pirro, C. Pobes, M. Pyle, R. Risegari, C. Rosenfield, M. Sisti, A. Smith, L. Torres, and G. Ventura, "CUORICINO: A large new bolometer array for astrophysical particles," *Nuclear Instruments & Methods on Physics Research*, 2004.

[85] M. Barucci, L. Lolli, L. Risegari, and G. Ventura, "Measurement of thermal conductivity of the supports of CUORE cryostat," *Cryogenics*, 2008.

[86] O. Louanasmaa, *Experimental Principles and methods below 1 K*. ?: Academic Press Inc. (London) Ltd., first ed., 1974.

[87] Guy K. White, *Experimental Techniques in Low Temperature Physics*. Great Clarendon Street, Oxford, OX2 6DP: Claradon Press, Oxford, third ed., 1979.

[88] R. C. Richardson and E. N. Smith, *Experimental Techniques in Condensed Matter Physics at Low Temperatures*. Addison-Wesley, 1988.

[89] H. M. Rosenberg, "The thermal conductivity of metals at low temperatures," *Phil. Trans. Roy. Soc.*, vol. 247A, pp. 441–497, 1955.

[90] A. C. Rose-Innes, *Low temperature laboratory techniques*. English Universities Press, 1973.

[91] "http://cryogenics.nist.gov/MPropsMAY/materialproperties.htm." online manual. NIST.

[92] D. Wlosewicz, K. Bartkowski, and J. Rafalowicz, "Temperature dependences of thermal and electric conductivity of brass alloys of different zinc concentration in the temperature range 4-300k," *Acta Physica Polonica A*, vol. A56, no. 6, pp. 779–85, 1979.

[93] P. H. Kes, J. G. A. Rolfes, and D. de Klerk, "Thermal conductivity of niobium in the purely superconducting and normal states," *Journal of Low Temperature Physics*, vol. 17, no. 3-4, pp. 341–64, 1974.

[94] G. Davey and K. Mendelssohn, "Heat conductivity of pure materials below 1 °K," *Physics Letters*, vol. 7, 1963.

[95] J. K. N. Sharma, "Heat conductivities below 1K: I," *Cryogenics*, vol. 7, pp. 141–156, 1967.

[96] A. Woodcraft, M. Hollister, D. Bintley, F. Gannaway, D. Gostick, and W. Holland, "Thermal design and performance of the SCUBA-2 instrument 1-k and mk systems," *Cryogenics*, vol. 49, pp. 504–513, 2009.

[97] "Windig." online. Microsoft Windows data digitiser.

[98] "Engauge digitiser." digitiser.sourceforge.net. Open source digitising software.

[99] "Stainless Steel: Types of stainless steel, J.J. Supply Company Inc.." www.jjsupplycompany.com/index_files/TypeofStainlessSteel.htm. Accessed 4/2011.

[100] G. Ventura and V. Martelli, "Very low temperature thermal conductivity of Kevlar 49," *Cryogenics*, vol. 49, pp. 366–377, 2009.

[101] G. Ventura and V. Martelli, "Thermal conductivity of Kevlar 49 between 7 and 290 k," *Cryogenics*, vol. 49, pp. 735–737, 2009.

[102] O. Umezawa and K. Ishikawa, "Electrical and thermal conductivities and magnetization of some austenitic steels, titanium and titanium alloys at cryogenic temperatures," *Cryogenics*, vol. 32, no. 10, pp. 873–80, 1992.

[103] J. Beddoes and J. Parr, *Introduction to stainless steels.* ASM International, 1999.

[104] C. Ho, R. Powell, and P. Liley, "Thermal conductivity of the elements: A comprehensive review," *Journal of Physical and Chemical Reference Data*, vol. 3, no. 1, pp. 587–605, 1974.

[105] M. Lorenzini, "Thermomechanical characterization of Materials for Future Interferometric GW Detectors." , 3 2007.

[106] Y. S. Touloukian, P. E. Liley, and S. C. Saxena, *Thermophysical properties of matter. Vol. 1. Thermal conductivity: metallic elements and alloys.* NY: Plenum, 1970.

[107] D. J. Benford, T. J. Powers, and S. H. Moseley, "Thermal conductivity of kapton tape," *Cryogenics*, vol. 39, no. 1, pp. 93–5, 1999.

[108] R. Radebaugh, N. V. Frederick, and J. D. Siegwarth, "Flexible laminates for thermally grounded terminal strips and shielded electrical leads at low temperatures," *Cryogenics*, vol. 13, pp. 41–43, 1973.

[109] S. L. Wipf, "Low temperature heat transfer by contact in vacuo, and thermal conductivity of kapton," pp. 692–5, 1985.

[110] D. Rula, D. Smith, and L. Sparks, "Thermal conductivity of polypyromellitimide film with alumina filler particles from 4.2 k to 300 k," *Cryogenics*, vol. 36, pp. 283–290, 1996.

[111] H. Yokoyama, "Thermal conductivity of polyimide film at cryogenic temperature," *Cryogenics*, vol. 35, no. 11, pp. 799–800, 1995.

[112] M. Barucci, E. Gottardi, I. Peroni, and G. Ventura, "Low temperature thermal conductivity of kapton and upilex," *Cryogenics*, vol. 40, pp. 145–147, 2000.

[113] J. Lawrence, A. B. Patel, and J. G. Brisson, "The thermal conductivity of kapton hn between 0.5 and 5 k," *Cryogenics*, vol. 40, no. 3, pp. 203–7, 2000.

[114] R. Radebaugh, "Electrical and thermal magnetoconductivities of single-crystal beryllium at low temperatures and its use as a heat

switch," *Journal of Low Temperature Physics*, vol. 27, no. 1/2, pp. 91–105, 1977.

[115] A. Anderson, W. Reese, and J. Wheatley, "Thermal conductivity of some amorphous dielectric solids below 1 k," *The Review of Scientific Instruments*, vol. 34, no. 12, pp. 1386–1390, 1963.

[116] M. Barucci, G. Bianchini, T. D. Rosso, E. Gottardi, I. Peroni, and G. Ventura, "Thermal expansion and thermal conductivity of glass-fibre reinforced nylon at low temperatures," *Cryogenics*, vol. 40, no. 7, pp. 465–467, 2000.

[117] T. Scott, J. de Bruin, M. Giles, and C. Terry, "Low temperature thermal properties of nylon and polyethylene," *J. Applied Physics*, vol. 44, no. 3, pp. 1212–1216, 1973.

[118] Philip. J. Meeson and Guy K. White, *Experimental Techniques in Low Temperature Physics*. Great Clarendon Street, Oxford, OX2 6DP: Oxford University Press, fourth ed., 2002.

[119] R. Berman, E. L. Foster, and H. M. Rosenberg, "The thermal conductivity of some technical materials at low temperatures," *Brit. J. App. Phys.*, vol. 6, no. 4, pp. 181–182, 1955.

[120] "Janis Research Company, Wilmington, MA, USA." http://www.janis.com/index.htm. Accessed 6/2008.

[121] "Helium Compressor Unit, CSW-71, Sumitomo Heavy Industries Ltd.." http://www.shi.co.jp/english/index.html, . Accessed 6/2008.

[122] "Coolmation Group, Cosmotec Industrial Cooling." www.coolmation.co.uk. Accessed 6/2008.

[123] "Oerlikon Leybold Vacuum, Vacuum Pump and Exhaust Management System Solutions." http://www.oerlikon.com/leyboldvacuum/.

[124] "Python." http://www.python.org. Python Software Foundation.

[125] "Picowatt AVS Resistance Bridge, Finland." http://picowatt.fi. Accessed 6/2008.

[126] "Lakeshore." Product manual. Lakeshore Cryogenics.

[127] "Labview™." http://www.ni.com/labview. National Instruments.

[128] Jack. Ekin, *Experimental Techniques for Low Temperature Measurements: Cryostat Design, Materials, And Critical Current Testing*. Great Clarendon Street, Oxford, OX2 6DP: Oxford University Press, fourth ed., 2006.

[129] "Cernox sensor calibration ." Product manual. Lakeshore Cryogenics.

[130] "Keithley instruments." www.keithley.co.uk.

[131] "http://cryogenics.nist.gov/MPropsMAY/materialproperties.htm." online manual. NIST.

[132] Kennedy J.S., Woodcraft A.L., Parr-Burman P., "Thermal Cycle Test of Spectral Black Anodised and Gold Plated Components." , 1 2009.

[133] Science and Technology Facilities Council, "ISIS Experiment." , 1 2002.

[134] J. Hust and A. Lankford, "Reference standard materials: Update of thermal conductivity and electrical resistivity of electrolytic iron, tungsten, and stainless steel." 1984.

[135] D.-H. Gwo, "Ultra-precision and reliable bonding method." United States Patent no. US 6 284 085 B1, 2001.

[136] D.-H. Gwo, S. Wang, K. A. Bower, D. E. Davidson, P. Ehresberger, L. Huff, E. Romero, M. T. Sullivan, K. Triebes, and J. A. Lipa, "The gravity probe-b star-tracking telescope," *Advances in space research*, vol. 32, p. 1401, 2003.

[137] A. A. Van Veggel, J. Scott, D. A. Skinner, B. Bezensek, W. Cunningham, J. Hough, I. Martin, P. Murray, S. Reid, and S. Rowan, "Strength testing and sem imaging of hydroxidecatalysis bonds between silicon," *Classical and Quantum Gravity*, vol. 26, no. 175007, 2009.

[138] A. A. Van Veggel, D. Van den Ende, J. Bogenstahl, S. Rowan, W. Cunningham, G. H. M. Gubbels, and H. Nijmeijer, "Hydroxide catalysis bonding of silicon carbide," *Journal of the European Ceramics Society*, vol. 28, pp. 303–10, 2008.

[139] S. Rowan and S. M. Twyford, "Mechanical losses associated with the technique of hydroxide-catalysis bonding of fused silica," *Physics Letters A*, vol. 246, p. 471, 1998.

[140] B. Willke *et al.*, "The geo 600 gravitational wave detector," *Classical and Quantum Gravity*, vol. 19, pp. 1377–1387, 2002.

[141] "ANSYS." Product manual. ANSYS.